FEMTOSECOND LASER MICROFABRICATION FOR OPTO-MICROFLUIDIC DEVICES IN GLASS

DAIYING ZHANG

FEMTOSECOND LASER MICROFABRICATION FOR OPTO-MICROFLUIDIC DEVICES IN GLASS

by

Daiying Zhang

A thesis submitted to the

School of Graduate Studies

in partial fulfillment of the requirements for the degree of

Master of Science

Department of Physics and Physical Oceanography

Memorial University of Newfoundland

August 2011

St. John's Newfoundland

Abstract

The femtosecond laser has been a powerful tool to achieve laser processing and microfabrication due to the advantages of unprecedented high peak intensity, a small heat-affected zone and the capability of three dimensional fabrication on micro-/nano-scales.

In recent years, opto-microfluidics has emerged and progressed rapidly with many practical applications. Various microchannels and optical components have been integrated into a palm-size chip to accomplish optical measurements, clinical diagnostics, molecular analysis, and chemical synthesis. Opto-microfluidic devices significantly reduce reagent consumption, waste production, analysis time and labour costs.

In this dissertation, femtosecond laser microfabrication for the fabrication of opto-microfluidic devices in fused silica is studied. Femtosecond laser microfabrication on the surface and in the bulk of the samples is achieved using analysis on the influence of various fabrication parameters. Fabrication of surface/ bulk microchannels of variable specifications has been demonstrated by femtosecond laser microfabrication assisted by hydrofluoric acid etching. The feasibility of fabricating of waveguides in glass with femtosecond lasers has also been proved. Laminar flow and particle counting are accomplished with the femtosecond laser microfabricated opto-microfluidic devices. The effectiveness of these prototype opto-microfluidic devices is investigated.

Acknowledgements

I would like to thank my supervisor, Dr. Qiying Chen, for his support and encouragement in the past two years. I have learned so much from him personally and academically during these two years. I would also like to thank Dr. Liqiu Men of CREAIT for her help with the observation of Raman, SEM and AFM, as well as our valuable discussions, which provided me broader views in my research field and inspired many novel ideas. I would like to thank my labmate, Mr. Ping Lu, for his helpful suggestions.

I would like to thank my course instructors Dr. Martin Plumer, Dr. John Whitehead, and Dr. John Lewis for their interesting lectures and Dr. Todd Andrews for the suggestions from annual graduate progress meetings. The fellowships from the School of Graduate Studies, my supervisor, and the Department of Physics and Physical Oceanography are greatly appreciated. I also thank Memorial University for awarding me the J. Bruce and Helen H. French Graduate Scholarship on December 2010 that acknowledged my achievement during my M. Sc. Program.

Finally, I would like to thank my parents, my brother and my sister-in-law for their everlasting help and support.

Table of Contents

List of Tables

List of Figures

Chapter 1 Introduction

1.1 Femtosecond laser microfabrication

Since the first laser was reported by Theodore Maiman at the Hughes Research Laboratory in California in 1960, laser technology has made great progress over the past 50 years. Many powerful laser systems are now used for fabrication such as cutting, welding, quenching and carving [1]. However, long duration pulsed lasers and continuous wave (CW) lasers [2], such as CO_2 and Nd:YAG lasers, generate a significant amount of heat by resonance absorption. The heat melts material in the focus regions, disperses into neighbouring regions, and induces a large heat-affected zone which decreases machining precision. Excimer lasers [3], which are a kind of ultraviolet (UV) laser with a pulse width of tens of nanoseconds, can disintegrate the molecular bonds within materials and ablate rather than melt the material. Excimer lasers can remove the surface material of the particular region without heating or changing the surrounding material; therefore, they are commonly used in eye surgery and semiconductor manufacturing. However, excimer lasers are limited to microfabrication on surfaces. In the 1990s, femtosecond lasers with extremely high peak intensity and ultrashort pulse duration emerged, making high precision, small heat-affected zone and three-dimensional laser microfabrication feasible.

1.1.1 Fabrication mechanisms

Compared with conventional laser-matter interactions, the processes between a femtosecond laser and matter are more complicated. When a femtosecond laser pulse is tightly focused into a bulk sample, the high pulse intensity in the focal region induces a

large amount of excited electrons from the conduction band by nonlinear photoionization, and then the excited electrons absorb the laser energy by avalanche ionization to form plasma. Plasma transfers the energy to the lattices by coupling with photons and phonons. If the lattices deposit enough energy, permanent structural changes will occur at the focused location. Therefore, nonlinear photoionization and avalanche ionization are the kernels for understanding the fabrication mechanisms.

1.1.1.1 Nonlinear photoionization

Photoionization refers to a process, in which an electron in a bound state of an atom or molecule is excited into a free state by absorption of an energetic photon. For a femtosecond laser, the laser wavelength is commonly in the near infrared (IR) or visible region which is transparent to some materials such as fused silica. The energy of a single laser photon is not high enough to excite an electron from the valence band to the conduction band and induce linear photoionization. Therefore, the atom or molecule has to simultaneously absorb multiple photons in order to overcome the ionization potential. This process is called multiphoton ionization (MPI). The multiphoton absorption rate φ_{MPI} can be expressed as [4]

$$\varphi_{MPI}(I) = \sigma I^m \tag{1.1}$$

where m is the number of photons required for ionization, σ is the absorption cross section of m photons and I is the laser intensity. Multiphoton ionization is often induced by a laser with a short wavelength and low intensity. Tunnel ionization [5], another type of nonlinear photoionization, is often induced by a laser pulse with a long wavelength and strong laser fields. In an intense electric field, the potential barrier of an atom (molecule)

drastically distorts. Therefore, the barrier length decreases and electrons easily escape from the atom (molecule).

In 1965, Keldysh introduced a parameter γ to distinguish multiphoton ionization and tunnel ionization [6]. A recent study by Chin *et al.* revealed that, if $\gamma < 0.5$, it is in the tunnel regime, and if $\gamma > 0.5$, it is in the multiphoton regime (Fig. 1-1) [5].

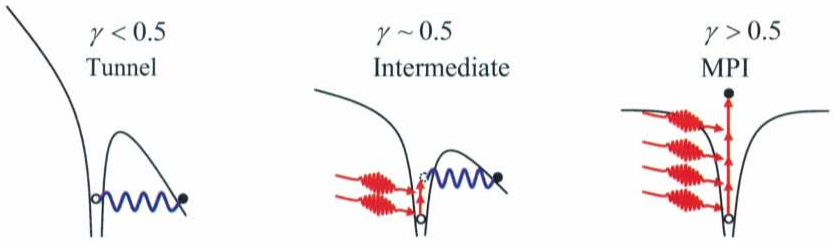

Figure 1-1 Schematic illustration of tunnel ionization and multiphoton ionization.

1.1.1.2 Avalanche ionization

After nonlinear photoionization, a few electrons with low initial kinetic energies escape from the valence band to the conduction band. These free electrons in the strong laser fields could absorb or emit n photons while scattering with a much heavier particle (atom, molecule or ion). The heavy particle keeps the momentum constant during the interaction. The process of absorbing n photons is called inverse Bremsstrahlung or free-free transition. After one or more inverse Bremsstrahlung processes, the free electrons acquire kinetic energy E_e, which is higher than the ionization potential. Subsequent collision gives rise to the release of an extra free electron from the molecule or atom, and results in two free low energy electrons. The two electrons undergo the same processes as

before, each giving rise to two more electrons, and so on, until the material breaks down. This is called cascade or avalanche ionization [5].

1.1.2 Applications of femtosecond laser microfabrication

When high energy femtosecond laser pulses, which can induce nonlinear processes, are focused on a bulk sample, the sample will be modified at the focus region with fewer heat-affected zones, and then three-dimensional structures can be fabricated by moving the sample through the femtosecond laser beam. Depending on the different properties of the laser, three types of structures can be written in transparent dielectric materials: isotropic positive refractive index modification [7-9], birefringence modification [10-12], and voids due to micro-explosion [13-15]. Among the various fabricated structures, optical waveguides (refractive index modification) and microchannels (voids due to micro-explosion) are two important structures with promising applications in optoelectronic devices.

1.1.2.1 Optical waveguides

Hirao *et al.* first reported the writing of waveguides in glass with a femtosecond laser in 1996 [16]. When a 810 nm Ti: Sapphire laser with a pulse width of 120 fs and a repetition rate of 200 kHz was focused through 5~20× microscope objective lenses to irradiate silica glasses, the refractive index of silica glass was found to increase at the focus region. By displacing the glass sample, waveguides were fabricated.

In the next few years, waveguides constructed in different photosensitive materials were reported, such as $LiTaO_3$ [17], Foturan glass [18], erbium-doped oxyfluoride silicate

glass [19], Er Yb-doped oxyfluoride silicate glass [20], aluminosilicate glass [21], and sodium aluminum phosphate glass [22]. Near-field profiles, refractive index profiles, and propagation losses of the waveguides at different pulse intensities, wavelengths, durations, repetition rates, polarizations, depths of focus, speeds of scan, and numeral apertures of objective lenses were reported [19, 23-27].

When using conventional spherical focusing lens in perpendicular waveguide writing, the cross sections of the waveguides produce strong core asymmetry which causes significant propagation loss [27]. The multi-scan technique [8, 20, 28] is a typical method to produce waveguides with a symmetrical cross section (such as circular or square). In 2002, Cerullo *et al.* proposed an astigmatic beam configuration to overcome the asymmetry [29, 30]. In the experiments, two cylindrical lenses were inserted in the path to reshape the beam. Waveguides with circular cross section were produced by astigmatic beams irradiation. Cheng *et al.* proposed a slit shaping configuration [31], in which a slit with its long dimension parallel to the writing direction was inserted in front of the objective lens to reshape the laser beam. He *et al.* used a pair of parallel gratings to separate the spectral components of the femtosecond laser beam in space before the beam entered the objective lens, and also obtained waveguides with a circular cross section [32].

Homoelle *et al.* fabricated the first Y coupler inside a pure fused silica sample [33], which opened up new possibilities for the fabrication of photonic devices, such as 1-to-N splitters [34, 35], $N \times N$ couplers [36-40], multimode interference waveguides [41], gratings [42-46] and waveguide lasers [47].

1.1.2.2 Microchannels

Marcinkevicius *et al.* succeeded in fabricating microchannels in fused silica with femtosecond laser pulses irradiation followed by a 5% aqueous solution of HF acid etching [48]. Matsuo *et al.* produced microchannels by using KOH solution as an etchant after femtosecond laser microfabrication [49].

Because HF acid gradually etches into the interior of a microchannel, different exposure durations in HF acid cause a typical conical shape of microchannel which is usually not preferred in the applications. In order to obtain uniform channels, Vishnubhatla *et al.* irradiated a conical spiral in the opposite direction to complement the cone [50]. By this technique, a cylindrical microchannel with a length of 4 mm was achieved. He *et al.* heated etched glass sample to a high temperature which was close to the melting point of fused silica (1700°C) using an oxyhydrogen flame, and drew the glass sample in a direction parallel to the microchannel to produce a circular cross section [51].

Besides the methods that are mentioned above, Li *et al.* drilled 3-D microchannels in glass using a water-assisted femtosecond laser [52]. Drilling began from the rear surface which contacted the distilled water. Then, water flowed into the drilled hole to reduce the effect from blocking and re-depositing of ablated material in the small hole. Further research done by other research groups achieved drilling microfluidic chambers and multi-microholes by a multiple-focus process [53-57].

1.2 Opto-microfluidics

Optofluidics refers to a platform of integrated optical devices and systems that performs an investigation on the properties of fluids. By combining microfluidic and optics technologies, optofluidic devices integrate bulky laboratory equipment into a palm-sized chip to realize optical measurements, biological analyses, and chemical syntheses. Microfluidic and optofluidic devices significantly reduce reagent consumption, waste production, analysis time and labour cost. There is no distinct boundary between microfluidics and optofluidics because many common techniques and applications are found in these two disciplines. We use the term "opto-microfluidics" to refer to the research that takes advantages of both optics/photonics and microfluidics. A few monographs provide good reviews on the history and development in the field of opto-microfluidics [58-63].

1.2.1 Techniques for microfabrication of opto-microfluidic devices

The first microfluidic device was a miniaturized gas chromatography (GC) system developed by Terry *et al.* [64] at Stanford University in the 1970s. In the 1980s, the growth of molecular biology, and especially of genomes, DNA, and proteins, stimulated the development of devices with higher sensitivity and resolution for microanalysis. Microfluidic systems for analyzing aqueous solutions were developed by some research groups [65-67]. The original microfluidic fabrication technologies were derived from silicon microelectronics, which were well developed in the semiconductor industry. However, these techniques are very expensive, complicated, and time consuming. Furthermore, silicon is not suitable to be applied in a microfluidic device due to its being

opaque to visible and UV light, in addition to its high cost. One of feasible techniques for the fabrication of microfluidic devices is microelectromechanical systems (MEMS) (Fig. 1-2). During fabrication, a material, typically a polymer, is deposited on a substrate first, and then the master pattern is transferred into the material by lithography. After an etching process (wet or dry etching), either the exposed or unexposed material is removed. Finally a cover is attached on the surface of the chip to enclose the microchannels.

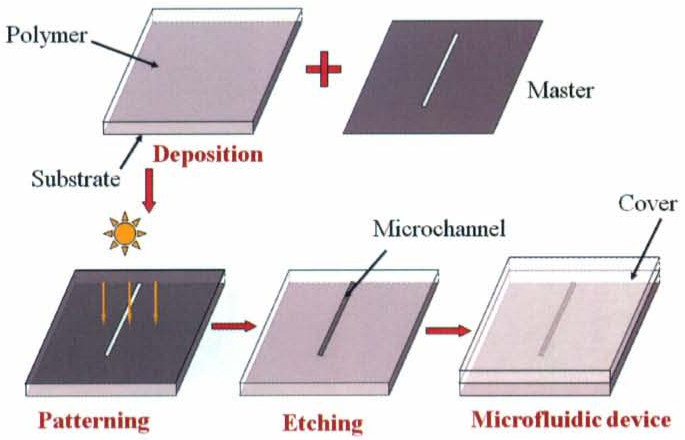

Figure 1-2 Procedures for the fabrication of a microfluidic device by MEMS technology.

Another widely adopted method to fabricate a microfluidic system is casting, in which a soft polymer elastomer of high optical transparency is used, i.e., poly (dimethylsiloxane) (PDMS) or poly (methyl methacrylate) (PMMA). Figure 1-3 shows the steps for the fabrication of a microfluidic device by casting. A mold is produced by soft lithography [68, 69] or laser fabrication [70-72] in a photoresist layer (SU-8) or a metallic sheet. The hot embossing technique [70, 72, 73], or poured molding method [71,

74-76], is used to duplicate the mold in the polymer sheet. The peeled polymer replica is sealed to a flat surface to enclose the channels. Very complex structures in a microfluidic device can be developed by stacking multiple polymer layers (100 μm in thickness per layer), similar to a sandwich structure [74, 77]. The time period is less than two days starting from design to the production of a functional device.

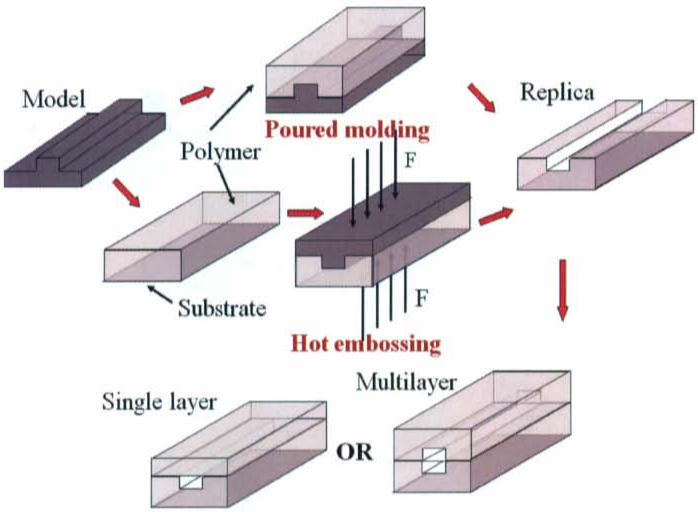

Figure 1-3 Steps for the fabrication of a microfluidic device by casting.

In some cases, optical components, especially optofluidic waveguides, were integrated into the chips, and their effectiveness in the transmission of light were demonstrated. Examples include solid core/solid cladding waveguides [78, 79], solid core/liquid cladding waveguides, liquid core/solid cladding waveguides [80], liquid core/liquid cladding waveguides and hybrid waveguides [75, 81, 82]. They are essential optofluidic technologies even though the term "optofluidics" was not coined at that time. The term "optofluidics" first appeared in the name of a University Research Center

founded by the Defense Advanced Research Projects Agency (DARPA) in 2003. It defined optofluidics as a field to "develop adaptive optical circuits by integrating optical and fluidic devices." Now, optofluidics has been broadly defined as the combination of optics and microfluidics in the same platform to leverage specific advantages of these two disciplines [62].

For applications in optofluidics, the drawbacks of using polymer materials, such as solubility in many common solvents, damage after tightly focused laser irradiation, and fluorescence at certain common wavelengths, appear to be severe. In contrast, glass-based devices with high optical transparency to visible light and inertness to chemical solvents are very suitable for these applications. Consequently, new fabrication techniques are required to produce microfabrication in various glasses. In this regard, ultrafast laser microfabrication has been revealed as a powerful approach to fabricate opto-microfluidic devices in glass [83].

Any of the aforementioned microfabrication techniques is effective to fabricate opto-microfluidic devices with pros and cons. Table 1-1 compares the advantages and drawbacks of different microfabrication techniques used for fabricating opto-microfluidic devices. Judicious selection is necessary in order to choose a suitable technique for a specific application. In some cases, a special approach may be required to overcome the drawbacks of a specific microfabrication technique.

Table 1-1 Comparison of the advantages and drawbacks of different fabrication techniques.

Fabrication technique		Advantages	Drawbacks	Ref.
Molding fabrication	MEMS	Possibility to fabricate complex structures	1. Long fabrication time; 2. Fluorescence of polymer at certain common wavelengths; 3. Material damage after tightly focused laser irradiation; 4. Polymer solubility in many common solvents.	[68, 71-73, 79]
	Casting			
Femtosecond laser fabrication		1. Less fabrication time 2. Optical transparency to visible light 3. Inertness to chemical solvent	1. Requiring precise laser focus and motion control; 2. Possible requirement of additional chemical etching.	[83-85]

1.2.2 Applications of opto-microfluidic technologies

1.2.2.1 Opto-microfluidic sensors for biological analysis

The original motivation for developing opto-microfluidics was for biological analysis, in which immunoassay and DNA separation have been the two main applications. Immunoassay is a biochemical technique that detects the presence and quantities of antibodies or antigens in samples [86-88]. Competitive immunoassay and sandwich assay are two common methods. When a labeled (such as an enzyme or fluorescent dye) analytical reagent with special antigens or antibodies is mixed with the sample, a specific binding will form between the antigen and the corresponding antibody. The changes in colour and intensity of light from the labeled binding are recorded to identify the immunity of the sample. The traditional technique requires a large amount of reagents and a long incubation time. Microfluidics-based immunoassays have been developed by several research groups. For instance, in a sandwich assay for the antigen, the antibody is

injected into the microchannels by a pressure-driven [89], electrokinetic control [90, 91] or centrifugal force [92], and deposited onto the wall of the microchannels to form the solid-phase antibody. Then the antigen in the sample is mixed with the solid-phase antibody in the microchannel, and finally another labeled antibody is added into the microchannel for signal generation. The colour signals from the antibody-antigen-labeled antibody bindings are detected by a fluorescence microscope after removing excess antibodies and antigens through washing steps. All steps can be completed in one hour, and the reagent consumption is only on the order of microliters. Roos *et al.* [93] and Herrmann *et al.* [94] used microspheres to support the binding, and the fluorescence signals were collected from these microbeads. These microspheres provided an increased surface area to support the immune complex. Nanoparticle-labeled microfluidic immunoassay [95] was reported by Lin *et al.*, in which free labeled antigens were deposited on the nanoscaled gold particles, and the scattered light from the particles provided readout to trace the bindings between antibodies and antigens.

Capillary electrophoresis (CE) is a rapidly growing opto-microfluidic separation technique, which has been applied in bioanalysis, environmental pollutant analysis and food analysis [96, 97]. By using high electric fields (larger than 500 V/cm), all ions and positive or negative particles in the sample generate electroosmotic and electrophoretic flow respectively. Electroosmotic flow pulls the analytes in the buffer solution through the capillary toward the cathode. However, the electrophoretic flow reduces the flow rate of the negatively charged analytes and increases the flow rate of positively charged analytes in the capillary. Therefore, the analytes separate due to different mobilities. UV absorption

detectors are equipped to detect the constituents of the sample near the outlet of the capillary. The data from the detector is displayed as an electropherogram, in which peaks at different times are shown for separated chemical compounds.

A CE instrument is formed when the microchannels and reservoirs are assembled in a chip with extra high potential. Figure 1-4 illustrates two types of CE chips and their operations. First, a sample is injected into the sample well. Then, high voltage is applied at the sample well and the sample waste well (ground). The high electric field pulls the sample from the sample well to the sample waster well (Fig. 1-4 (b)). Finally, the voltage is removed and another high voltage is applied to the buffer well and buffer waster well (ground). The sample within the intersection is drawn towards the buffer waster well (Fig. 1-4 (c)). Through this step, the constituents of the sample are separated by electroosmotic and electrophoretic flow.

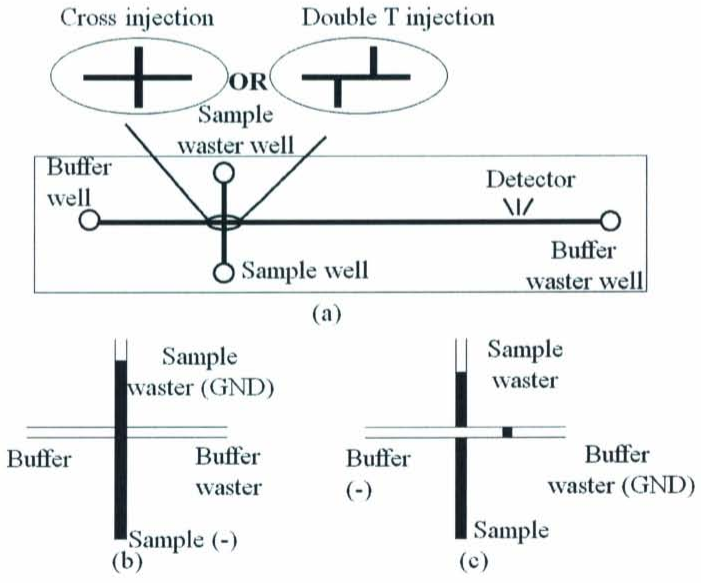

Figure 1-4 Schematic illustration of a CE chip: (a) a CE chip with reservoirs; (b) CE Process of the injection phase; and (c) CE process of the separation phase.

The CE chips are extensively used in medical research such as DNA analysis [98], infectious disease diagnostics [99] and sample purification [100]. Now some companies such as Micronit Microfluidics BV in the Netherlands, microLIQUID in the USA and Micralyne Inc. in Canada supply CE chips and kits for clinical diagnostics. Meanwhile, several research groups have integrated different components into CE chips to satisfy diverse needs of analysis. For example, the combination of polymerase chain reaction (PCR) with CE chip (PCR-CE chip) is a focus of research, in which one or multiple PCR chambers are integrated into the CE chip to incubate and analyze DNA simultaneously [101-106]. Prakash *et al.* fabricated PCR arrays with PCR valves and ports on the CE chip to control the flow of samples in each PCR chamber. The CE chip can be reused by using different PCR chambers [107]. The proposals that combine multichannel with CE chips to produce mixing, reaction and separation were also reported by some research groups [108-111]. Munce *et al.* used CE with optical tweezers to achieve single-cell sorting and analysis in one chip [112]. A CE chip that was integrated with an acoustic wave sensor successfully trapped single live myocyte and clearly detected the contraction and relaxation of the cell without any influence from other cells [113].

The commonly adopted detection method in a CE chip is a confocal detection system. Bliss *et al.* integrated optical waveguides into a CE chip [114]. The electropherogram demonstrated that the waveguide detection possesses an equal or higher sensitivity than that of the confocal system. In order to accurately identify the constituents of a sample, the CE chip was connected to an electrospray mass spectrometry (ESMS) by a capillary [106], as shown in Fig. 1-5.

Figure 1-5 Schematic illustration of a CE chip with electrospray mass spectrometry.

1.2.2.2 Opto-microfluidic chemical sensors

Polymer particles are in high demand in biology, cosmetics, food processing, medicine, and pesticides. However, insufficient control and the high cost of traditional chemical synthesis techniques limit their applications. Kumacheva *et al.* proposed a novel approach [115] to achieve continuous and scalable production of core-shell droplets and polymer capsules in microfluidic devices, such as biopolymer microcapsules [116], Janus and ternary particles [117], microgels of biological polymers [118], monodisperse particles with microspheres, rods, disks and ellipsoids [119], dynamic lattices [120, 121] and colloidal particles at gas–liquid interfaces [122].

Centrifugal microfluidic devices were reported by Salin *et al.*, in which multiple chambers and capillary valves were fabricated in a disc. The flow of the solvent was controlled to achieve dissolution [123], mixing [124], extraction [77, 125] and reactions [124] between reagents by adjusting the rotational rate of the disc. The components and concentrations of analytes were measured at a detection unit by fluorescence and absorption spectra. In some cases, magnets were utilized in the chamber and base to serve as agitators to increase the efficiency of the chemical reaction. Centrifugal microfluidic

devices could be applied in environmental monitoring and soil analysis for their portability and rapidity.

An optofluidic platform for chemical component analysis by laser-induced breakdown spectroscopy (LIBS) was achieved by Fedosejevs *et al.* [126, 127]. A small thermal or piezoelectric actuator was deposited on the bottom of a microchannel while an orifice of a few microns was opened on the opposite wall of the actuator. During the operation, a bubble was first excited at the orifice by the actuator, and then a fast intense laser pulse broke down the bubble, and thus plasma with the components of the reagent was generated. As the plasma was cooled down, electrons and ions were recombined, accompanied by the emission of electromagnetic radiation with fingerprint wavelengths of the elements in the reagent, as detected by spectroscopic measurements. The most notable advantage of this technique is non-contact measurement, which completely avoids sample contamination.

1.2.2.3 Optofluidic surface plasmon resonance sensors

Surface plasmon polaritons (SPP) are electromagnetic waves that propagate along a metal and dielectric interface [128, 129]. SPP can be evanescent, which are excited by both electrons and photons. The excitation of SPP by photons is usually referred to as surface plasmon resonance (SPR). SPP cannot be directly excited by photons due to momentum mismatch. Special arrangements, such as Otto configuration [130], Kretschmann configuration [131], or a diffraction grating [132], are well-known techniques to couple photons into SPP in order to match the wave vectors of the photon and the surface plasmon, as illustrated in Fig. 1-6. In Otto configuration, the light

illuminates on a prism, and total internal reflection happens at the internal bottom of the prism. When a thin metal film is located close enough to the prism bottom, the SPP is excited on the surface of the metal by the interaction between an evanescent wave and a plasma wave (Fig. 1-6 (a)). The Kretschmann configuration is the most common approach. In the Kretschmann configuration, a thin metal film is coated onto the prism bottom. An evanescent wave which is induced by total internal reflection penetrates through the thin metal film, and excites the SPP at the outer side of the film (Fig. 1-6 (b)). The thickness of the metal layer is usually a few tens of nanometers to ensure that the evanescent wave travels through the metal and couples to a surface plasmon mode (Fig. 1-6 (d)). In a diffraction grating system, an evanescent wave is induced by diffraction at the surface of metal diffraction gratings, and excites the SPP at the surface of the metal layer (Fig. 1-6 (c)).

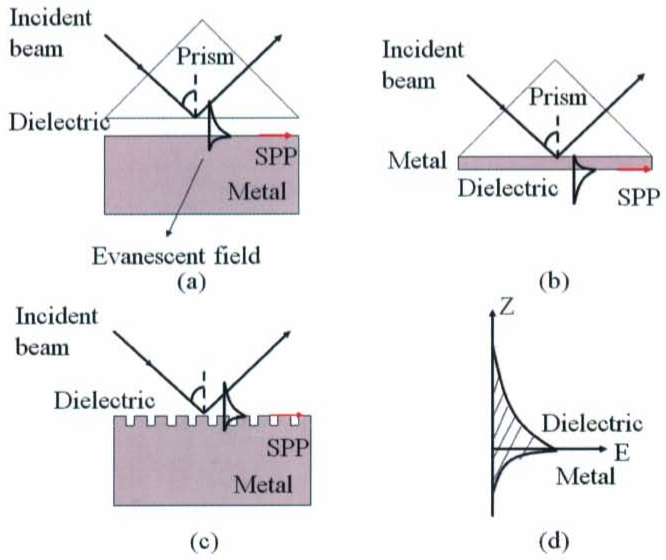

Figure 1-6 Surface plasmon resonance: (a) Otto configuration; (b) Kretschmann configuration; (c) a diffraction grating; and (d) evanescent field at the interface.

Since the wave travels on the interface of the metal and the external dielectric layer, SPR is very sensitive to any change at this interface, such as the density and temperature of the dielectric layer and the structure of the metal surface. Optofluidic SPR sensors for immunoassay and refractive index measurement have been reported by several research groups [133-135]. In these experiments, a prism coated with a gold film formed one wall of a micrchannel, and liquid solution as a dielectric material was infused into the gold-coated microchannel. When light with different incident angles was irradiated on the interface of the prism and gold film, part of the light, which matched with the SPR angle θ_{SP}, was attenuated into the gold film to generate SPR and the rest of the light was reflected. As a result, the reflection intensity showed a dip at the SPR angle due to the absorption of light by the surface plamons. A photodetector was placed at the end of the device to capture and monitor the intensity of the reflected wave. Immunoassay or refractive index was measured depending on the intensity changes of reflected light.

Nanohole-based SPR sensors have received considerable attention in recent years. One of the most important characteristics of a nanohole array is that the intensity of the transmitted light is enhanced at certain wavelengths due to SPP coupling when the incident light irradiates on the surface of the metal film. By monitoring the wavelengths of the intensity peaks, a nanohole-based SPR sensor is achieved. Compared with a standard reflective mode SPR sensor, a nanohole SPR sensor operates at normal incidence without the necessity to consider the SPP angle. Sinton *et al.* made nanohole array SPR sensors [136-141]. For example, a device with flow-through nanohole arrays,

instead of dead-end nanohole arrays in a SPR sensor, made reagents travel through the nanoholes rapidly, thus reducing the response time remarkably [141].

With the improvement of SPR techniques, surface plasmon resonance imaging (SPRI) has been proposed as a new kind of detection technique in biology [142]. Kanda *et al.* patterned a surface of metal (gold) with free-labeled protein antigens arrays [143]. When the sample flowed through the microchannel located above the patterned gold film, the antigen-antibody bindings were generated at the arrays. A high contrast SPRI based on the adsorbed proteins was produced to evaluate the quantitative and qualitative properties of the antibodies in the sample. Tabrizian *et al.* replaced the plain gold film in the SPR with periodic gold nanoposts to detect DNA hybridization. The optimal result showed a fivefold SPRI enhancement compared with the common SPRI [144]. The same research group also combined the SPRI technique with digital microfluidics (DMF) to detect biological samples [145, 146]. DMF is a fluid manipulation technique, in which a patterned array of electrodes is etched on the substrate with MEMS techniques and then coated with a waterproof material like Teflon to form DMF. Droplets can dispense and merge in DMF when an electrical potential is applied on sequential electrodes in the array [147-151]. Therefore, this combination achieved real-time monitoring and detection of reactions.

1.2.2.4 Opto-microfluidic sensors integrated with novel optical functionalities

Integration of micro-optical components into a chip could effectively shape beams to enhance the sensitivity of a sensor and increase its portability. Besides optical waveguides discussed in the previous sections, Table 1-2 lists several micro-optical components

integrated in opto-microfluidic devices, which include lenses [152-157], gratings [78, 158], mirrors [133, 159, 160] and light sources [161-163]. There is a continuing effort to produce integration of multiple components to acquire novel optical functionalities.

Optical tweezers are important instruments to trap and sort particles like cells, proteins, and microspheres. A tightly-focused laser beam (Gaussian beam) provides an attractive or repulsive force on the particles due to the changes in the momentum of light upon reflection or refraction. Although the force is on the order of piconewtons, it is large enough to hold and move small objects with sizes of several tens of microns. Taking advantage of the merits of opto-microfluidic devices with narrow channel widths, fiber-microfluidic tweezers have been particularly attractive in studying a variety of biological systems. Sinton *et al.* accomplished trapping multi-microsphere by dual-beam, which could be applied for contact-free storage of biological cells as well [164-167]. In addition, Guo *et al.* fabricated a microfluidic chip with on-chip lens structures to reduce the beam waist of the light and achieved a higher efficiency in optical operation and optofluidic transportation [152].

Table 1-2 Micro-optical components integrated in opto-microfluidic devices.

Optical component	**Fabrication technique**	**References**
Lenses	MEMS Femtosecond laser	[152, 153] [154-157]
Gratings	MEMS Femtosecond laser	[78] [158]
Mirrors	MEMS Femtosecond laser	[133, 159] [160]
Light sources	MEMS Femtosecond laser	[161] [162, 163]

The microcytometer is another important application of opto-microfluidic sensors. Azmayesh-Fard *et al.* [74] first injected two types of mixed dyed particles into the microchannel, and then coupled two excitation lasers with different wavelengths and durations into the microfluidic device with solid-core waveguides. Finally, a windowed Fourier transform was applied to the output optical signals. By this step, different types of particles were resolved and counted from peak intensities. Multiple parallel waveguides were integrated into an opto-microfluidic sensor to collect the fluorescent and scattered signals from labeled cells by Xu *et al.* [168]. The same group also fabricated micro-lenses in chips to shape the excitation beam and improve the signal-to-noise ratio of cytometers [153]. A wide-angle microfluidic cytometer was reported by Tsui *et al.* [169-171]. A conventional cytometer can only collect signals through small-angle forward scattering (5°) and side scattering (10°) in which errors are apparent when cells gather or irregular cells and other organelles exist. In the wide-angle microfluidic cytometer, the goniometric measurement and finite-difference time-domain (FDTD) method were adopted to overcome the disadvantages of conventional cytometers.

Refractive index (RI) sensing is another important application of opto-microfluidic sensors, which has been widely applied in environmental monitoring and optical measurement. Opto-microfluidic RI sensors based on Mach-Zehnder interferometer (MZI) [79, 172, 173], grating [158, 174], and refractometers [159] have been reported. All these reported methods adopted similar principles in which two identical beams were first coupled into different paths such as a solid core waveguide and a liquid core waveguide; then interference occurred due to the difference in the optical paths when the

two beams were combined. The measurement of the refractive index of the liquid can be achieved by monitoring the change of the interference intensity.

1.3 Outline of research

Opto-microfluidics has receives considerable attention for applications in optical measurements, biological analyses, and chemical syntheses due to the significant advantages of reduce reagent consumption, waste production, analysis time and labour cost. Among various microfabrication techniques for opto-microfluidic devices, femtosecond laser microfabrication draws considerable attention. High peak intensity, a small heat-affected zone and the capability of three-dimensional fabrication make the femtosecond laser a powerful tool for micromachining and microfabrication. Fused silica, a high-purity synthetic amorphous silicon dioxide, possesses a superior transmittance over a wide spectral range, especially in the ultraviolet, and an exceptional low thermal expansion coefficient. These excellent optical properties render its wide applications in various semiconductor and optical equipment. In this study, opto-microfluidic devices and systems fabricated by femtosecond lasers in fused silica are proposed and demonstrated.

Since the understanding of the femtosecond laser microfabrication is the first step in the design and preparation of opto-microfluidic devices, the surface morphologies and features of craters and grooves fabricated with different irradiation parameters are first investigated in Chapter 2. Compared with traditional waveguide fabrication techniques, femtosecond waveguide writing exhibits unique advantages of three-dimensional, maskless fabrication with a single step. In Chapter 3, type II waveguides are fabricated

with femtosecond waveguide writing technique. Raman spectra have been applied in the analysis of structure changes in the waveguides, which provides evidence on the origin of a type II waveguide. As an important component of opto-microfluidics, microchannels fabricated with femtosecond laser irradiation followed by HF acid etching are presented in Chapter 3 as well. A novel compensation fabrication method is proposed to improve the structure of microchannels. In addition, intakes are also fabricated for microchannel interconnection. Chapter 5 focuses on the laminar flow in the microchannel. Three-dimensional Y-shaped and three-intake microchannels are fabricated in fused silica, and laminar flow is observed in the microchannels using a fluorescence microscope. As the fundamental flow mechanism at microscale, the laminar flow provides references for choosing buffers and solutions in opto-microfluidic experiments. An opto-microfluidic particle counter has been designed and fabricated in fused silica, which is presented in Chapter 6. Compared with other particle counting devices, this particle counter is a real 3-dimensional microchannel without any extra bonding process. Furthermore, the operation was convenient. Experimental results with high precision demonstrate the feasibility of the opto-microfluidic particle counting devices proposed in this study,

Chapter 2 Femtosecond laser microfabrication on surfaces

2.1 Introduction

The first microstructure fabricated on the surface of a material by a femtosecond laser was reported in l995, in which sub-micron holes were machined in a silver film using 200 fs, 800 nm laser pulses. The advantage of a femtosecond laser for micromachining with minimized heat-affected zones was demonstrated by comparing them with the diameter of nanosecond pulsed laser drilled holes [175]. Since then, various patterns fabricated by femtosecond lasers have been studied on a wide range of materials, such as copper [176, 177], nickel [178], glass [179-181], silicon [176, 179, 182, 183], and polymers [184]. Through these studies, laser-matter interaction, energy deposition, thermal and collateral damage were revealed, and femtosecond laser microfabrication as a highly precise material processing technique was widely recognized.

Since fused silica is an important material for optical devices, ablation of fused silica by a femtosecond laser has drawn considerable attention. The sizes of ablated craters on fused silica with laser pulse duration ranging from picoseconds to femtoseconds were measured; and the dependence of a laser-induced surface damage threshold on pulse duration was demonstrated [185-187]. A clear increase in the size of the ablated craters for single- or multiple-shot ablation was observed as the laser fluence increased [185, 186]. Ashkenasi *et al.* proposed that the number of femtosecond laser pulses had a great impact on the surface damage threshold and the crater depth of fused silica in air or in a vacuum [188, 189]. Wu *et al.* reported that the morphology of the ablated microstructure

on the surface changed depending on the focusing condition, and sub-micrometer cavities and bubbles were fabricated with single pulse shots on the surface of fused silica by adjusting the focus position [190]. Morphology and composition analysis was performed on ablated grooves of fused silica, by Kasaai *et al.* The results showed that the chemical composition of a fused silica sample had no significant changes before and after laser irradiation, and the crystalline silicon dioxide detected from the ejected debris illustrated that the thawing, cooling and re-solidification processes occurred in fused silica during the laser-matter interaction [191]. Polarization-independent microgrooves were fabricated on a fused silica surface by femtosecond laser [192]. The groove profiles ablated by a femtosecond laser with various pulse energies (10-200 mW) and scan speeds (1-7 mm/s) were investigated by Ameer-Beg *et al.* [179]. They attributed the increase of the groove size at the low ablation rate to the incubation processes, in which the ablation takes a certain amount of pulses to reach a steady state due to weak two photon absorption in material.

All research results mentioned above were obtained under different laser conditions and experimental setups, and a systematic study has not yet been done. In this study, a home-made femtosecond laser microfabrication station established in our laboratory is the main tool for microfabrication. Comprehensive research is performed, such as making changes in the surface morphology which result from different laser focusing conditions on fused silica samples, and investigating features on the fused silica fabricated with different laser powers, pulse numbers, repetition rates, and writing speeds.

2.2 Experimental setup

The laser system used for fabrication is a Ti: Sapphire femtosecond laser amplifier with integrated oscillator and pump lasers (Coherent Libra). The output laser pulses have a maximum energy of 1 mJ at 800 nm and a pulse width of 67 fs. The repetition rate could be varied from a single shot to a maximum rate of 1 kHz. As shown in Fig. 2-1, a variable attenuator, consisting of a half wave plate and a polarizer, is placed in the path of the beam to control and continuously adjust the output power of the laser. A shutter triggered by a LabView program is used to control the exposure time of the sample to laser irradiation. A power meter monitors the change of the laser power in real time through a beam splitter.

The translation stages (Aerotech ATS 100), which moves in three dimensions with 0.3 μm accuracy, are powered by a multi-axis motion controller (Aerotech Unidex 511). The movements of the stages can also be programmed by LabView. A microscope objective lens focuses the laser beam onto the sample.

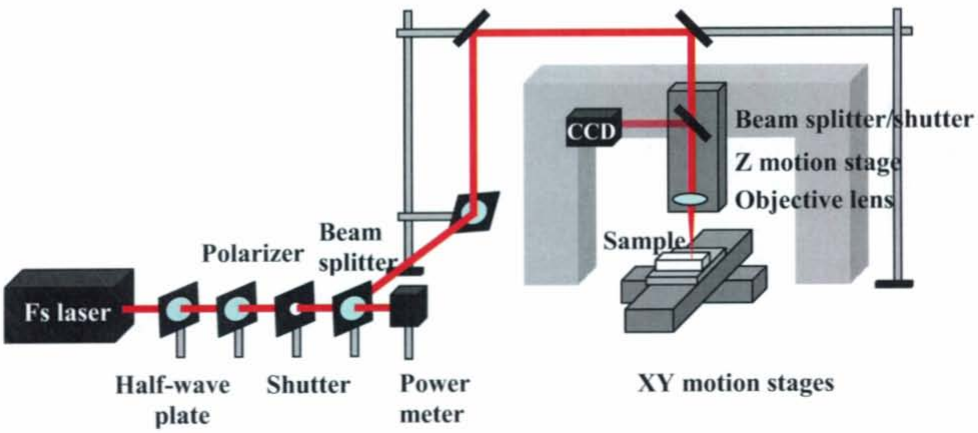

Figure 2-1 Schematic illustration of the experimental setup.

The material for femtosecond laser microfabrication used in this study is fused silica. Small samples are cut from a fused silica disk (125 mm diameter × 1mm thickness) with a diamond cutter. The samples are mounted on the XY stages. A beam splitter reflects the light from the sample surface into a CCD camera. A suitable position for laser microfabrication on the sample is found with the monitor by adjusting the XYZ stages. Depending on factors such as laser wavelength, numerical aperture of the objective lens, and focusing depth, the laser-induced damage threshold of the fused silica varies from tens to hundreds of nJ [193, 194]. Therefore, the laser energy is adjusted to several μJ (far larger than nJ) to achieve distinct changes of surface morphology which are observed more easily by the optical microscopy and the atom force microscopy (AFM).

2.3 Crater characterization

2.3.1 Effects of focusing condition

The beam produced by a femtosecond laser has a typical Gaussian profile (Fig. 2-2). ω_0 is the waist size, Z_R is the Rayleigh range, b is the depth of focus, and $\omega(z)$ is the radius at which the field intensity drops to $1/e^2$ of their axial values. The time-averaged intensity distribution is [195]

$$I(r,z) = I_0(\frac{\omega_0}{\omega(z)})^2 \exp(\frac{-2r^2}{\omega^2(z)}) \tag{2.1}$$

where $\omega(z) = \omega_0\sqrt{1+(\frac{z}{Z_R})^2}$, with $Z_R = \frac{\pi\omega_0^2}{\lambda}$, I_0 is the intensity at the center waist of the beam, r is the radial distance from the center axis of the beam, z is the axial distance from the beam's waist, and λ is the wavelength of the beam. Figure 2-3 is the simulation

of a femtosecond laser beam at the waist region using MATLAB, where ω_0 is 1 μm, and λ is 800 nm. It shows that most of the energy concentrates in a small elliptical central area. Therefore, femtosecond lasers are powerful tools to realize microfabrication due to the highly concentrated energy within a central area of a few microns in diameter.

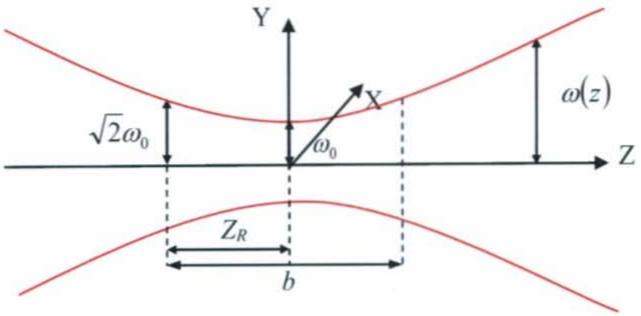

Figure 2-2 Gaussian beam width ω(z) as a function of the axial distance z . ω_0: beam waist; b: depth of focus; Z_R: Rayleigh range.

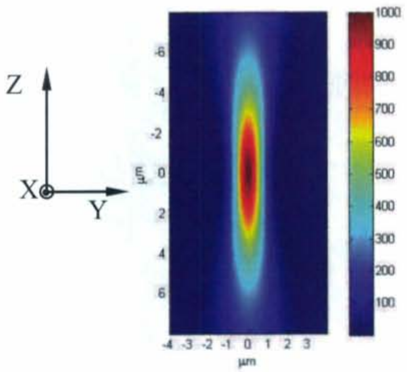

Figure 2-3 Simulation of a Gaussian beam. The waist is 1 μm, λ=800 nm.

The focusing condition has a significant effect on the surface morphology. Figure 2-4 shows a schematic illustration of five different focusing conditions, in which (a) and (e) correspond to de-focusing conditions, (b) and (d) show slight de-focusing, and (c) represents perfect focusing on the sample surface. Figure 2-5 is the image of pits in which single femtosecond laser pulses through an objective lens (20×, NA 0.46) are irradiated

on the sample, observed by an AFM (MulitMode™ SPM). For the 21 pits in the figure, each pit was fabricated with the focus location moved up 1 μm along the Z axis sequentially.

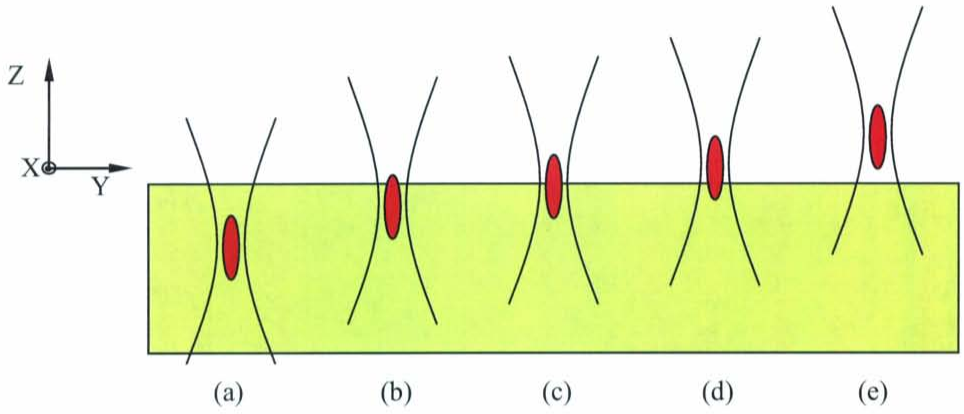

Figure 2-4 Schematic illustration of different focusing conditions: (a) and (e) correspond to de-focusing condition; (b) and (d) show slight de-focusing; and (c) represents perfect focusing on the sample surface.

The pits 1st~5th and 21st in Fig. 2-5 show no change in the morphology of the sample surface. The reason is that the laser energies at the sample surface in these cases are much less than the damage threshold, as the focus of the laser is too far away from the sample surface, such as Fig. 2-4 (a) and (e). However, circular tracks can be observed in the bulk of the sample with an optical microscope for pits 1st~5th (Fig. 2-6). This is because micro-explosion occurs [196] in the vicinity of the focus after the material is irradiated by the femtosecond laser of high pulse energy. Immense pressure forces the material from the focus region to move outward. Therefore, a void or low density (refractive index) region surrounded by a high density (refractive index) shell is induced. The stress-induced refractive index changes enhance the visibility of the tracks.

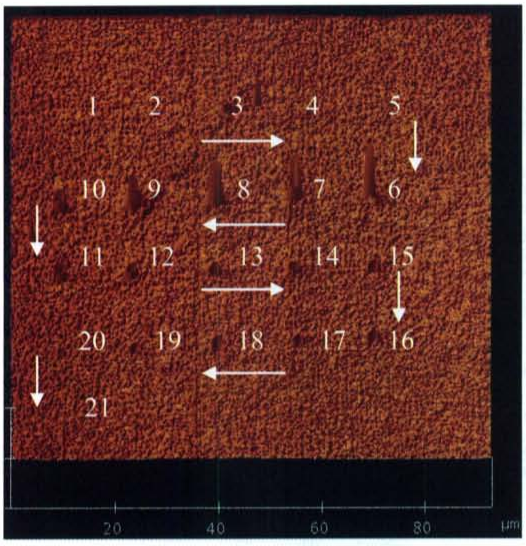

Figure 2-5 AFM image of 21 pits fabricated by single pulses with 4 μJ energy and an objective lens of magnification 20×.

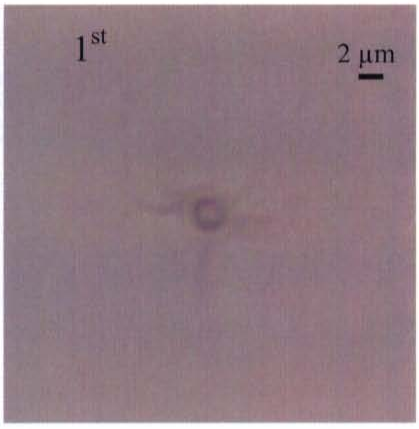

Figure 2-6 An optical micrograph of the 1st pit in Fig. 2-5.

When the femtosecond laser is focused on the positions near the surface (Fig. 2-4 (b)), high pressure makes the vaporized material break through the surface, spray out, and freeze around the hole. Figure 2-7 presents the AFM images of the ablated crater-like pits fabricated in different focusing conditions. Increasing debris accumulation around the craters can be found in the cases of deeper focus location because more material is vaporized and sprayed out.

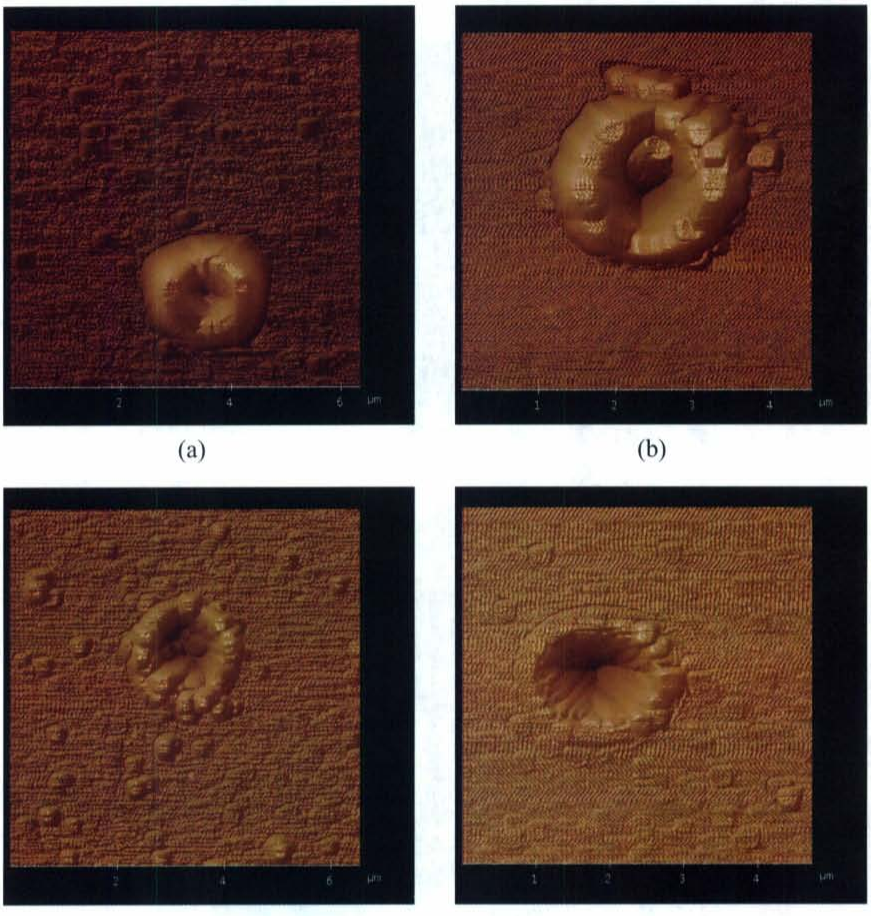

(a) (b)

(c) (d)

Figure 2-7 AFM images of the individual pits in Fig. 2-5: (a) the 6th pit; (b) the 8th pit; (c) the 11th pit; and (d) the 14th pit.

Figure 2-8 gives the changes in the depth and diameter of craters shown in Fig. 2-5. However, we cannot derive the exact focus location from Fig. 2-8 (a) because the sprayed material often re-deposits into the craters which affects the measured values of the depths and diameters of the craters. Considering the symmetry of a Gaussian beam in the Z

direction, as a rule of thumb, we believe that the middle pit 13th corresponds to the best focusing condition in view of the gradual pattern changes from pit 6th to 20th.

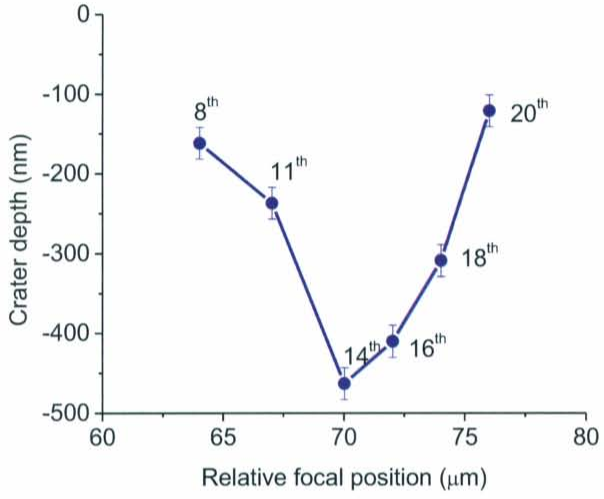

(a)

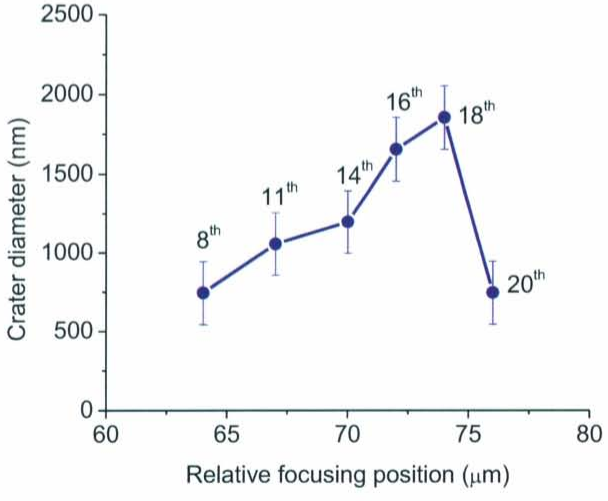

(b)

Figure 2-8 Changes in the depth and diameter of the craters fabricated at different focusing conditions.

2.3.2 Effects of pulse energy

The energy intensity of the Gaussian beam increases with the increase in pulse energy. Figure 2-9 shows the simulation of the intensity profile of femtosecond laser beams in the X-Z plane using MATLAB. The scale bar on the right indicates the correlation between intensity and colour. Red stands for a higher intensity, while blue represents a lower intensity. A larger size of high-intensity distribution is presented when the beam energy is higher (right one). This means that more precise focus positions will possess higher energies exceeding the damage threshold. As a result, the diameters and depths of the ablated craters also increase accordingly. Figure 2-10 presents six craters, each ablated by a single pulse of different pulse energies, in which (a) is an AFM image, (b) and (c) are the changes in the depth and diameter of the craters. The laser is focused on the sample surface with an objective lens (50×, NA 0.75). The size of crater increases with the increase of pulse energy as mentioned above.

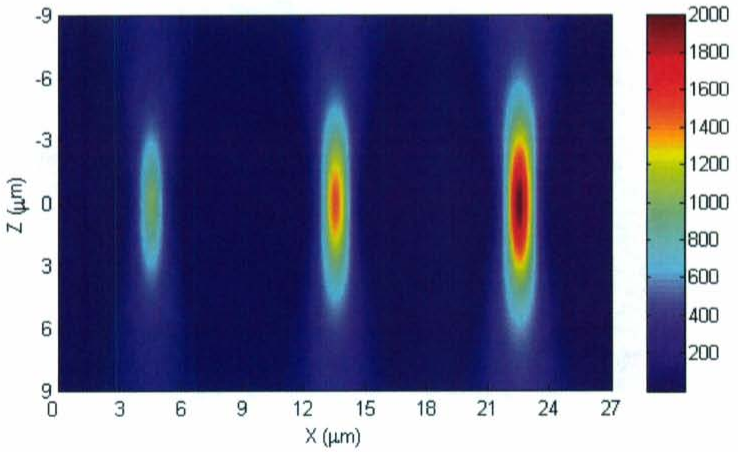

Figure 2-9 Simulation of the intensity profile of a Gaussian beam in the X-Z plane. The waist is 1 μm at a wavelength λ=800 nm.

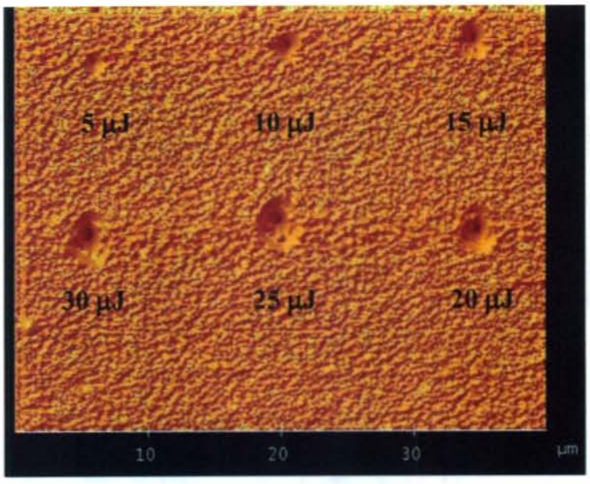

(a)

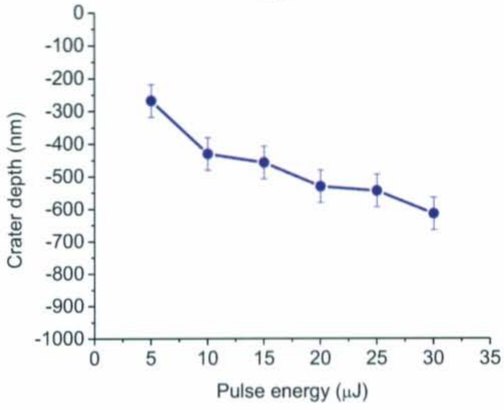

(b)

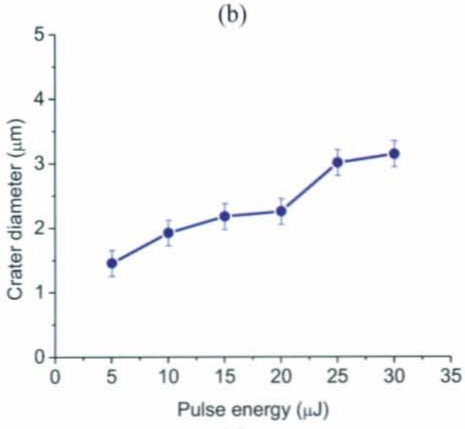

(c)

Figure 2-10 Craters ablated by single pulses of different pulse energies: (a) AFM image; (b) and (c) the changes in the depth and diameter of the craters.

2.3.3 Effects of repetition rate

Laser energy deposits through nonlinear absorption and spreads out to nearby regions by heat diffusion. If the heat diffusion time is longer than the interval time between pulses, heat accumulates and melts the material around the focus regions [197]. Compared with long pulse lasers such as CO_2 and excimer lasers, femtosecond lasers produce much smaller heat effects in laser-matter interactions. Since the ultrafast pulse laser with a pulse width on the order of tens of femtoseconds (10^{-14}-10^{-13} s) and the maximum repetition rate of 1 kHz (Fig. 2-11), the energy from the femtosecond laser does not have enough time to dissipate into the bulk of the sample within one pulse duration. Furthermore, the longer pulse interval (relative to the pulse duration) is also helpful for sample cooling.

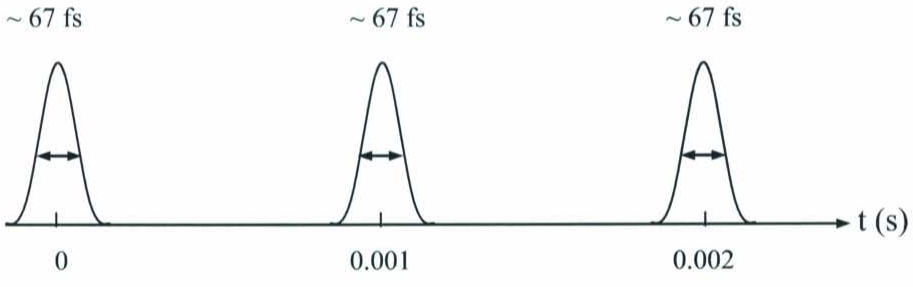

Figure 2-11 Schematic illustration of femtosecond laser pulses with 1 kHz repetition rate.

Figure 2-12 shows the effects of the repetition rate on the microfabrication of craters, in which (a) is an AFM image of the sample, and (b) and (c) are the changes in the depth and diameter of the craters. 500 pulses with different repetition rates are irradiated on the sample surface by an objective lens with a magnification of 50× (NA 0.75). The pulse energy is 3.5 μJ. The number of pulses is accurately controlled by the exposure time of

the shutter which is computer controlled. The result shows that the size of the crater increases with the increase of the repetition rate. This is because more heat accumulates due to a shorter pulse interval between pulses in a higher repetition rate, and more melting volume is generated around the focal volume. However, the heat-affected zones are very small (the increase in the size of the crater is on the order of nanometers for the case with a pulse energy of 3.5 μJ), as compared with other kinds of lasers.

2.3.4 Effects of pulse number

Figures 2-13 and 2-14 show the effects of pulse number on the craters fabricated by the femtosecond laser, which is irradiated on the sample surface with a pulse energy of 3.5 μJ by an objective lens with a magnification of 50× (NA 0.75). For the ablation by the laser beam at a 1 kHz repetition rate as shown in Fig. 2-13, the diameter and depth of the crater slightly increase at the first few pulses, and then stop growing after several hundred shots. The size increase is also caused by heat accumulation effects. With more shots of laser pulses, the volume of melted material is larger. When the ablation structure grows large enough after several hundred pulses, the laser beam intensity drops below the damage threshold. The crater remains unchanged due to no further energy deposition occurs. Figure 2-14 shows the morphology of the pits ablated by the laser beam at a 50 Hz repetition rate, which indicates that the size of the crater is nearly unchanged with the increase of pulse number. The reason is that the accumulated heat is negligible when laser pulses with much lower repetition rates irradiate the sample.

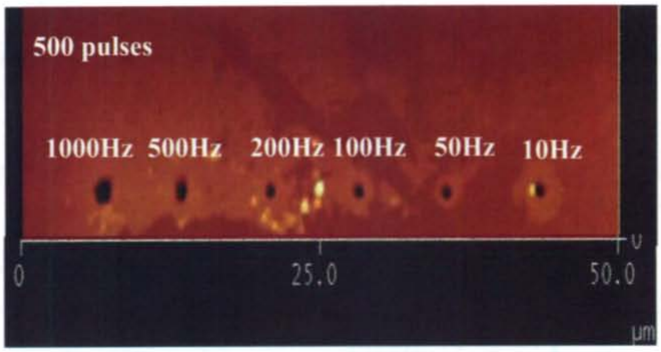

(a)

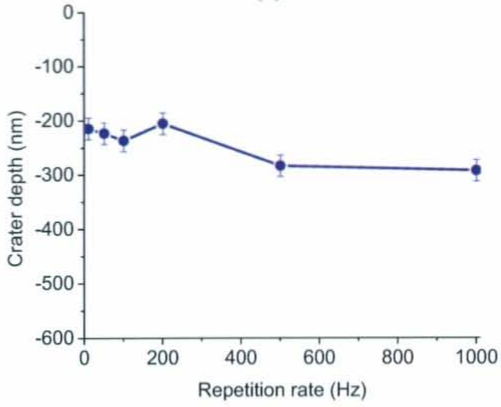

(b)

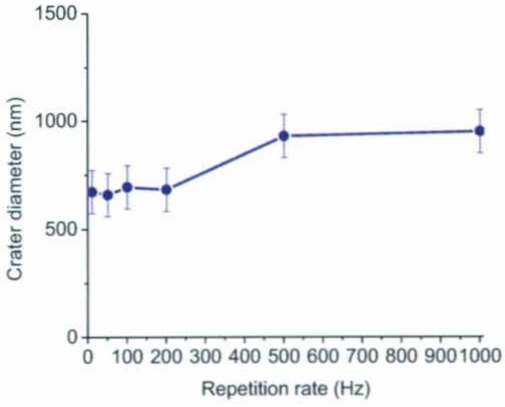

(c)

Figure 2-12 Craters fabricated by 500 pulses with a pulse energy of 3.5 μJ in different repetition rates: (a) AFM image of sample; (b) and (c) the changes in the depth and diameter of the craters.

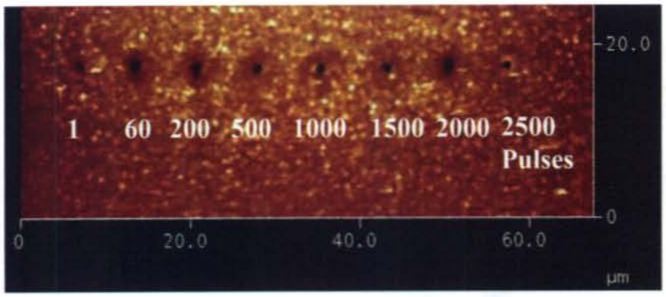

(a)

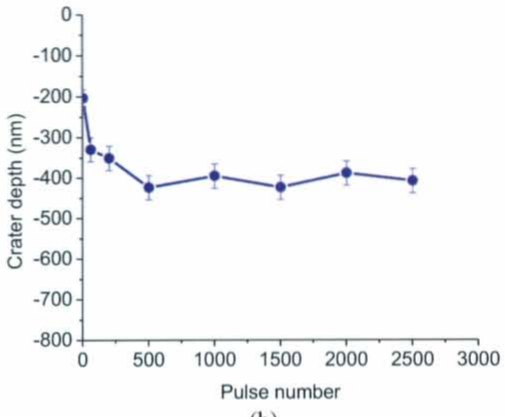

(b)

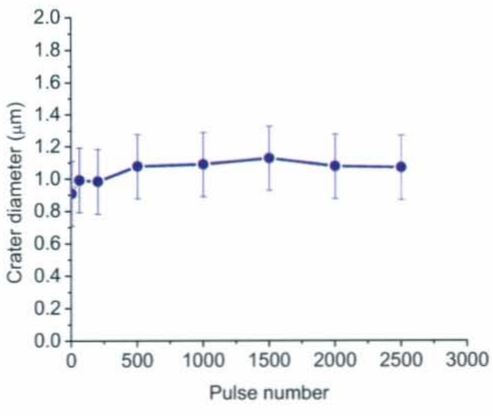

(c)

Figure 2-13 Craters fabricated by different pulse numbers of the femtosecond laser (3.5 μJ/ pulse, 1 kHz): (a) AFM image of sample; (b) and (c) the changes in the depth and diameter of craters.

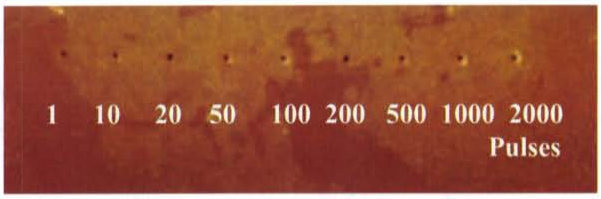

(a)

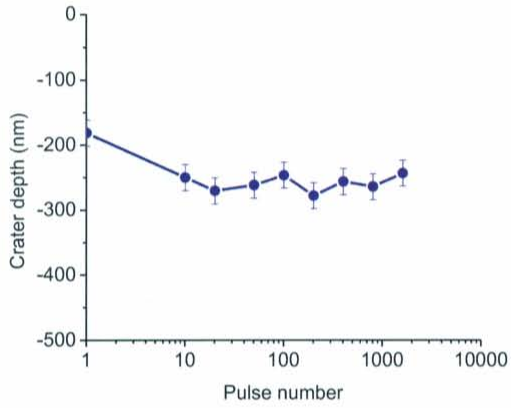

(b)

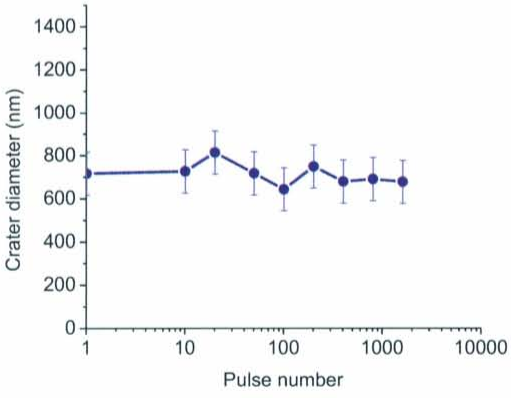

(c)

Figure 2-14 Craters fabricated by different pulse numbers of the femtosecond laser (3.5 μJ/ pulse, 50 Hz): (a) AFM image of the sample surface; (b) and (c) the changes in the depth and diameter of the craters.

2.4 Groove characterization

When the laser beam is focused on the surface of a moving sample controlled by translation stages, a groove is fabricated. Except for some cases with a specific description, all structures mentioned in the following sections are ablated with the femtosecond laser of 1 kHz repetition rate and an objective lens with a magnification of 50× (NA 0.75). Figure 2-15 is the AFM image of a groove fabricated by the laser of 30 μJ pulse energy and a translation speed of 1 μm/s [63]. The V-shaped cross section of the groove observed in Fig. 2-15 is in good agreement with the energy distribution of a Gaussian beam.

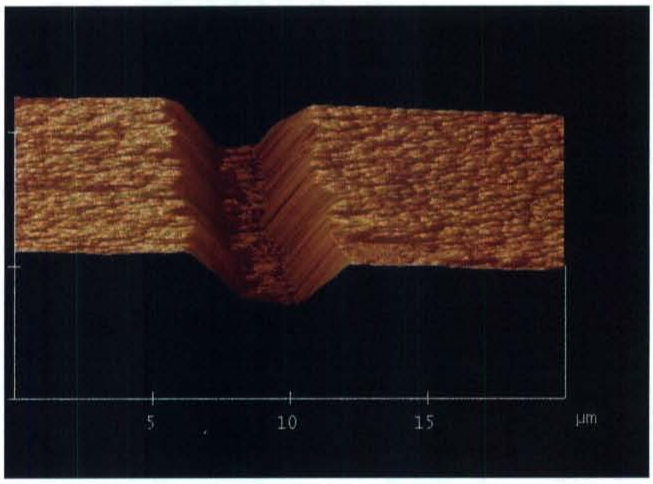

Figure 2-15 AFM image of a groove fabricated by the femtosecond laser of 30 μJ/ pulse, 1 kHz repetition rate, and 1 μm/s translation speed.

2.4.1 Effects of pulse energy

Figure 2-16 shows the grooves fabricated by the femtosecond laser of different pulse energies with a translation speed of 1 μm/s. The result is similar to the fabricated crater mentioned in the previous section, i.e. the size increases with the increase of the pulse energy.

2.4.2 Effects of translation speed

A lower translation speed of the sample during fabrication means that more laser pulses irradiate in the same location of the sample. Therefore, the effects of translation speed are similar to the effects of pulse number. Figure 2-17 shows the sample fabricated with different translation speeds at a laser energy of 30 μJ/ pulse. From Fig. 2-10, the average diameter of the craters fabricated by a single pulse is about 3.1 μm under the same irradiation parameters, and the size increases to 5 μm after multiple laser pulse irradiation. If the translation speed is 1 μm/s, it means that 5000 pulses irradiate on one spot, and if the translation speed is 50 μm/s, it means that 100 pulses irradiate on one spot. As mentioned in the previous section, the fabricated structure ceases growing after enough pulse shots. Therefore, the size of the groove does not exhibit significant change at a lower translation speed, as shown in Fig. 2-17.

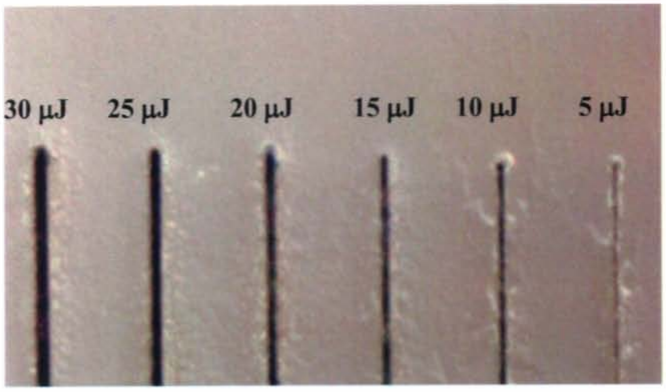

(a)

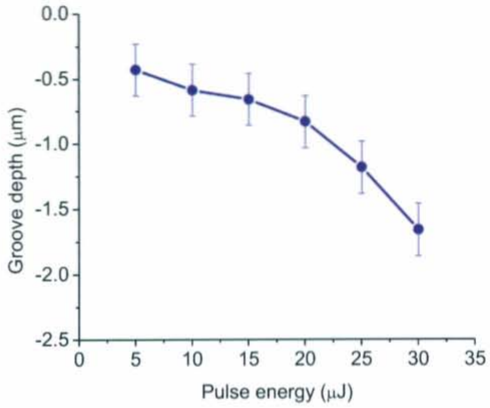

(b)

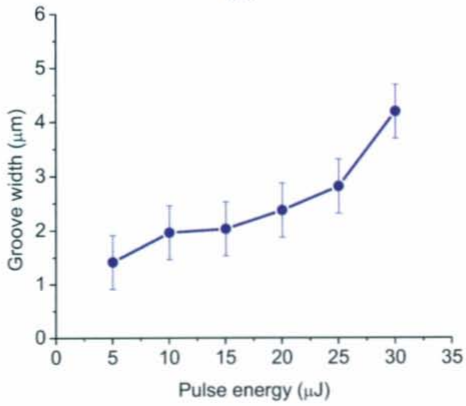

(c)

Figure 2-16 Grooves fabricated by the femtosecond laser of different pulse energies at a translation speed of 1 μm/s: (a) AFM image of sample; (b) and (c) the changes in the depth and width of grooves.

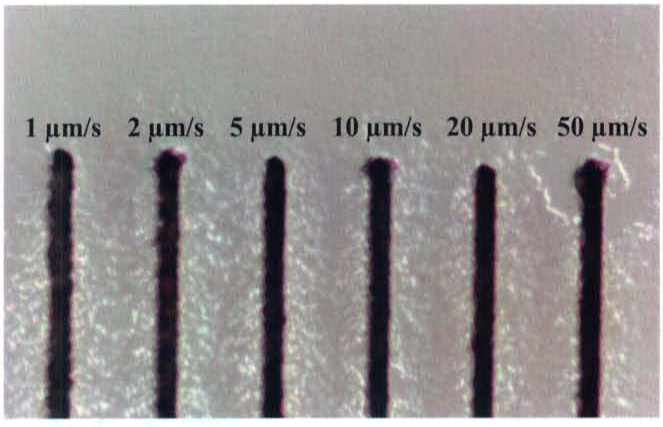

(a)

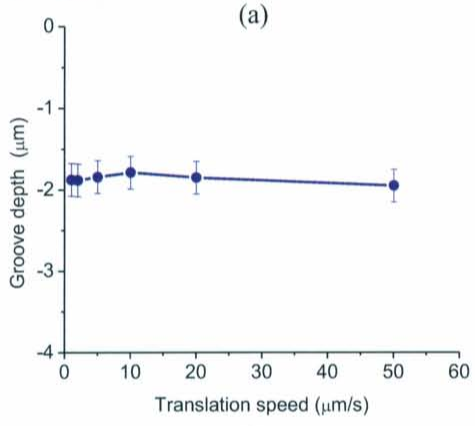

(b)

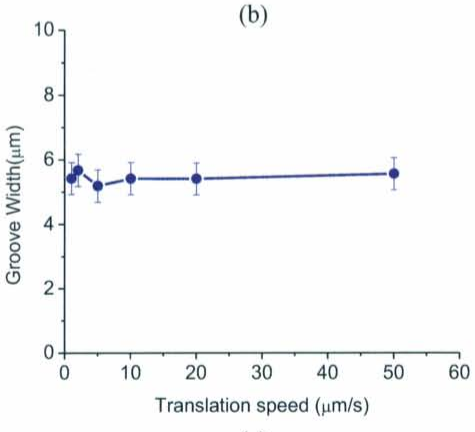

(c)

Figure 2-17 Grooves fabricated by the femtosecond laser of different translation speeds at a laser energy of 30 μJ/ pulse: (a) AFM image of sample; (b) and (c) the changes in the depth and width of grooves.

Chapter 3 Femtosecond laser microfabrication in bulk: waveguide fabrication

3.1 Introduction

As one of the key components of opto-microfluidic devices, integrated optical waveguides efficiently reduce the size of the devices. When a femtosecond laser is tightly focused into the bulk of fused silica, a permanent refractive-index increase is induced in the focus region. Compared with traditional waveguide fabrication techniques, such as MEMS, poured molding, and hot embossing, femtosecond waveguide writing exhibits unique advantages of three-dimensional, maskless fabrication with a single step. Figure 3-1 illustrates two kinds of type I waveguide writing methods by a femtosecond laser of low energy: transverse waveguide writing and longitudinal waveguide writing. The properties of waveguides vary significantly, depending on experimental setup, sample material, depth of the fabricated feature, microscope objective lens, repetition rate, etc. [198]. Eaton *et al.* reported that the waveguide with low loss was induced by increasing the repetition rate of a femtosecond laser due to heat accumulation effects, and a waveguide with ~0.2 dB/cm propagation loss was written by a femtosecond laser with 1 MHz repetition rate in an alkali-free borosilicate glass [199]. Will *et al.* demonstrated that the multimode waveguide in fused silica could be produced only by increasing the writing speed [200]. Complex photonic devices, such as splitters, gratings, and interferometers, were created at arbitrary depths inside the bulk of a sample to produce a lab-on-chip [201].

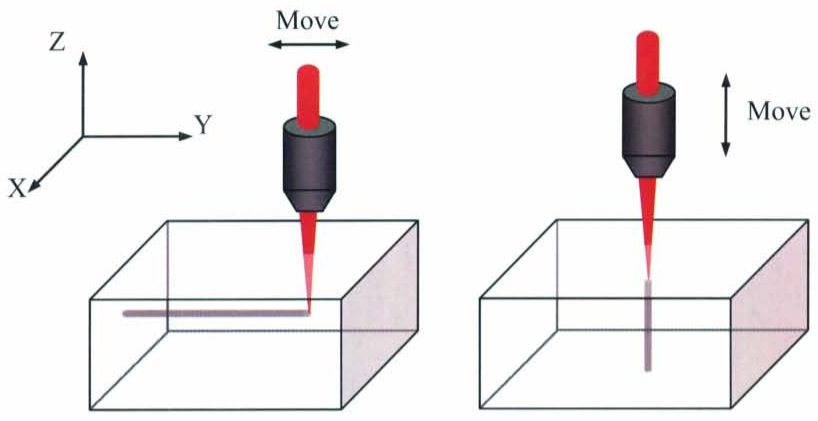

Figure 3-1 Schematic illustration of waveguide writing by a femtosecond laser: (a) transverse waveguide writing; (b) longitudinal waveguide writing.

Different mechanisms for a type I waveguide were proposed to explain the nature of the increase in the refractive-index, such as colour centre formation [202, 203], thermal effect [204], and densification [203, 205]. However, none of these hypotheses provides sufficient evident to support them [206]. The theory of nonlinear processing induced refractive index increase is generally accepted.

In 2001, Chan *et al.* proposed the use of a confocal spectroscopy setup to survey the type I waveguide in the bulk of the sample, in which Raman and fluorescence spectra measurements indicated the structural changes of fused silica in the modified region [205]. Nowadays, Raman spectroscopy has been shown to be a powerful tool to reveal the characteristics of femtosecond laser-induced waveguides in various materials [207-209]. In addition, the spatial distribution maps of the Raman intensity and peak shift in the transverse plane to the waveguide, which could be obtained from a high resolution scanning confocal microscope, provide more direct analysis of laser-matter interaction [210-213].

When lines are written with low pulse energy (below the damage threshold of the material), a type I waveguide appears at the focus region. However, when the pulse laser with a pulse energy above the damage threshold of the material focuses on the bulk of the sample, a type II waveguide structure is fabricated. As shown in Fig. 3-2, two parallel lines are fabricated in the bulk of the sample. The centre region, which has a higher refractive index than the focus regions, can transmit light as an optical waveguide. Several research groups succeeded in fabricating type II waveguides in fused silica, Yb-doped $KY(WO_4)_2$ crystals, lithium niobate and $LiNbO_3$, and corresponding near-field and refractive index profiles have been reported [210, 214-218].

In this chapter, different type II waveguides are fabricated in the bulk of fused silica samples. After fabrication, the edges of the sample are polished with polishing paper (3M®, 30 μm, 15 μm, 9 μm, 5 μm, 3 μm, 1 μm, and 0.5 μm grit) to reduce the coupling loss. The distributions of the Raman intensity in the waveguide focal plane as indicates by the dashed line in Fig. 3-3 and the near-field images of waveguides with different fabricated parameters are studied.

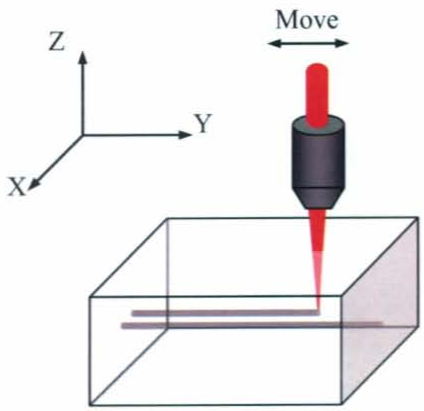

Figure 3-2 Schematic illustration of a type II waveguide writing.

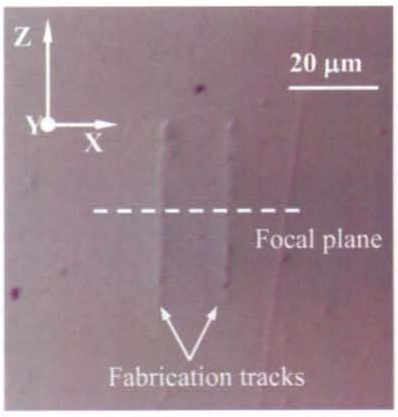

Figure 3-3 Location for Raman spectra analysis.

3.2 Raman spectra of waveguides in fused silica

When light encounters atoms or molecules, most incident photons are scattered with the same energy and wavelength. This kind of elastic scattering is Rayleigh scattering. However, a small fraction of the incident photons interacts with atoms or molecules in the sample, and gains or loses energy. As a result, the scattered photons exhibit shifts in frequency. Such inelastic scattering is referred to as Raman scattering. Raman scattering can occur accompanying a change in vibrational, rotational or electronic energy of a molecule. A spectral analysis of the scattered light provides a fingerprint to quickly identify and analyze molecules.

Silicon dioxide (SiO_2) can be described as a tetrahedron with four oxygen atoms surrounding a silicon atom. Figure 3-4 (a) shows the molecular structure of SiO_2. Fused silica is a high-purity synthetic silicon dioxide in amorphous (non-crystalline) form. The three-, five- and six-membered ring structures of fused silica are shown in Fig. 3-4 (b). The greater the number of three-membered ring structures a fused silica has, the higher its density due to less empty space in the three-membered ring structure.

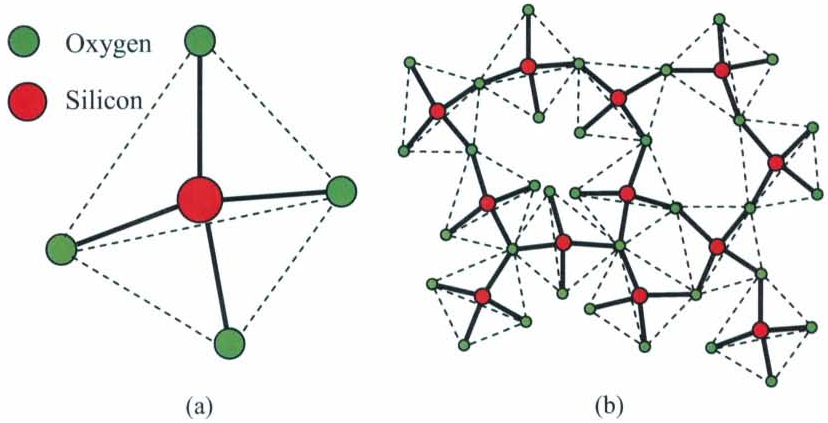

Figure 3-4 Molecular structures of (a) SiO_2 and (b) fused silica.

Figure 3-5 is the Raman spectrum of pristine fused silica without femtosecond laser irradiation. The spectrum is obtained from a confocal Raman spectrometer (HORIBA LabRAM, 100 mW, 532 nm diode laser, grating with 1800 lines/mm). The green laser beam is focused onto the sample with an objective lens of magnification of 100× and a pinhole of 50-microns. The collection time is 60 seconds per spectrum. The peaks of 605 cm^{-1} and 490 cm^{-1} (D_2 and D_1) are related to oxygen symmetric stretching motions in three-and four-membered ring structures. The peak 800 cm^{-1} (ω_2) is due to bending motions involving primarily oxygen. The intensity of the 800 cm^{-1} peak scales with the total intensity. The peak 1060 cm^{-1} (ω_3) is due to out-of-phase and in-phase stretching motions, primarily of oxygen, with little silicon motion. The intensity ratio between the 605 cm^{-1} Raman peak and the total Raman intensity will increase with the increase of fused silica density. Meanwhile, the densification is also accompanied by a downshift of the peak frequency at 1060 cm^{-1}. The shift can be attributed to both an increase in the Si–O bond length and a decrease in the mean Si–O–Si angle [205, 219, 220].

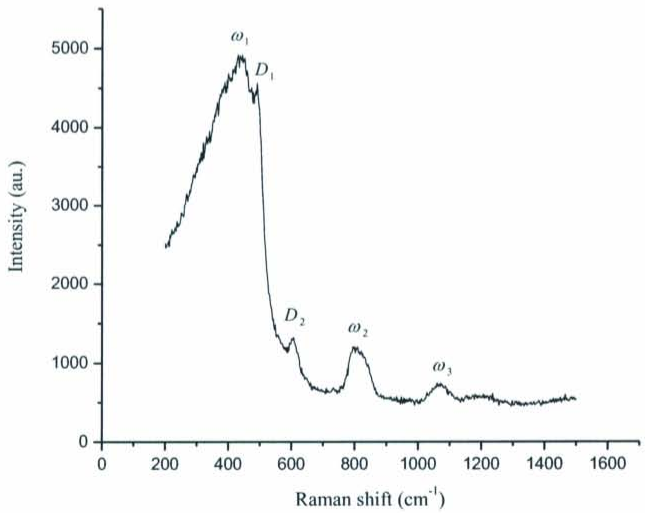

Figure 3-5 Raman spectrum of fused silica.

3.2.1 Raman spectra of femtosecond laser fabricated pits

Figure 3-6 is an optical micrograph of a pit fabricated by 10^4 femtosecond laser pulses with a pulse energy of 15 μJ/ pulse and a depth of 20 μm below the surface. In order to obtain a Raman signal coming from the desired region (pit), the fabricated sample is first mounted on the motion stages of the Raman spectrometer. A white light beam is focused on the bulk of the sample at the same depth (20 μm) as the femtosecond laser by moving the Z stage. Then the fabricated pit is located with the help of a CCD camera by moving the XY motion stage. Finally, a diode laser replaces the white light beam to irradiate the same position to obtain Raman spectra. Figure 3-7 shows the Raman spectra at different locations around the pit. The rising tails in the Raman spectra are due to fluorescence. Non-bridging oxygen hole centers (NBOHC) form during femtosecond laser modification and thus induce fluorescence. The rising tails are more obvious towards the pit centre which complicates the accurate evaluation of Raman peak shift at 1060 cm^{-1}. For this reason, the ratio of peak areas (605/800 cm^{-1}) is used to evaluate the change of refractive index instead of peak downshift at 1060 cm^{-1}.

3.2.2 Raman spectra of femtosecond laser fabricated lines

As shown in Fig. 3-8, after subtracting the baseline, Gaussian fit and peak integration using Origin software, the ratio of peak areas (605/800 cm^{-1}) can be easily obtained. Figure 3-9 shows the changes in the ratio of the peak areas of single lines at different pulse energies. The reference ratio is the peak area ratio of the material without femtosecond laser irradiation. The ratios increase significantly near the locations of the

fabricated line which means the density and refractive index of the material at the corresponding location increase. Therefore, stress-induced guiding regions appear at both sides of the femtosecond laser irradiated line. The size of the guiding region increases with the increase of the pulse energy, which is due to the fact that higher laser energies induce stronger stress. In addition, the higher energy induces a fabricated line of larger width. On average, this approach could produce a 2~4 μm guiding region for waveguiding. Figure 3-10 is a near-field image of a single line coupled with a He-Ne laser of 632.8 nm. The line is fabricated by a pulse energy of 1.5 μJ with an objective lens of magnification 20× (0.46 NA) at a writing speed of 100 μm/s. The two bright spots on both sides of the black line (fabricated line) also demonstrate the presence of guiding regions.

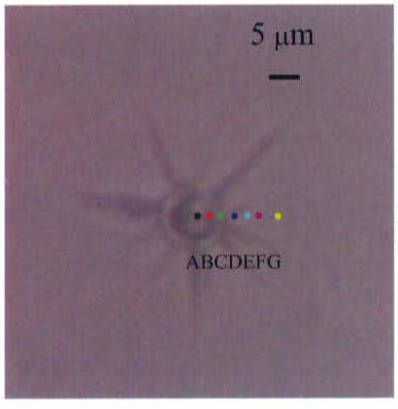

Figure 3-6 A pit fabricated by 10^4 pulses with the femtosecond laser of 15 μJ pulse energy. The pit is located at a depth of 20 μm below the sample surface.

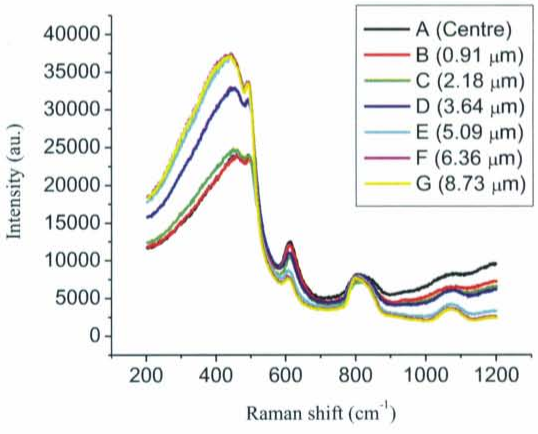

Figure 3-7 Raman spectra at different locations.

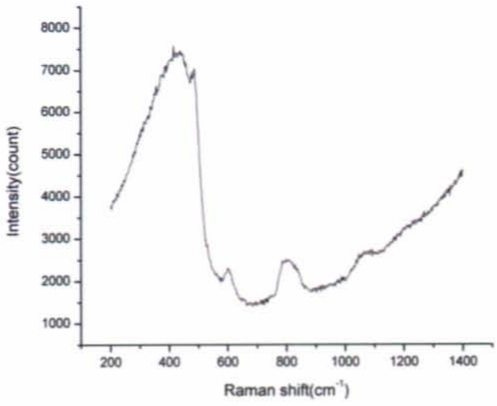

(a)

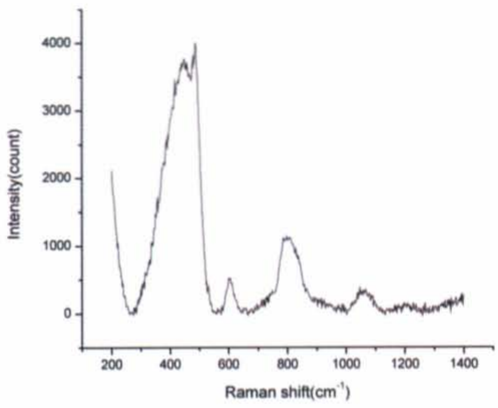

(b)

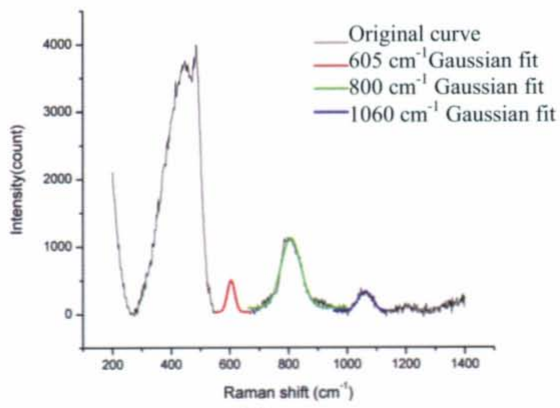

(c)

Figure 3-8 Procedures to analyze the peak areas at 605, 800, and 1060 cm^{-1}: (a) original Raman spectrum; (b) baseline subtraction; (c) Gaussian fit followed by peak integration.

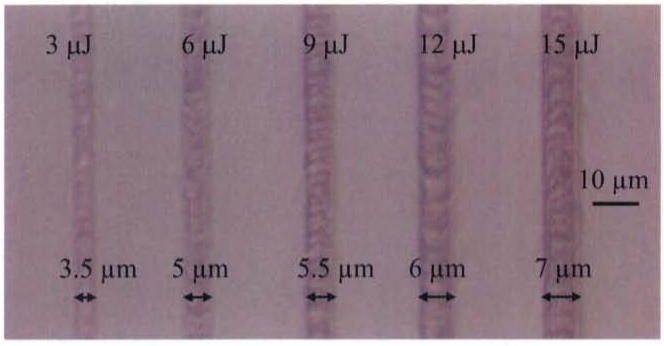

(a)

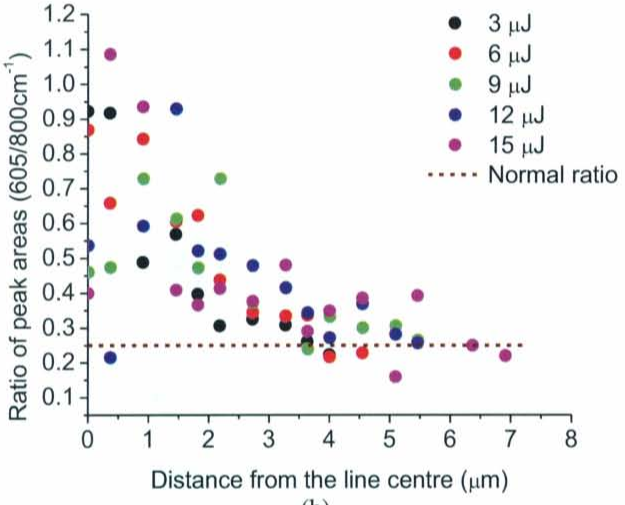

(b)

Figure 3-9 (a) An optical micrograph of lines fabricated by femtosecond laser of different pulse energies at a depth of 20 μm below the surface. Writing speed is 5 μm/s; (b) ratio of peak areas (605/800 cm^{-1}) at different locations.

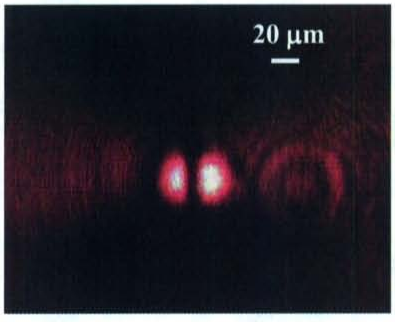

Figure 3-10 Near-field image of a single line coupled with a He-Ne laser of 632.8 nm.

3.2.3 Raman spectra of femtosecond laser fabricated double lines

The stress induced guiding region between two lines can be used as a waveguide. Figure 3-11 shows the spectra changes of the double lines with different separations. Lines are fabricated by femtosecond lasers of 12 μJ pulse energy with a writing speed of 5 μm/s at a depth of 20 μm below the surface. Compared with traditional optical waveguides such as the fiber and type I waveguide, the refractive index of the core is not uniform in the type II waveguide, which has a low refractive index in the core centre and a high refractive index in the core fringe. This phenomenon is more obvious in double lines with larger separations. The refractive index in the centre region is unchanged (over a length of 10 μm) (Fig. 3-11 (e)).

Figure 3-12 shows type II waveguides fabricated by different numbers of scans with the femtosecond laser of 11 μJ pulse energy at a depth of 30 μm below the surface. The separation between the two lines is 15 μm. The writing speed is 10 μm/s. There is no significant difference in the ratios of peak areas after multi-scan (Fig. 3-12). The effects of multi-scan on the waveguide transmission is studied in the next section.

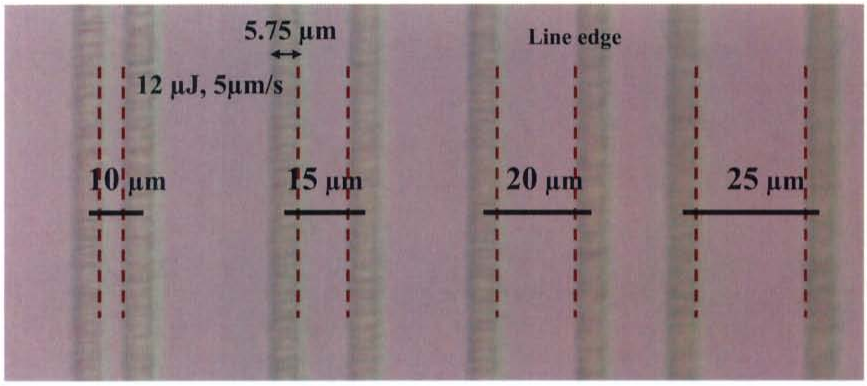

(a)

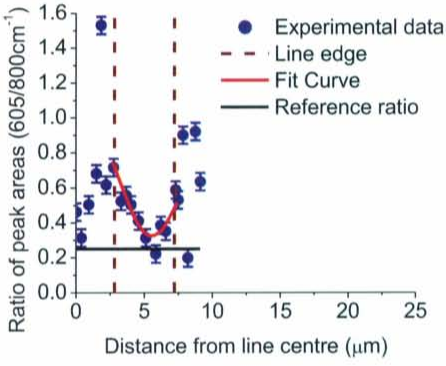

(b)

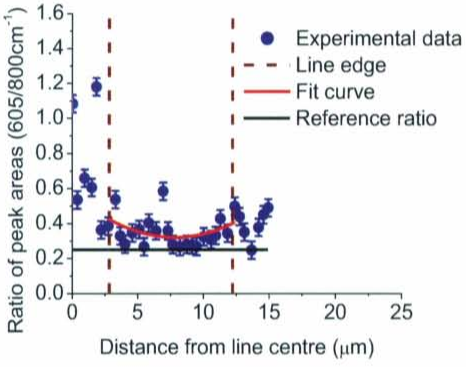

(c)

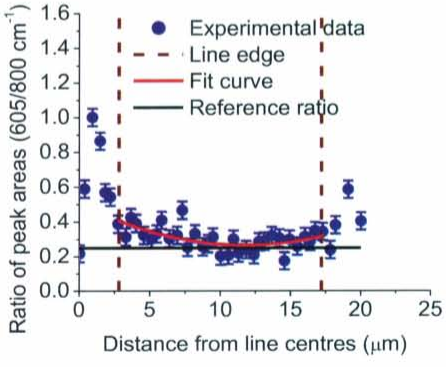

(d)

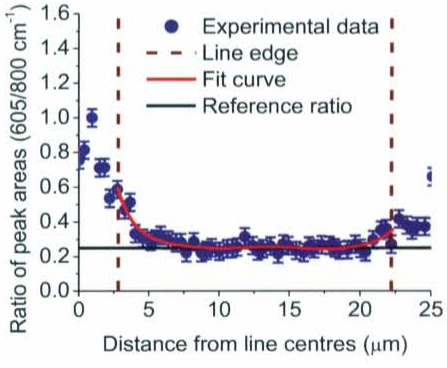

(e)

Figure 3-11 (a) An optical micrograph of femtosecond laser fabricated double lines with different separations; (b), (c), (d) and (e) the changes in the ratios of the peak areas in Raman spectra for the cases of double line with separations of 10, 15, 20, and 25 μm, respectively.

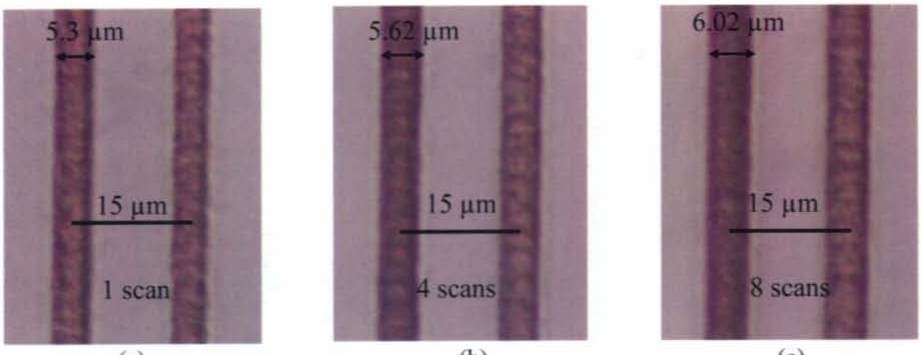

(a) (b) (c)

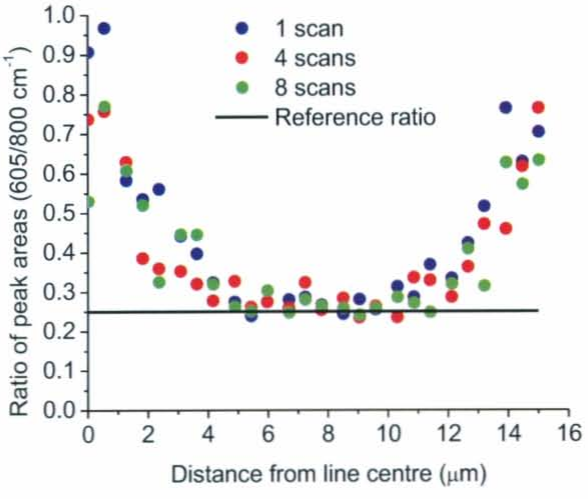

(d)

Figure 3-12 (a), (b) and (c) Optical micrographs of pairs of lines fabricated by femtosecond lasers of 11 μJ at a depth of 30 μm below the surface. Writing speed is 10 μm/s. The distance between two lines is 15 μm; (d) the changes in the ratios of the peak areas in Raman spectra after different numbers of scans.

3.2.4 Effects of polarization

Polarization is another important parameter in laser fabrication which may induce significantly different laser-matter interactions. Bellouard *et al.* [221] reported that the longitudinal polarization (electrical field parallel to the laser writing direction) induced a larger material density than the transverse polarization (electrical field perpendicular to the laser writing direction) in low energy irradiation due to polarization dependent nano-grating generation in the focus region. Here, we study the effects of polarization on femtosecond laser microfabrication in fused silica in the high energy case.

Figures 3-13 and 3-14 show the changes in the ratio of peak areas of single lines fabricated by either longitudinal or transverse polarization. It is evident that no obvious difference could be found between the two polarizations, which are also in agreement with the results in Fig. 3-15. The reason is that high laser energy significantly alters the structure of the samples. The polarization-dependent nano-gratings are destroyed in the high energy case [222]. Therefore, all the type II waveguides discussed in the next section are fabricated by the femtosecond laser of longitudinal polarization.

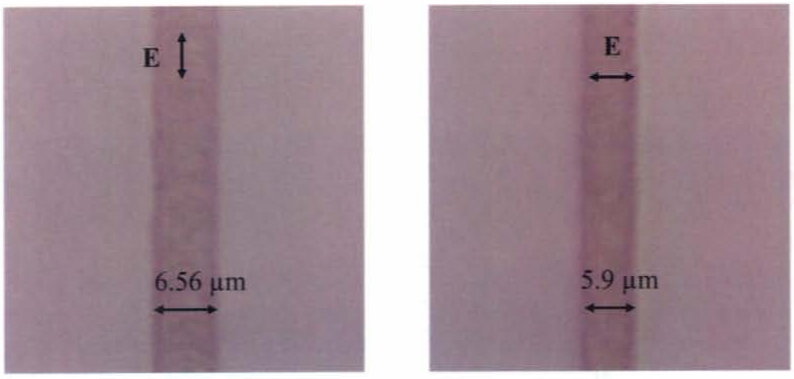

(a)

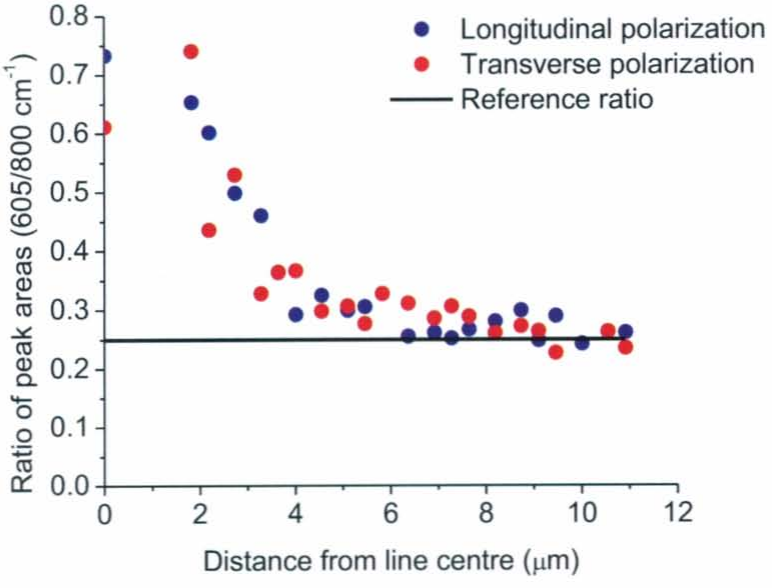

(b)

Figure 3-13 (a) Optical micrographs of lines fabricated by femtosecond laser beams of different polarizations with a 12 μJ pulse energy at a depth of 20 μm below the surface. Writing speed is 5 μm/s; (b) the changes in the ratio of peak areas of Raman spectra for the femtosecond laser beams of different polarizations.

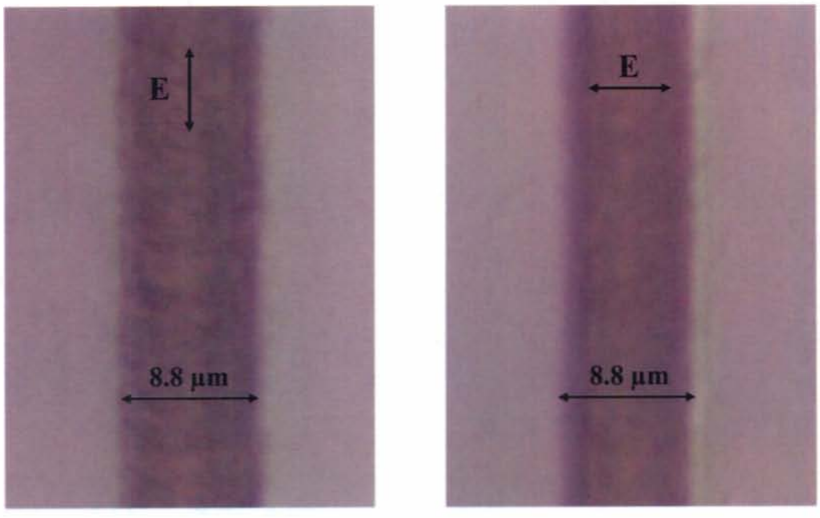

(a)

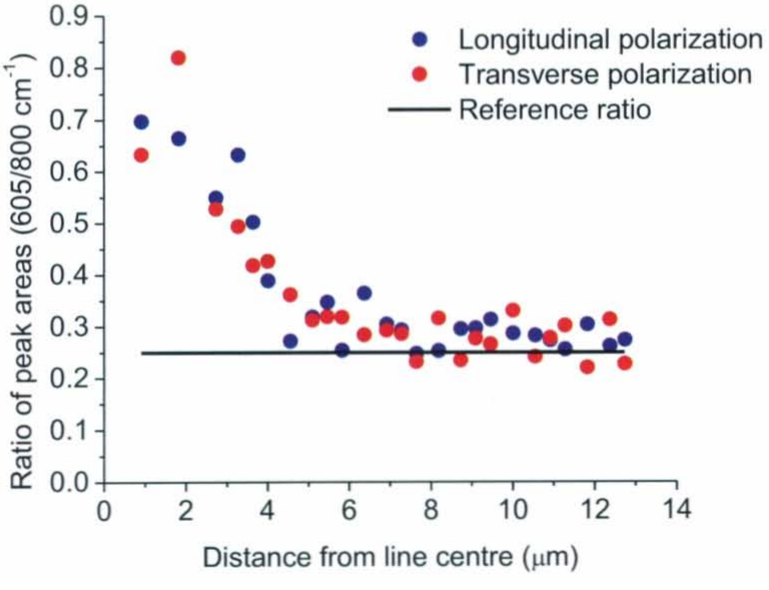

(b)

Figure 3-14 (a) Optical micrographs of lines fabricated by femtosecond laser beams of different polarizations with a 25 μJ pulse energy at a depth of 40 μm below the surface. Writing speed is 5 μm/s; (b) the changes in the ratio of peak areas of Raman spectra for the femtosecond laser beams of different polarizations.

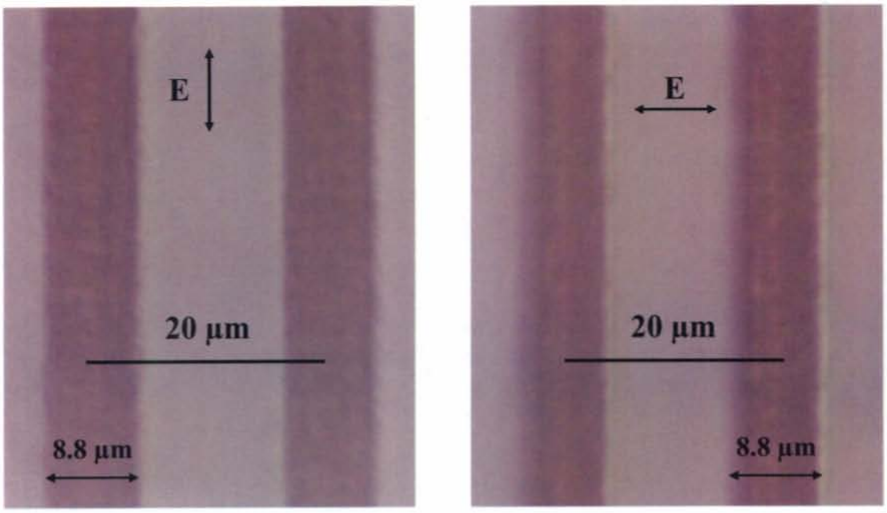

(a)

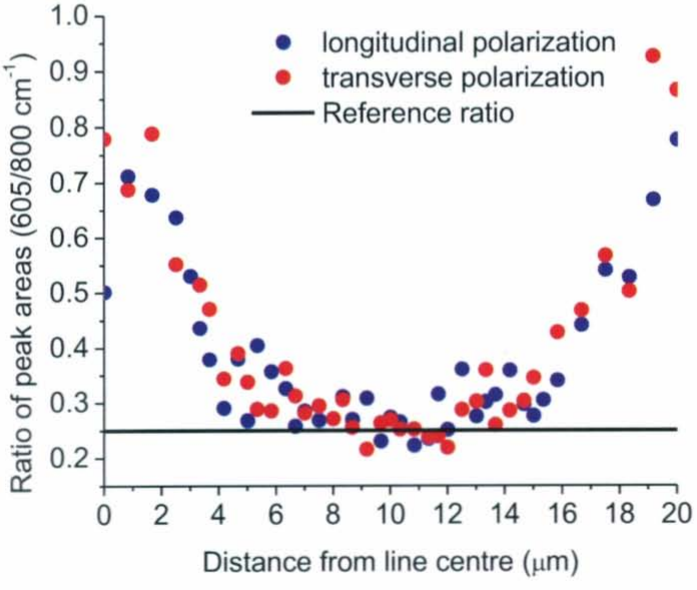

(b)

Figure 3-15 (a) Optical micrographs of double lines fabricated by femtosecond laser beams of different polarizations with a 25 μJ pulse energy at a depth of 40 μm below the surface. The writing speed is 5 μm/s; (b) the changes in the ratio of peak areas of Raman spectra for the femtosecond laser beams of different polarizations.

3.3 Waveguide characterization

The home-made experimental setup for coupling a laser into a waveguide is shown in Fig. 3-16. A He-Ne laser source with a wavelength of 632.8 nm is used to coarsely align a waveguide at first. A tunable laser source (Hewlett Packard 8168F) is used to characterize the waveguide. The output wavelength of the tunable laser ranges from 1460 to 1590 nm. 0.1 mW CW light emitted from the tunable laser is coupled into a short section of single-mode fiber (P1-7324-FC) through an FC/APC connector. The other end of the fiber is placed into a fiber chuck with chuck holder (Fig. 3-17) and mounted on XYZ stages for alignment in order to optimize waveguide coupling. The transmitted light is focused by a 100× microscope objective lens (0.95 NA), and collected by a camera head with camera controller (Hamamatsu, C2741) which is connected to a computer. The near-field image of the transmitted light is captured by FlashBus spectrim software. Optimized waveguide coupling is achieved by carefully adjusting XYZ stages, which is achieved when the exiting light from the waveguide reaches the maximum brightness.

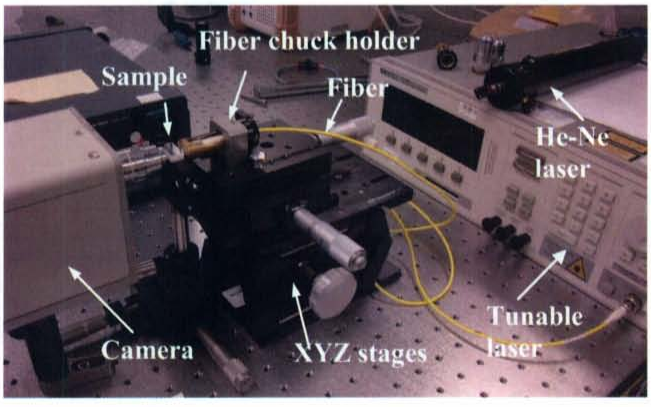

Figure 3-16 Photograph of the experimental setup for coupling laser light into waveguides.

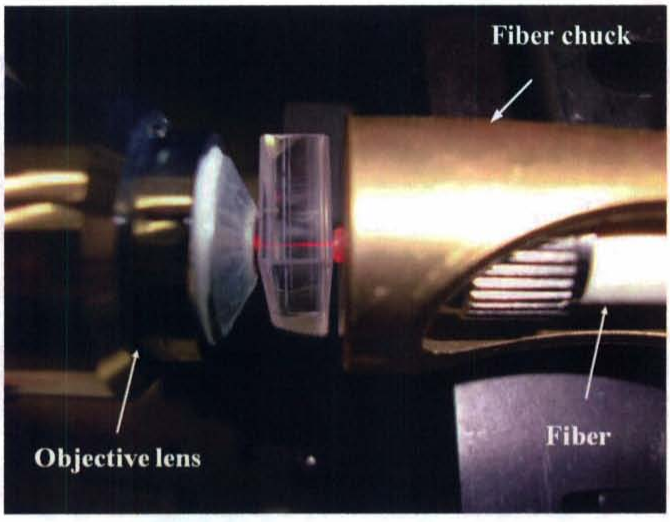

Figure 3-17 Type II waveguide coupling in fused silica using a He-Ne laser at 632.8 nm.

3.3.1 Effects of separation between lines

Near-field images of waveguides are shown in Fig. 3-18. The waveguides are fabricated by a laser pulse energy of 15 μJ at a writing speed of 5 μm/s with twice scans. Laser light with a wavelength of 1550 nm, which show low absorption by fused silica, is coupled into the waveguide. An elliptical cross section of transmitted light demonstrates the success of type II waveguide fabrication and laser coupling. When the separation exceeds 30 μm, the waveguides show weak exiting light, as shown in Fig. 3-18 (c). Therefore, we usually choose 20 μm as the separation of type II waveguides.

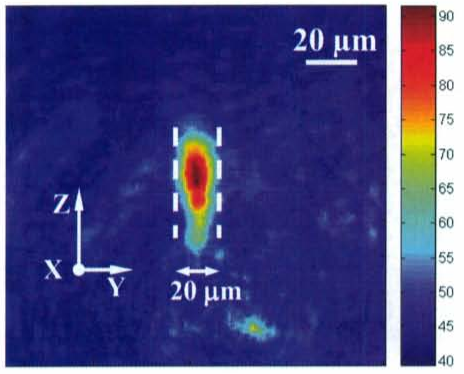

(a)

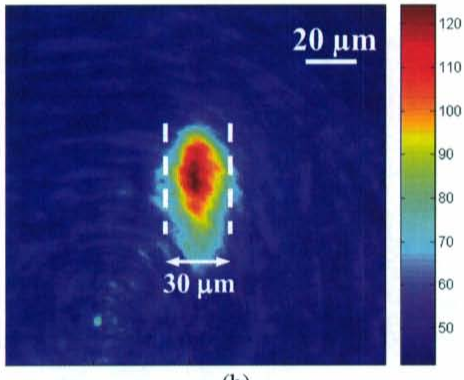

(b)

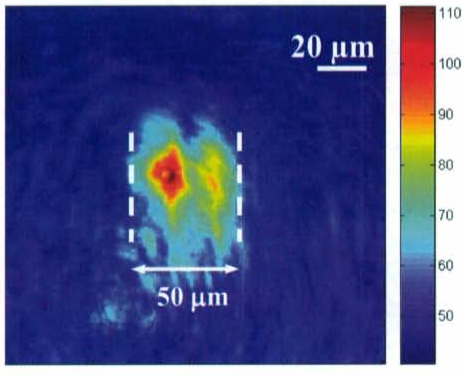

(c)

Figure 3-18 Near-field images of type II waveguides with different separations.

3.3.2 Effects of laser energy

The origin of the elliptical cross section of the waveguide depends on the length of the fabricated tracks. Lower fabrication energy can decrease the length of a track; so does the aspect ratio of the waveguide cross section (the ratio of its longer dimension to its shorter dimension). Figure 3-19 shows type II waveguides fabricated with different laser pulse energies. The shape of the waveguide cross section appears as a circle in Fig. 3-19 (d).

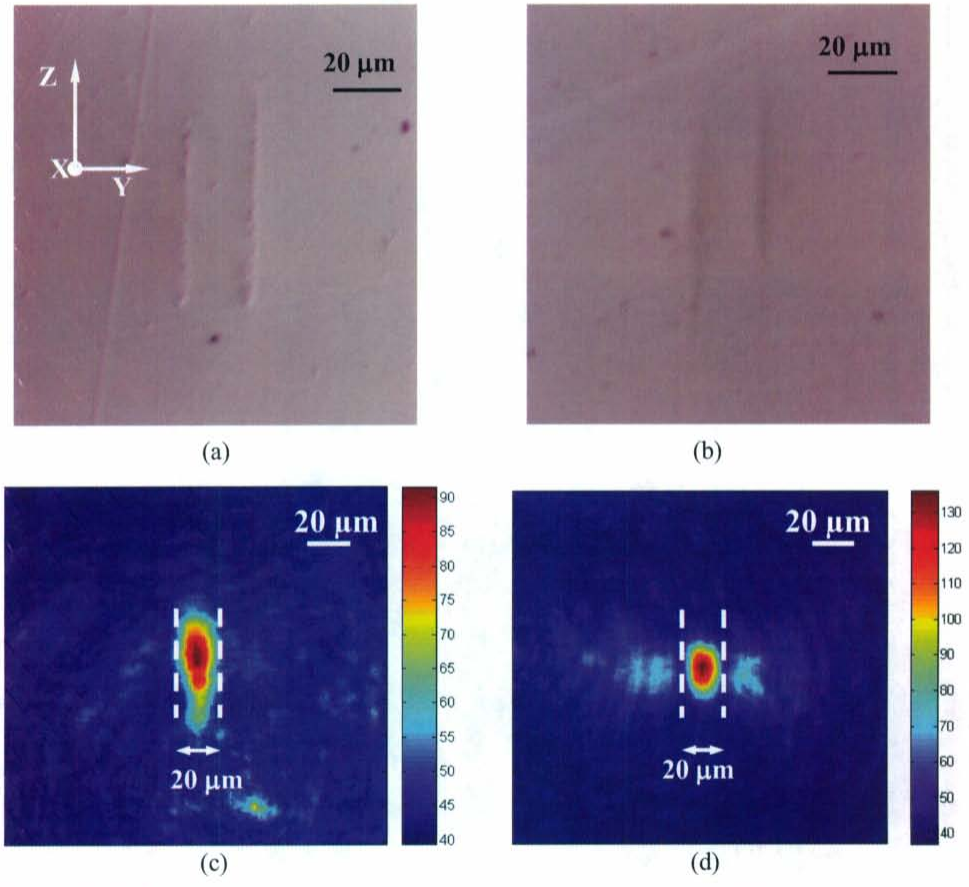

Figure 3-19 Cross section of a type II waveguide with a separation of 20 μm: (a) a waveguide fabricated by a laser pulse energy of 15 μJ at a writing speed of 10 μm/s; (b) a waveguide fabricated by a laser pulse energy of 10 μJ at a writing speed of 10 μm/s. All waveguides are 300 μm below the sample surface, and are scanned twice; (c) and (d) near-field images of (a) and (b), respectively.

3.3.3 Effects of a multi-scan

Figure 3-20 shows the near-field images of waveguides by multiple scans of the femtosecond laser. The waveguides are fabricated by a laser pulse energy of 15 μJ at a writing speed of 5 μm/s, and coupled with a laser of 1550 nm. The transmission loss is significant after one scan due to the fact that pulsed laser irradiation causes uneven micro-structures in the fabricated line, which induces inconsistent change in the refractive index along the X direction. After three scans, the waveguide exhibits a better guiding character which can be observed from the maximum intensity of the colourbar, as shown in Fig. 3-20 (c). Therefore, even though there is no obvious increase in the refractive index of the waveguide observed from the Raman spectra after a multi-scan, a multi-scan improves the uniformity of the change in the refractive index along the X direction.

3.3.4 Effects of writing speed

Near-field images of waveguides with different writing speeds are shown in Fig. 3-21. The waveguides are fabricated by a laser pulse energy of 15 μJ with twice scans and coupled with the laser at 1550 nm. There is no significant difference among these waveguides. The reason is that the changes in the refractive index are the same at the low writing speed due to the fact that the fabricated lines in the waveguide do not exhibit pronounced change after multi-pulse irradiation at the low writing speed, as mentioned in Section 2.4.2.

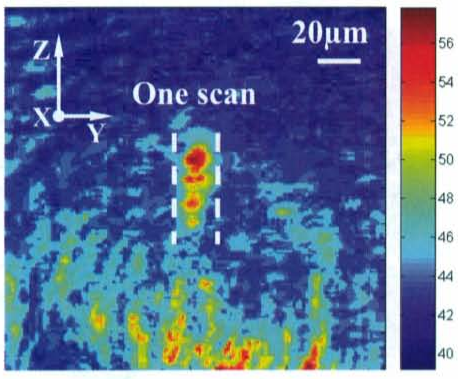

(a)

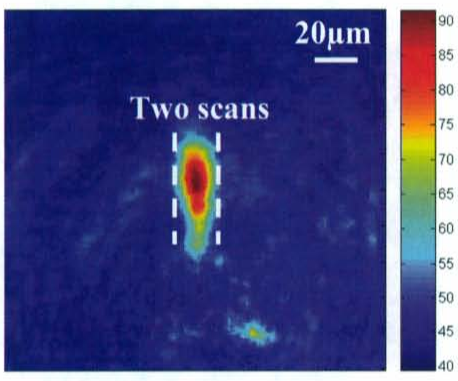

(b)

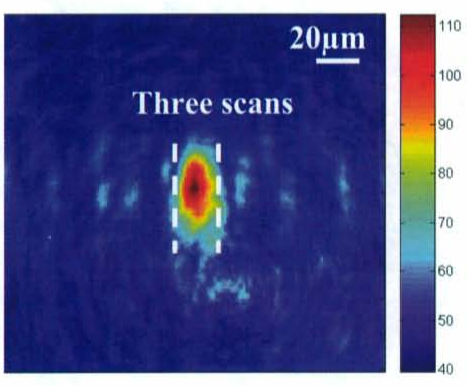

(c)

Figure 3-20 Near-field images of waveguides fabricated by a multi-scan of the femtosecond laser. The fabrication parameters of pulse energy, double line separation, and scan speed are 15 μJ, 20 μm, and 5 μm/s, respectively.

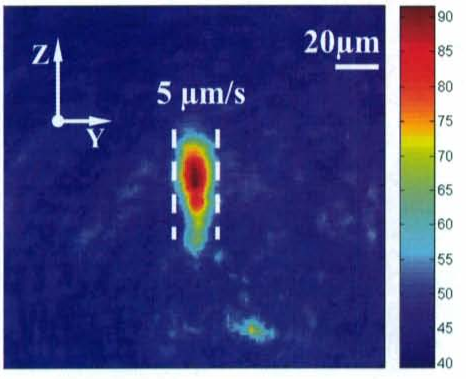

(a)

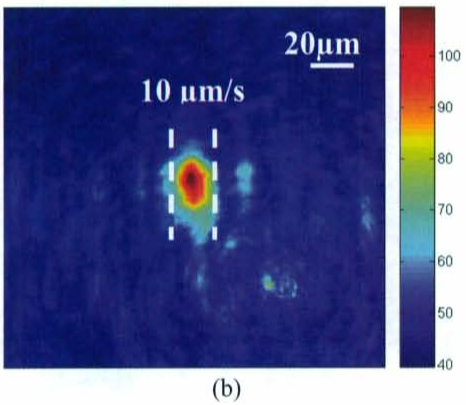

(b)

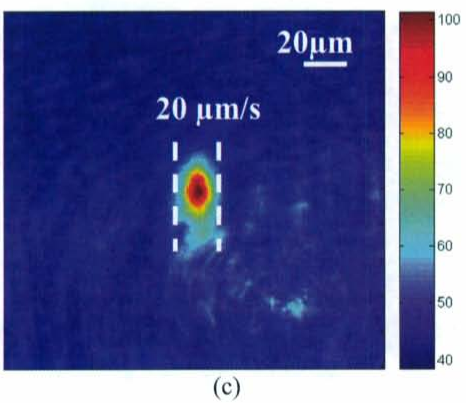

(c)

Figure 3-21 Near-field images of waveguides fabricated with the femtosecond laser of different writing speeds. The fabrication parameters of pulse energy, double line separation, and the number of scans are 15 μJ, 20 μm, and two, respectively.

3.3.5 Propagation loss

When light propagates along the waveguide, the intensity of the light continuously attenuates because of scattering and absorption. To measure the propagation loss, two waveguides with different lengths (1 cm and 0.5 cm) are fabricated with a laser pulse energy of 15 μJ with two scans at a writing speed of 10 μm/s. Near-field images of the waveguides are shown in Fig. 3-22. The near-field intensities from the two waveguides, *i.e.*, $I_{1\text{cm}}$ and $I_{0.5\text{cm}}$ are calculated from the images. From the following equation,

$$\text{Propagation Loss} = 2\times 10\log(\frac{I_{1cm}}{I_{0.5cm}})\ \text{dB/cm} \qquad (3.1)$$

we estimate that the waveguide propagation loss is ~4 dB/cm with these fabrication parameters. Compared with type I waveguides of a propagation loss of less than 1 dB/cm, the loss of a type II waveguide is larger. The main reason is that there are no distinct boundaries at the top and bottom parts of this type of waveguide, which results in significant light scattering. However, for the applications of these waveguides in opto-microfluidic devices, ~4 dB/cm propagation loss is acceptable (typical waveguide loss is 0.5 – 3.0 dB/cm).

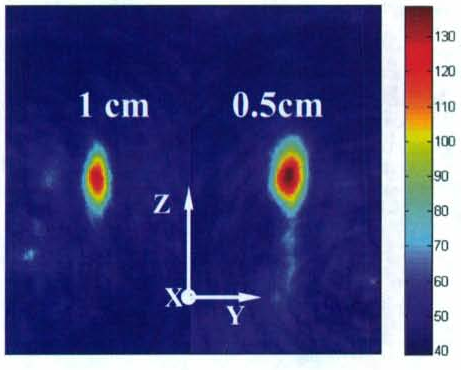

Figure 3-22 Near-field image of waveguides with different lengths.

3.4 Waveguides with complex structures

3.4.1 S-shaped waveguides

Compared to straight waveguides, S-shaped waveguides have larger propagation loss due to the fact that more scattering loss occurs at the bends. Small-angle bending introduces a smaller scattering loss. Figure 3-23 shows a schematic diagram and a near-field image of an S-shaped waveguide. The bending angle is about 0.76°. Figure 3-24 shows another S-shaped waveguide. The bending degree is about 26.6°. All waveguides are fabricated by a laser pulse energy of 15 μJ with two scans at a writing speed of 10 μm/s. Weak transmitted light with lower brightness in Fig. 3-24 (b) demonstrates that a higher propagation loss results in this case.

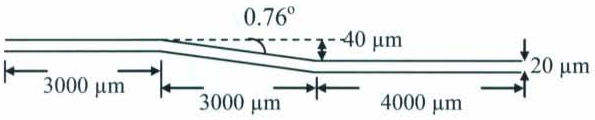

(a)

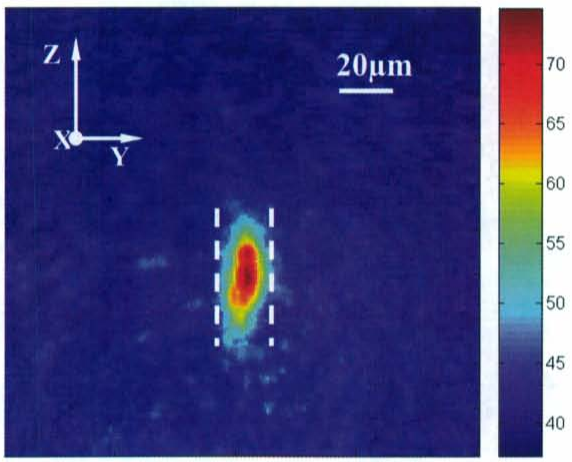

(b)

Figure 3-23 An S-shaped waveguide: (a) schematic diagram of an S-shaped waveguide with a bending angle of 0.76°; (b) near-field image of the S-shaped waveguides.

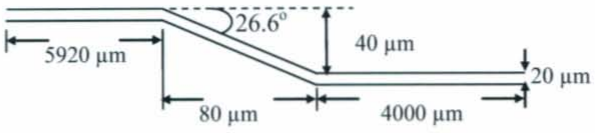

(a)

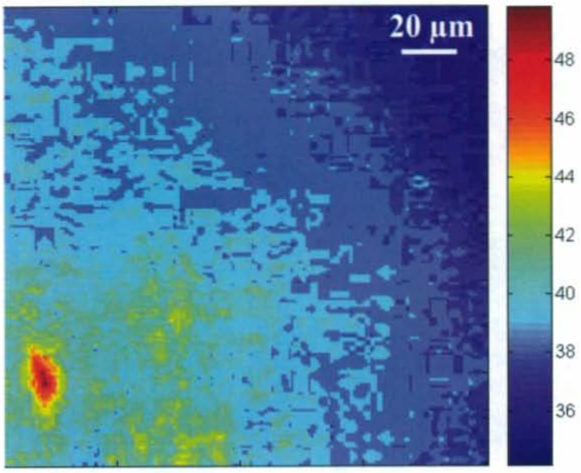

(b)

Figure 3-24 An S-shaped waveguide: (a) schematic diagram of an S-shaped waveguide with a bending angle of 26.6°; (b) near-field image of the S-shaped waveguide.

3.4.2 Y-shaped waveguides

Y-shaped waveguides play an important role in splitting or combining light, and are widely applied in opto-microfluidic devices to achieve specific optical functions. Similar to S-shaped waveguides, Y-shaped waveguides also possess relatively large scattering loss. Judging by the experimental result on S-shaped waveguides, Y-shaped waveguides with a small bending angle using a laser pulse energy of 15 μJ at a writing speed of 10 μm/s are fabricated. A laser beam with a power of 0.2 mW is coupled into one side of the waveguide with a separation of 30 μm, and then the laser beam is split into two beams

which are transmitted to the other side of the waveguide with a separation of 15 μm. Figures 3-25 and 3-26 are two examples of the Y-shaped waveguides. The near-field profiles display the feasibility of the Y-shaped waveguide. In addition, Fig. 3-26 (b) shows a better transmitted light due to a less bending angle.

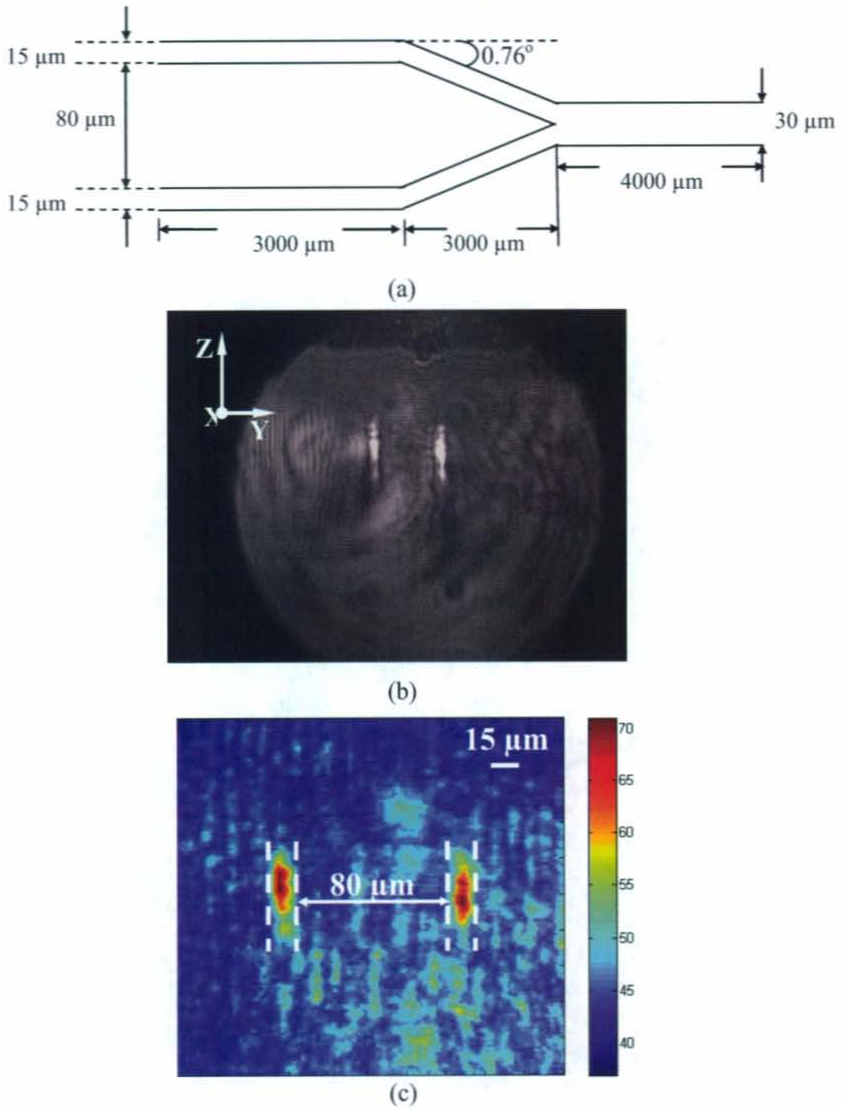

Figure 3-25 A Y-shaped waveguide: (a) schematic diagram of a Y-shaped waveguide with a bending angle of 0.76°; (b) and (c) near-field images of a Y-shaped waveguide coupled with lasers of wavelength 633 and 1550 nm, respectively.

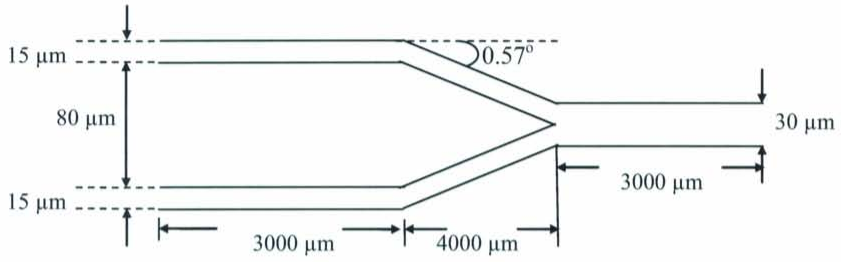

(a)

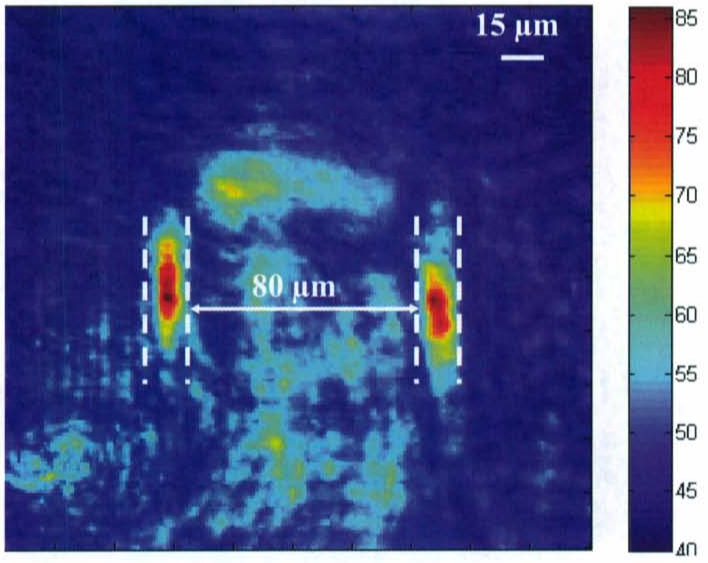

(b)

Figure 3-26 A Y-shaped waveguide: (a) schematic diagram of a Y-shaped waveguide with a bending angle of 0.57°; (b) near-field image of a Y-shaped waveguide coupled with a laser of wavelength1550 nm.

Chapter 4 Femtosecond laser microfabrication in bulk: microchannel fabrication

4.1 Introduction

As mentioned in Chapter 1, femtosecond laser irradiation assisted by HF acid etching can produce microchannels. The properties of the microchannels have been investigated by changing irradiation and etching parameters such as writing energy, writing speed, laser polarization, HF concentration and etching time [223-226]. Hnatovsky *et al.* reported that the etching rate of the microchannel strongly relies on the laser polarization in the low energies (~150 nJ) due to the presence of polarization-dependent self-ordered periodic nanocracks or nanoporous structures [222, 227]. The high dependence of the etching rate inside the focus region on the femtosecond laser wavelength in fused silica was observed and explained based on the fact that the fused silica has a higher damage threshold at a longer writing wavelength, by Sun *et al.* [228].

The reasons for the selective chemical etching can be explained by the fabrication mechanisms of the femtosecond laser. A periodic electron plasma concentration is generated by the interference of the incident laser field with the electron plasma density wave, and leads to the periodic structural changes (nanogratings or nanovoids) in the irradiated regions [229]. Although, the HF acid etches the whole sample (irradiated and unirradiated regions), the nanogratings and nanovoids cause the acid solution diffusing into the interior of fused silica to etch the material. Thus faster etching rate appears in the irradiated regions than that in the unirradiated regions.

In this chapter, we investigate the details of the technique for microchannel fabrication under different irradiation parameters. Intake apertures and shape-controlled microchannels fabrication are studied with the compensation fabrication method. Combining the optimized fabrication parameters, various microchannels with intakes are achieved. As shown in Fig. 4-1, we first irradiate the sample with the femtosecond laser, and then immerse the sample into a diluted HF acid solution of 20% in concentration. After several hours of etching, a microchannel is generated. Simultaneous sample rotation in rotary shakers is adopted to assist the etching process.

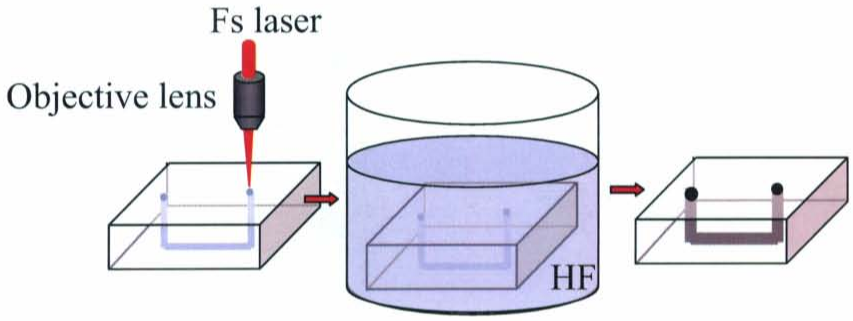

Figure 4-1 Schematic illustration of the procedure for etching-assisted femtosecond laser microfabrication.

4.2 Microchannel characterization

4.2.1 Effects of pulse energy

The common shape of the cross section of a microchannel is an ellipse, which is due to the nature of the Gaussian beam which induces an elliptical track in the bulk of samples (Fig. 3-19 (a) and (b)). As a result, an elliptical cross section is generated after HF acid solution etching (Fig. 4-2). Figure 4-3 shows the microchannels fabricated with

different pulse energies. The writing speed is 10 μm/s, and the etching duration is three hours. The transverse diameter of the cross section of the microchannel increases significantly as compared with the increase in the conjugate diameter. This result matches the Gaussian distribution of a laser beam. From the simulation of the intensity profile of a Gaussian beam (Fig. 2-9), the intensity distribution increases more remarkably along the Z axis than that along the X axis when the beam energy increases. Therefore, a higher pulse energy results in a larger cross section of the microchannel with a higher ratio of the transverse diameter to its conjugate diameter (aspect ratio). The lengths of the microchannels are about 1.31 mm, which have no obvious changes with the increase in laser pulse energy. The reason is that the high energy (much higher than the damage threshold) induces similar microstructures in the focus position which lead to the same etching rate by the HF acid.

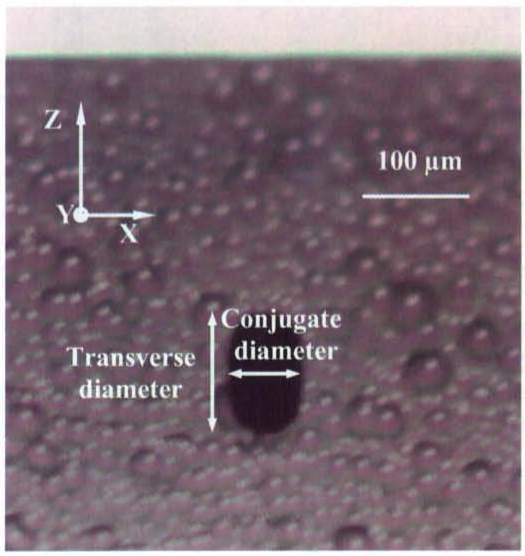

Figure 4-2 Elliptical cross section of a microchannel.

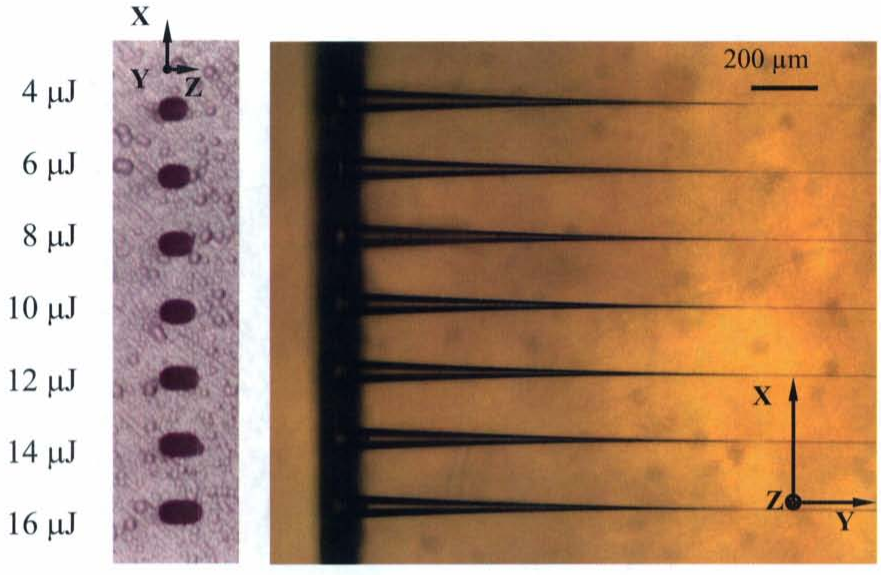

(a)

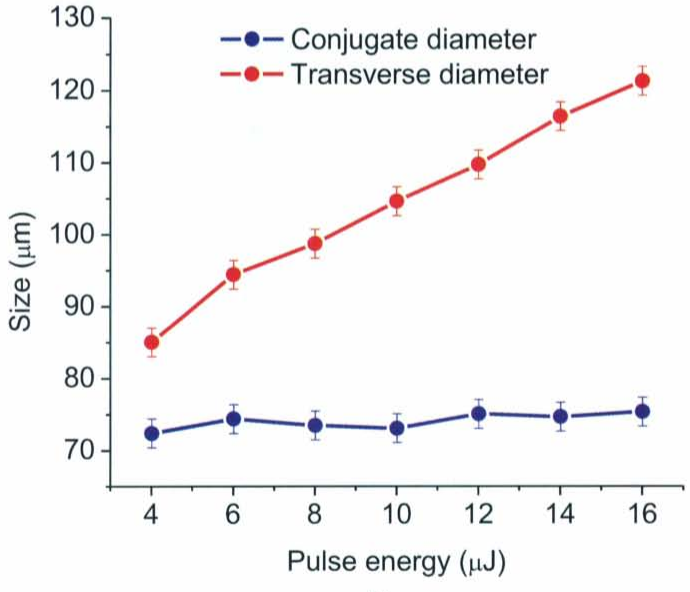

(b)

Figure 4-3 Microchannels fabricated with the femtosecond laser pulses of different energies at a writing speed of 10 μm/s followed by 3 hours of etching: (a) optical micrograph of microchannels observed from the end face (left) and above (right); (b) changes in the conjugate and transverse diameter of the cross sections with the increase in pulse energy.

4.2.2 Effects of writing speed

Figure 4-4 presents the microchannels fabricated with the femtosecond laser of the same pulse energy (10 μJ) but at different writing speeds, followed by etching with a diluted 20% HF solution for three hours. The results demonstrate that the writing speed in high energy cases has a minor effect on the microchannel etching at low writing speeds (less than 50 μm/s), which is similar to the results obtained in Section 2.4.2. However, in higher writing speed cases, less nanovoids are induced due to the fact that less laser pulses irradiate on the same location. In addition, high writing speed also causes discontinuous modifications in the focus position. As a result, the cross section and the length of the microchannel significantly decrease as shown for the case of 800 μm/s in Fig 4-4 (b).

4.2.3 Effects of polarization

As mentioned before, polarization-dependent nanostructures ablated by a femtosecond laser with low energy play a great role in the sample etching rate. Our experiments in the high pulse energy case, performed at a pulse energy of 10 μJ, a writing speed of 10 μm/s, and an etching time of 3 hours in 20% HF solution, indicate that the polarization has no significant impact on the microchannel fabrication, as shown in Fig. 4-5. The reason is that disruptive modifications like voids and micro-explosions replace the polarization-dependent structures in the high energy as mentioned before.

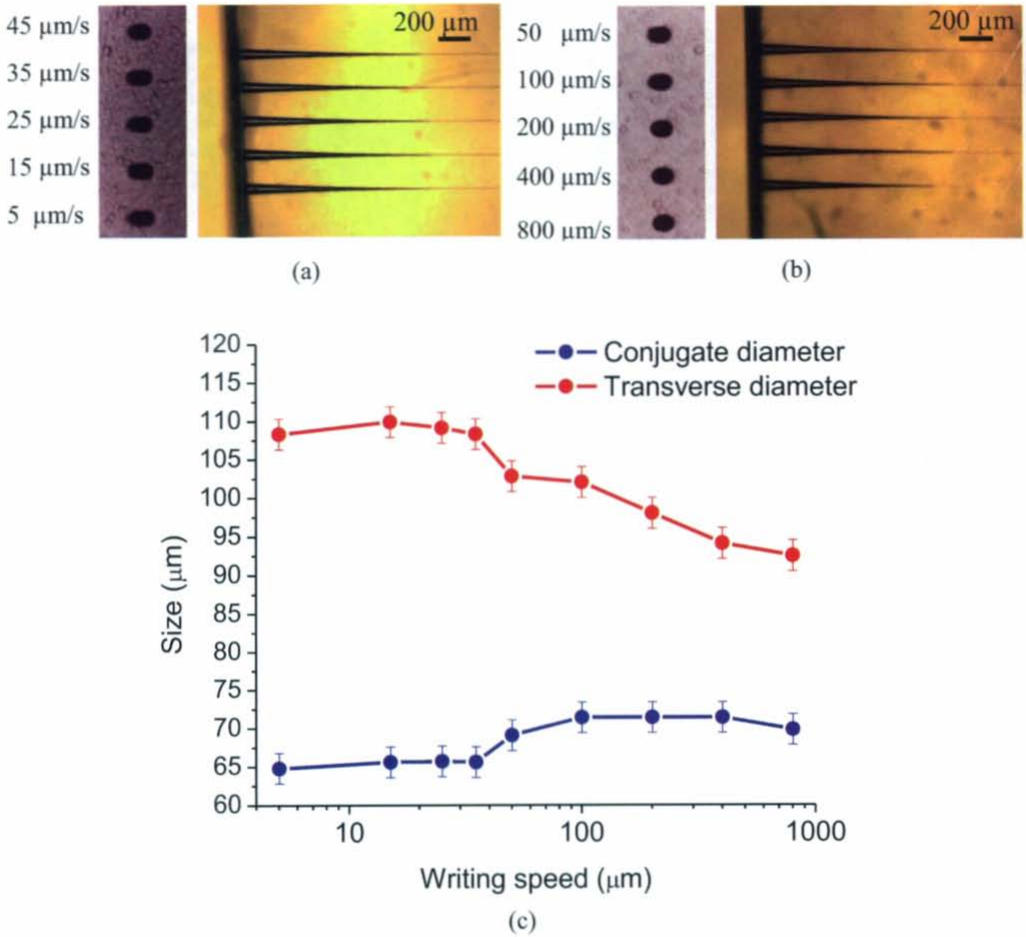

Figure 4-4 Microchannels fabricated with the femtosecond laser of 10 μJ/pulse at the different writing speeds, followed by 3 hours of etching: (a) and (b) optical micrographs of microchannels observed from the end face (left) and above (right); (c) changes in the conjugate and transverse diameter of the cross sections with the increase in the writing speed.

4.2.4 Effects of number of scans

In Section 3.3.3, we mentioned that multi-scaning affects the ablating structures by improving the uniformity of the ablating tracks. For the study here, multi-scan tracks are fabricated by femtosecond laser pulses with a pulse energy of 10 μJ, a writing speed of 10 μm/s, and followed by etching for 3 hours in 20% HF solution. The experimental results indicate that there is no pronounced difference between the resultant microchannels (Fig. 4-6). Therefore, in the next microchannel fabrication, we choosed the fabrication parameters as: 10 μJ pulse energy, 10 μm/s writing speed, longitudinal polarization, and single scan.

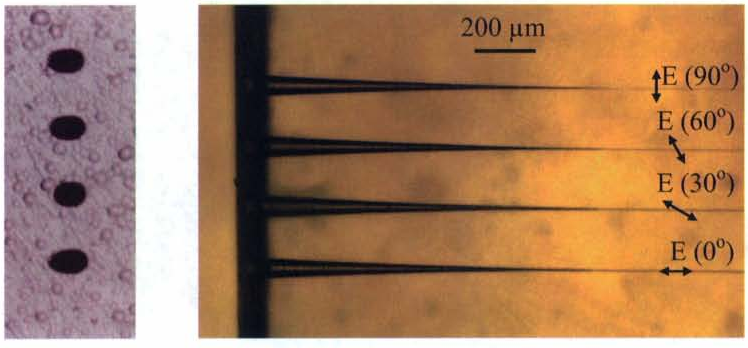

(a) (b)

Figure 4-5 Microchannels fabricated with the femtosecond laser of a 10 μJ/pulse in different polarizations at the writing speed of 10 μm/s, followed by 3 hours of etching: (a) optical micrograph of microchannels observed from the end face, and (b) optical micrograph of microchannels observed from above.

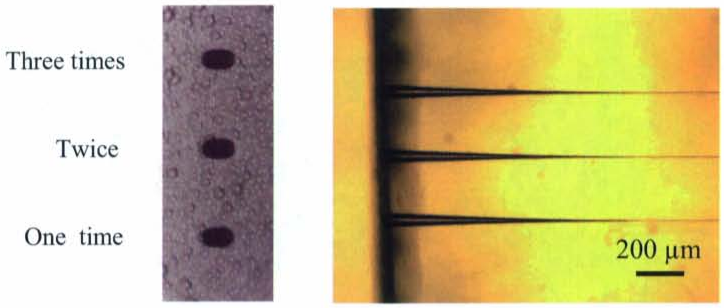

(a) (b)

Figure 4-6 Microchannels fabricated with the femtosecond laser of 10 μJ/pulse in different numbers of scans at the writing speed of 10 μm/s, followed by 3 hours of etching: (a) optical micrograph of microchannels observed from the end face, and (b) optical micrograph of microchannels observed from above.

4.2.5 Roughness of microchannels

Roughness of the microchannels is an important aspect for their applications in opto-microfluidic devices. Large roughness not only influences the flow of liquid in the microchannels, but also blocks the optical signals from being transmitted efficiently. However, it is difficult to directly measure the roughness of the microchannel inside the bulk sample using an available technique. In our study, we focus the femtosecond laser beam 30 μm below the sample surface to fabricate tracks. After 5 hours of 20% HF acid solution etching, the upper layer fused silica is eroded, and the microchannel is exposed; thus, the roughness of the fabricated microchannel is studied using a scanning electron microscope (SEM, Hitachi S-570).

4.2.5.1 Effects of pulse energy

Figure 4-7 shows SEM micrographs of the structures of exposed microchannels fabricated with femtosecond laser beams of different pulse energies at a writing speed of

50 μm/s. The polarization direction is perpendicular to the writing direction. The results indicate that the pulse energy has no significant effect on the roughness of the microchannels. Some tiny patterns with sizes less than 1μm appear on the wall of the microchannel, which are caused by disruptive modification. When HF acid seeps into the voids and micro-explosion cracks, it maintains a longer etching time in these places than in others; thus, the shapes of voids and micro-explosion cracks are recorded on the wall of the microchannel.

4.2.5.2 Effects of polarization

Figure 4-8 shows the structures of exposed microchannels fabricated with the femtosecond laser of a pulse energy of 10 μJ in different polarizations and a writing speed of 50 μm/s. The polarization shows no significant effects on the roughness of the microchannels.

4.2.5.3 Effects of writing speed

The morphologies of the microchannels fabricated with the femtosecond laser of a pulse energy of 10 μJ at different writing speeds are shown in Fig. 4-9, in which the polarization direction is perpendicular to the writing direction. Microchannels fabricated in lower writing speeds have a smaller roughness due to the fact that more uniform destructive structures replace the nanovoids and nanocracks after multi-pulse irradiation.

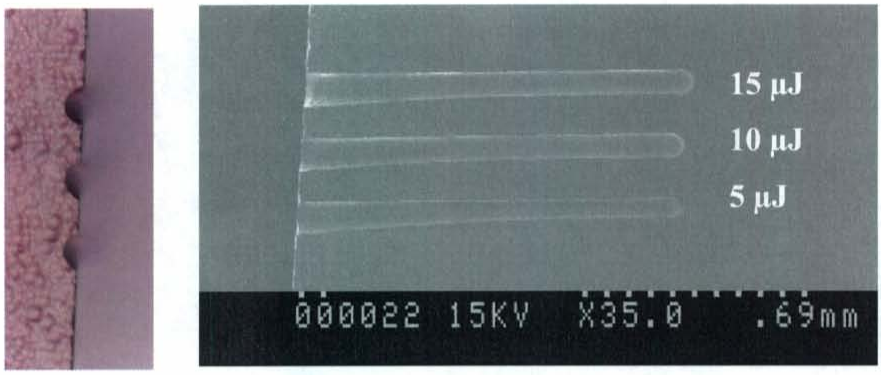

(a) (b)

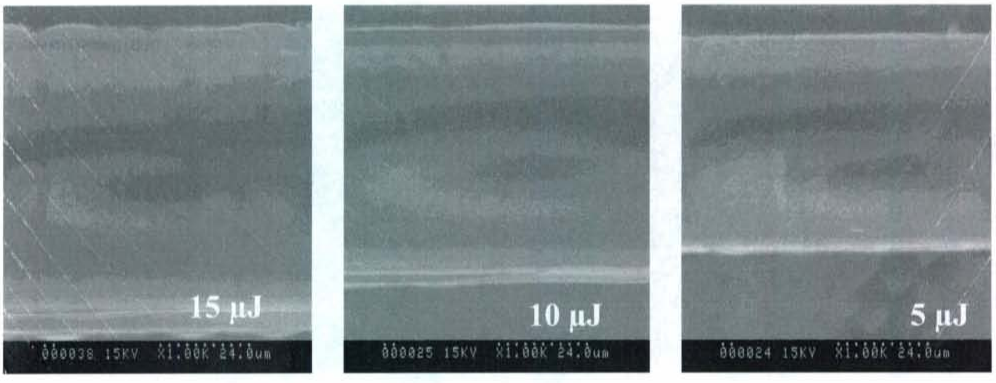

(c) (d) (e)

Figure 4-7 (a) End-face optical micrograph of microchannels; (b) SEM image of microchannels; (c), (d) and (e) SEM images of microchannels fabricated by the femtosecond laser with a pulse energy of 15, 10 and 5 μJ, respectively. The writing speed is 50 μm/s.

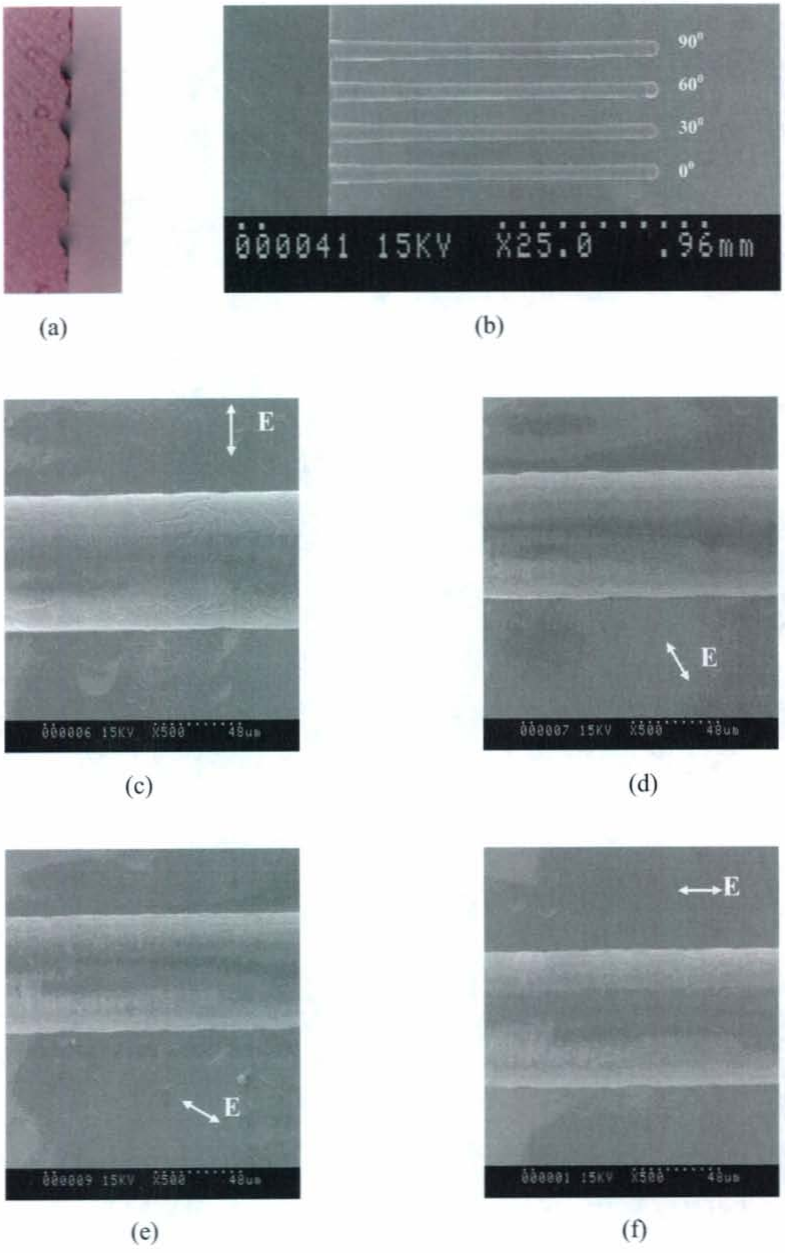

Figure 4-8 (a) End-face optical micrograph of microchannels; (b) SEM image of microchannels; (c), (d) and (e) SEM images of microchannels fabricated by the femtosecond laser with a polarization of 90°, 60°, 30° and 0°, respectively. The writing speed is 50 μm/s.

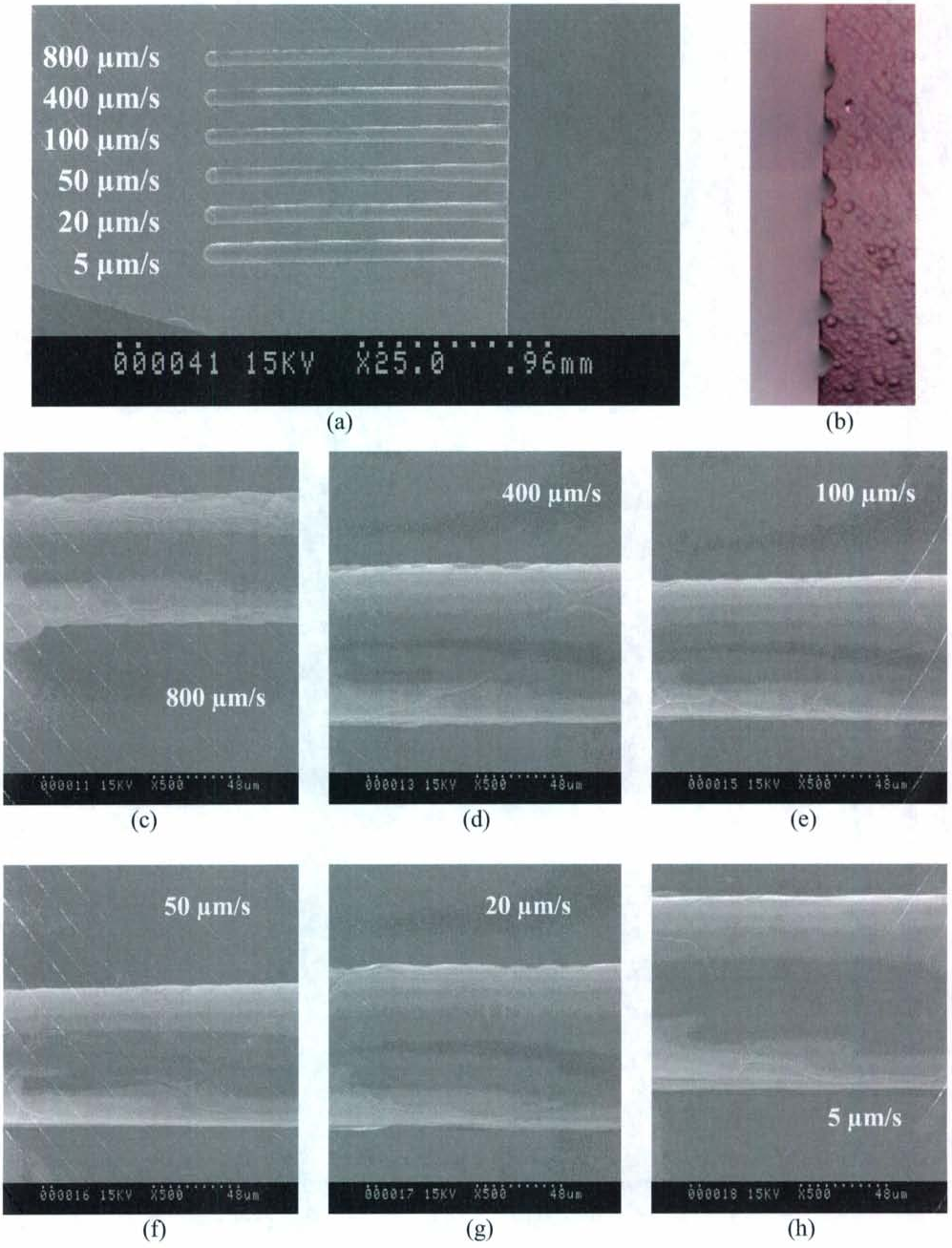

Figure 4-9 (a) SEM image of microchannels; (b) end-face optical micrograph of microchannels; (c), (d), (e), (f), (g) and (h) SEM images of microchannels fabricated at 800, 400, 100, 50 µm/s, 20 and 5 µm/s, respectively.

4.3 Intakes of a microchannel

For practical applications with a fluid passing through a microchannel for diagnostics, circular intakes are needed in order to connect a capillary tube (Upchurch Scientific, 360 μm OD and 100 μm ID) with microchannels. An intake hole with a diameter of 370-380 μm on fused silica can perfectly match the capillary tube. Although a long etching duration can achieve an intake hole of this size, the roughness of the sample surface will increase accordingly and the structure of the microchannel will be changed as well. Therefore, we propose a new technique to fabricate the intake hole, in which multiple concentric cylinders are fabricated in the sample first, followed by HF etching. The schematic illustration of multiple concentric cylinders is shown in Fig. 4-10. Each concentric cylinder consists of multiple fabricated lines which have been designed and recorded in the control program in advance. The length of the individual line depends on the depth of the desired microchannel. The separation between any two adjacent lines is ~2 μm. Figure 4-11 (a) is the concentric cylinders fabricated with the femtosecond laser at a pulse energy of 10 μJ and a writing speed of 50 μm/s. The maximum diameters of the concentric cylinders are 0, 60, 120, and 180 μm. A vertical single straight line along the Z direction is also fabricated and marked with "0". The intake holes are achieved after etching the concentric cylinders in 20% HF acid for 4 hours which are shown in Fig. 4-11 (b). The bigger the cylinder is fabricated, the larger intake hole is etched. The surface diameter of an intake hole increases about 100 μm in 4 hours. Figure 4-12 shows the structural changes of microchannels with intakes. A horizontal line with a length of 2 mm is first fabricated at a depth of 300 μm below the sample surface by a femtosecond laser

of 10 μJ and a writing speed of 50 μm/s, and then two cylinders with a diameter of 60 μm and length of 300 μm are fabricated at two sides of the line (the lower pattern in Fig. 4-12 (a)). In addition, we also fabricate a horizontal line connected to two vertical single lines (like a U shape) at the same laser parameters for comparison (the upper pattern in Fig. 4-12 (a)). After 4-hour-etching in 20% HF acid, a conical shape microchannel with a narrow neck appears on the lower pattern. The two sides of the upper pattern do not become connected because the small intake holes limit the amount of HF acid solution flowing into the microchannel for further etching (Fig. 4-12 (b)). After another 5 hours of etching, both microchannels with intakes are generated. However, the rough sample surface is observed in Fig. 4-12 (c) due to the long etching time. As a result, we conclude that the etching rate in 20% HF acid is about 25 μm/hr. 5.5 hours is the proper etching duration to achieve an intake hole of 370 - 380 μm in diameter, in which the diameters of the individual concentric cylinders are 0, 80, 160, and 240 μm, respectively. Figure 4-13 presents the side-view of an intake hole connected to a capillary tube, which clearly shows a perfect match between the intake hole and the capillary tube.

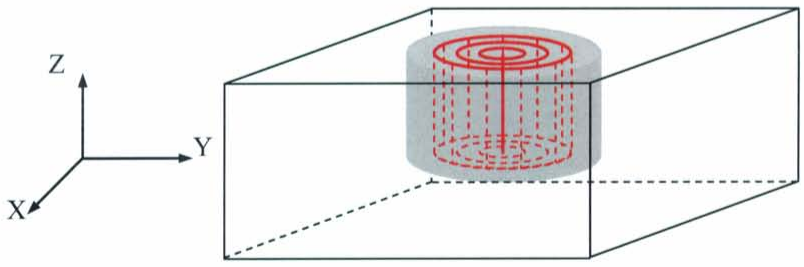

Figure 4-10 Schematic illustration for the fabrication of an intake hole. The red dashed lines are fabricated tracks of a femtosecond laser. The separation between any two adjacent lines is ~2 μm. The grey cylinder is the final intake hole after HF etching.

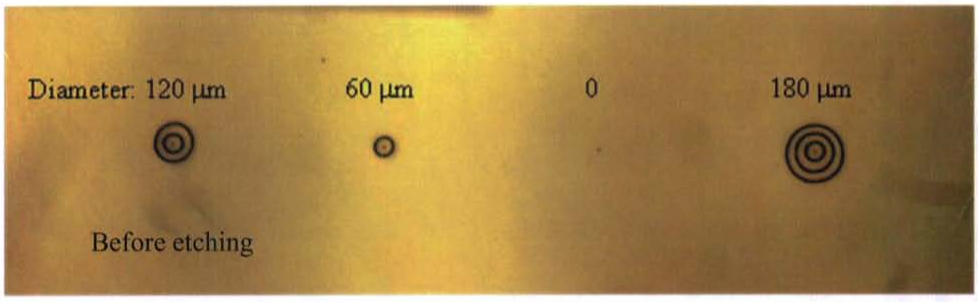

(a)

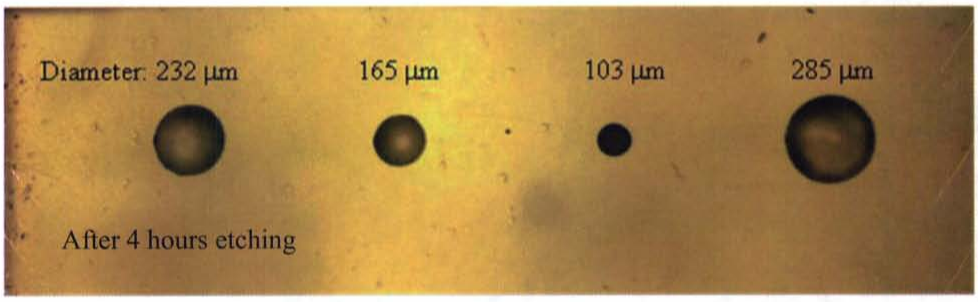

(b)

Figure 4-11 Intake holes before and after HF etching: (a) fabricated concentric cylinders with the femtosecond laser at a pulse energy of 10 μJ and a writing speed of 50 μm/s. A vertical single line is fabricated and marked with "0"; (b) intake holes achieved after etching the concentric cylinders in 20% HF acid for 4 hours.

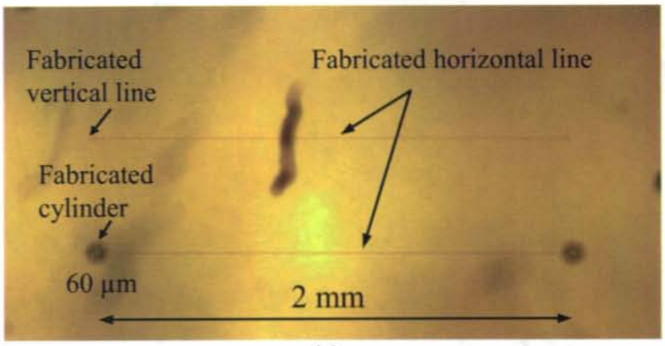

(a)

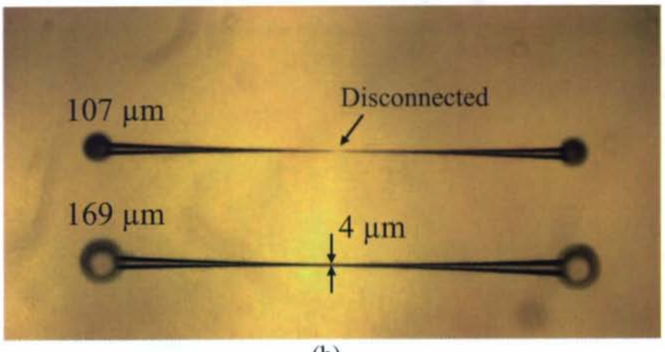

(b)

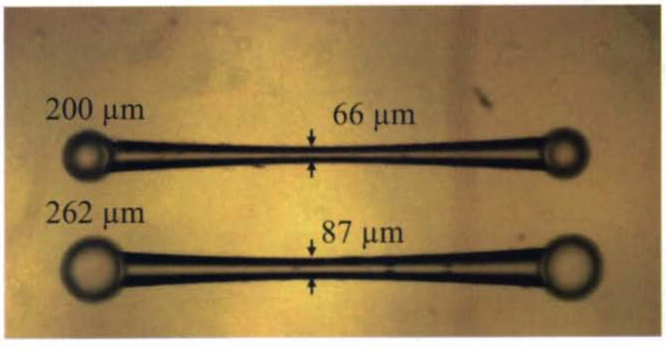

(c)

Figure 4-12 Microchannel with intakes before and after HF etching: (a) two patterns fabricated by a femtosecond laser of 10 μJ and a writing speed of 50 μm/s; (b) microchanhnels etched by 20% HF acid for 4 hours; (c) microchannels etched by 20% HF acid for 9 hours.

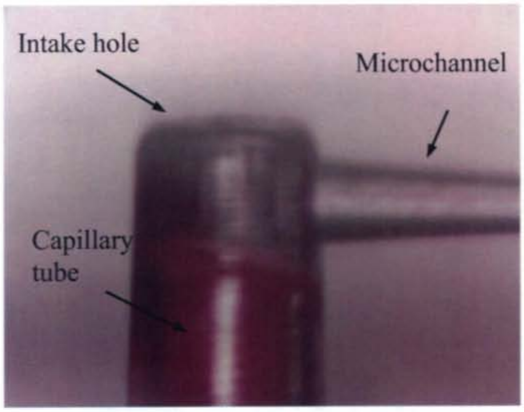

Figure 4-13 Optical micrograph of the side-view of an intake hole with a capillary tube. The red part is the capillary tube.

4.4 Shape-controlled microchannels

The common shape of a microchannel is cone-like due to the fact of more etching time experienced at the entrance. As mentioned in the previous chapter, the cross section of a microchannel is an ellipse. In many applications, a circular cross-sectioned microchannel or cylindrical microchannel is preferred. In this section, we report our development of compensation techniques for microchannel fabrication.

4.4.1 Conical microchannels

The difference between the transverse and conjugate diameter of the cross section of a microchannel fabricated by the femtosecond laser of 10 μJ pulse energy is about 30 μm which is observed from the sample side. Therefore, we fabricate a triangle with a base side of 30 μm in length. The maximum separation between two adjacent lines is ~2 μm. The schematic illustration of our cross section compensation fabrication technique is

shown in Fig. 4-14. Figure 4-15 shows the structural changes of microchannels fabricated by a common (single line) and compensation fabrication techniques. The shape of the cross section of the microchannel becomes circular after compensation fabrication. Another important character of this compensation fabrication is that the length of the microchannel significantly increases because a microchannel of larger cross section hosts a larger amount of HF acid to enter the sample interior, thus further etching the material.

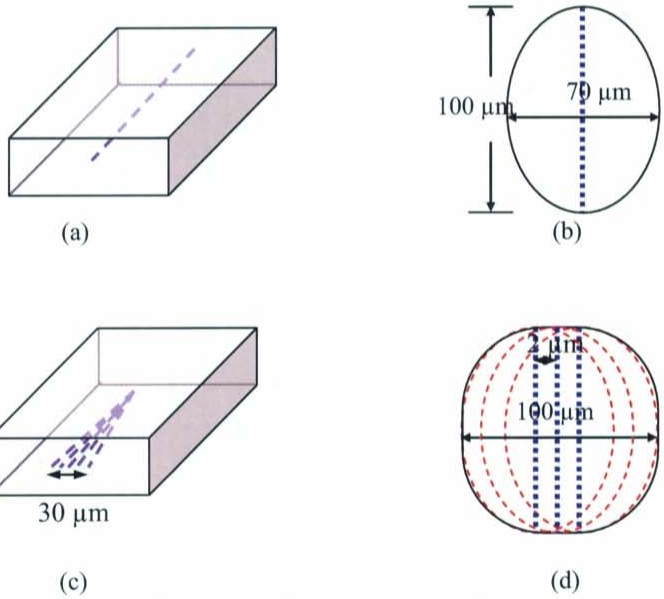

Figure 4-14 Schematic illustration of a compensation fabrication: (a) single line fabrication; (b) cross section of the single line after etching; (c) triangle compensation fabrication with 2 μm separation; (d) cross section of compensation fabrication. The blue dashed line shows the fabricated track, and the red dashed line is the cross section of a commonly fabricated microchannel.

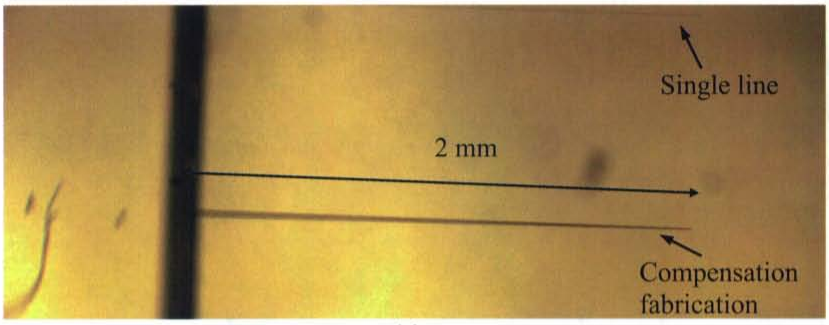

(a)

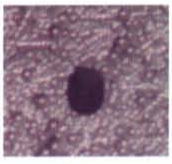

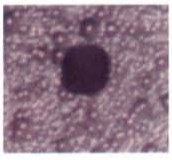

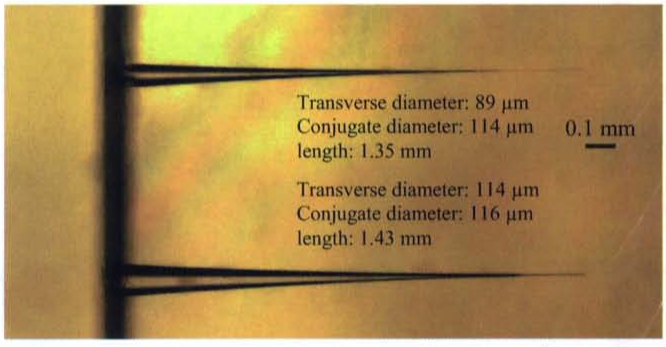

(b) (c)

Figure 4-15 Comparison of elliptical and conical microchannel fabrication: (a) microchannels fabricated by the femtosecond laser at a pulse energy of 10 μJ and a writing speed of 50 μm/s before etching; (b) and (c) end-view (left) and side-view (right) of the microchannels after etching for 4 hours in 20% HF acid solution.

4.4.2 Cylindrical microchannels

A similar compensation fabrication technique is also used to produce a cylindrical microchannel (elliptic cylinder). A schematic illustration of cylindrical microchannel compensation fabrication is shown in Fig. 4-16. Compensating lines are fabricated toward the opposite direction of a common microchannel. The maximum separation between any two adjacent lines is ~ 2 μm. After HF etching, a cylindrical microchannel appears.

Figure 4-17 presents the microchannels produced by a compensation fabrication method.

The first one is a conical microchannel, and the second one is a cylindrical microchannel.

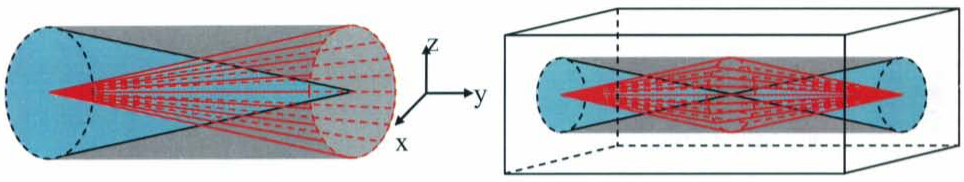

(a) (b)

Figure 4-16 (a) Schematic illustration of cylindrical microchannel fabrication; (b) schematic illustration of a long cylindrical microchannel in the bulk of a sample. The blue one is the common conical microchannel. The red ones are extra compensation fabrication lines to compensate for the conical microchannel. The grey one is the final cylindrical microchannel.

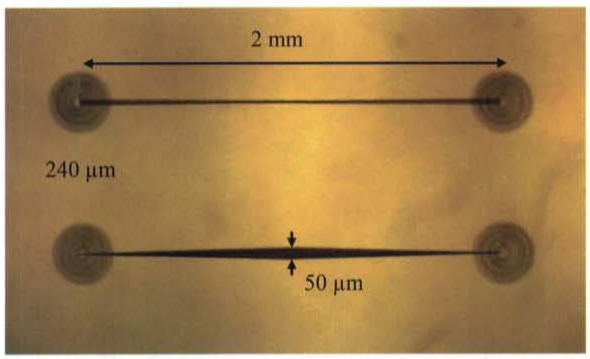

(a)

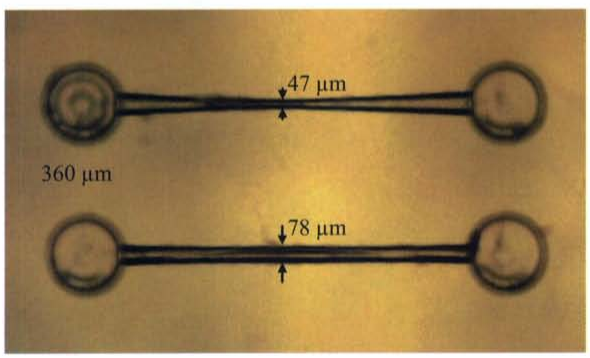

(b)

Figure 4-17 Fabrication of microchannels by compensation fabrication technique: (a) microchannels fabricated by a femtosecond laser at a pulse energy of 10 μJ and a writing speed of 50 μm/s before etching; (b) microchannels after etching for 5 hours in 20% HF acid solution.

4.5 Various microchannels

Combining the technique of fabricating a conical microchannel and a cylindrical microchannel, various microchannels have been made. Figures 4-18 ~4-23 show several microchannels of different shapes. Since these microchannels are etched in different batches of experiments, slight discrepancies in the widths of the microchannels and the diameters of the intake holes exist even with the same etching parameters.

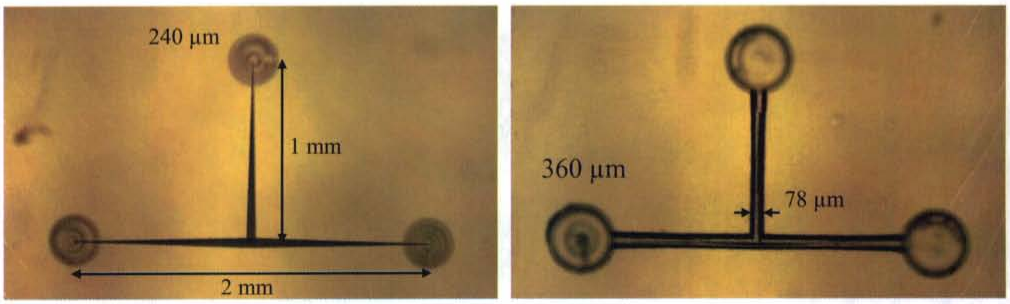

(a) (b)

Figure 4-18 Intakes attached T-shaped microchannel: (a) femtosecond laser microfabricated microchannel before etching; (b) microchannel after etching for 5 hours in 20% HF acid solution.

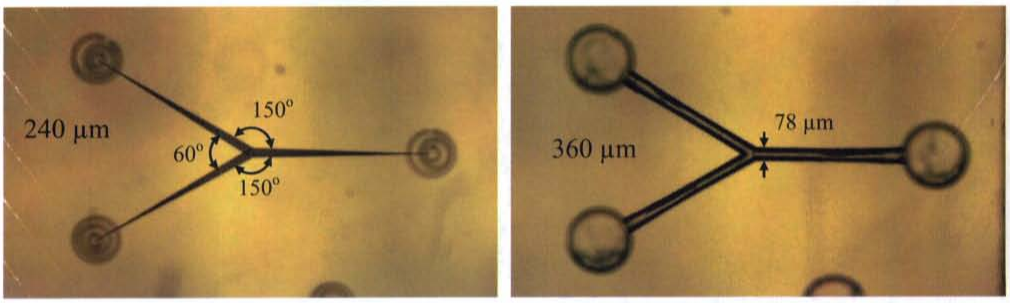

(a) (b)

Figure 4-19 Intakes attached Y-shaped microchannel: (a) femtosecond laser microfabricated microchannel before etching; (b) microchannel after etching for 5 hours in 20% HF acid solution.

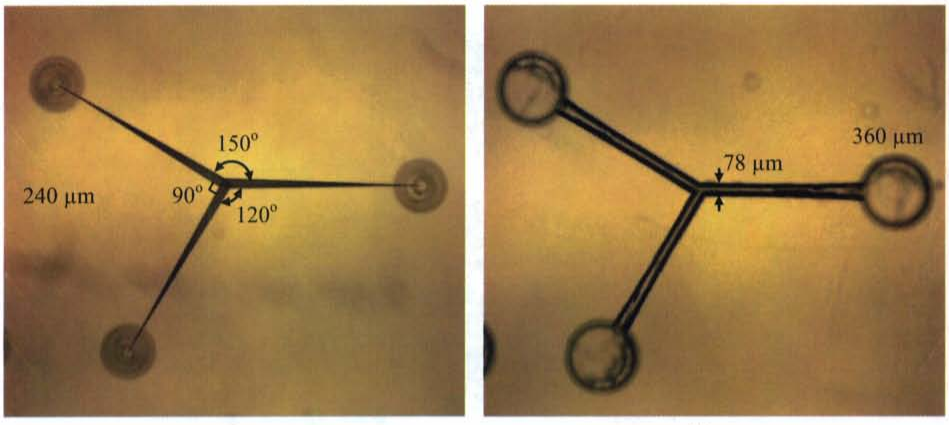

(a) (b)

Figure 4-20 Intakes attached Y-shaped microchannel: (a) femtosecond laser microfabricated microchannel before etching; (b) microchannel after etching for 5 hours in 20% HF acid solution.

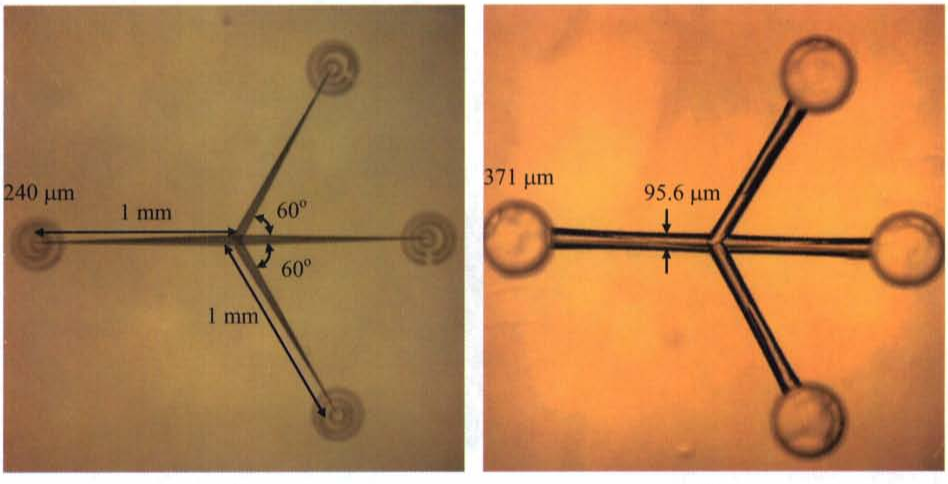

(a) (b)

Figure 4-21 Branched microchannel with three intakes: (a) femtosecond laser microfabricated microchannel before etching; (b) microchannel after etching for 5.5 hours in 20% HF acid solution.

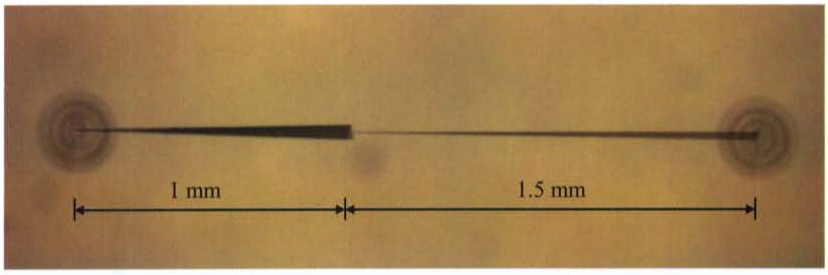

(a)

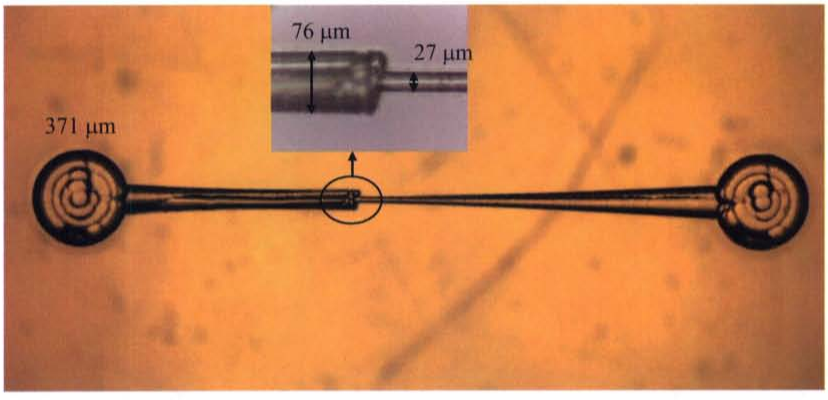

(b)

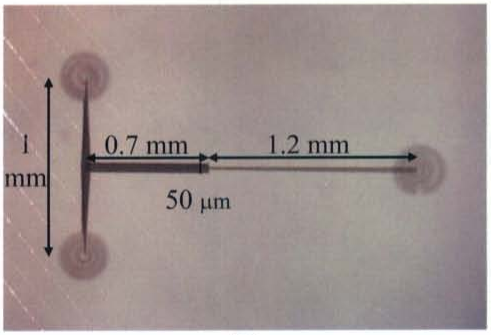

(c)

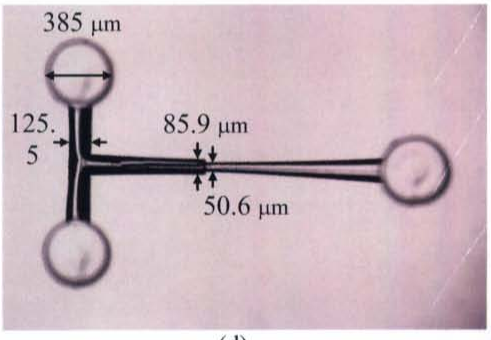

(d)

Figure 4-22 Intakes attached to a microchannel with varying diameters: (a) and (c) femtosecond laser microfabricated microchannel before etching; (b) and (d) microchannel after etching for 5.5 hours in 20% HF acid solution.

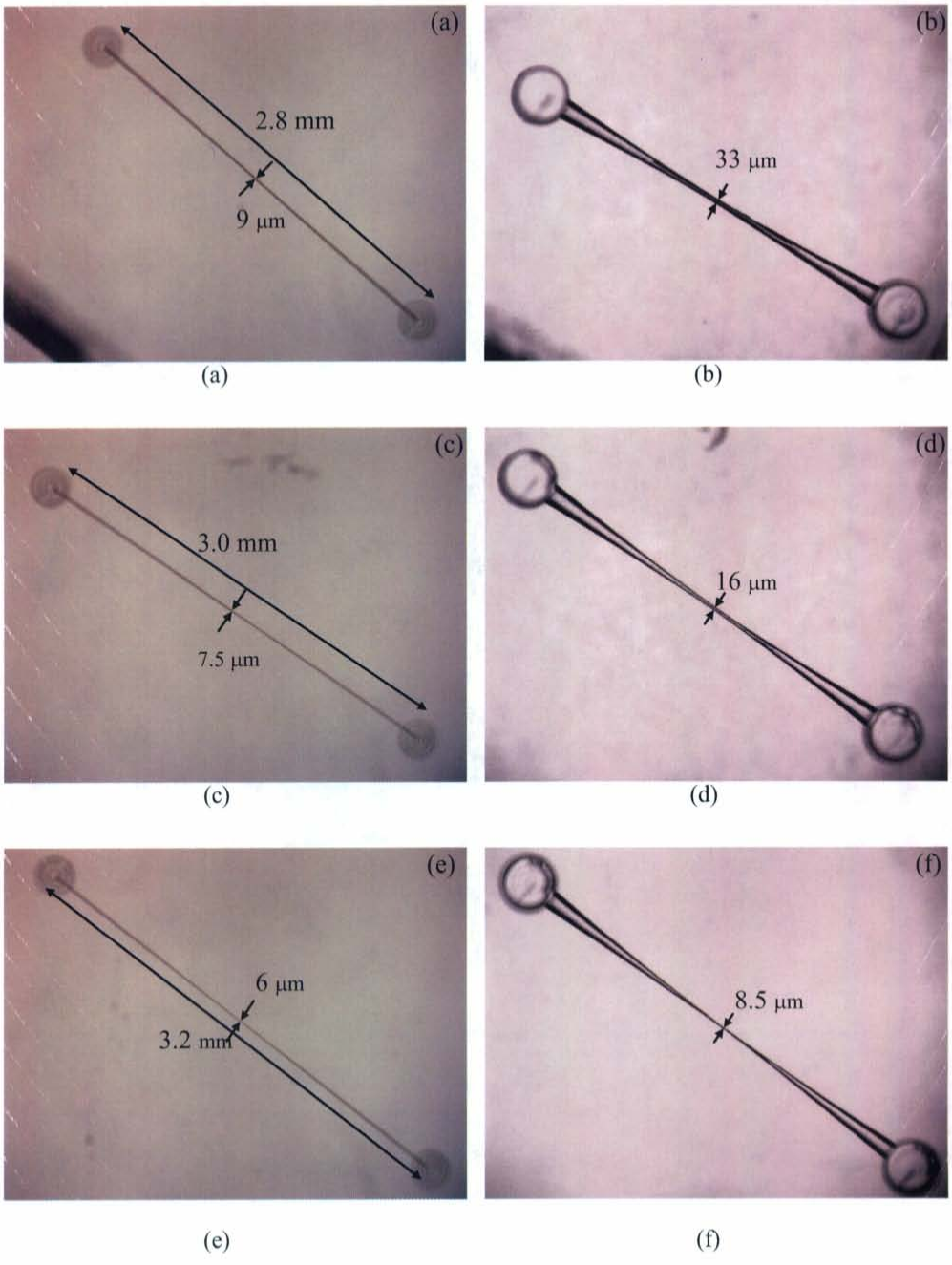

Figure 4-23 Intakes attached to a microchannel with varying diameters: (a), (c) and (e) femtosecond laser microfabricated microchannels before HF etching; (b), (d) and (f) microchannels after 20% HF etching for 5.5 hours.

Chapter 5 Laminar flow in the microchannel

5.1 Introduction

The flow mechanism on a microscale is completely different from that on a macroscale. On a microscale, laminar flow is the main flow mechanism due to a very low Reynolds number (the ratio of inertial forces to viscous forces) [230, 231]. Particles in the fluid move in an orderly way in straight lines along the pipe walls without eddies or swirls of fluids. Particle transportation between lines takes place only through diffusion. The diffusion equation in laminar flow fluids is given by [232]

$$C(t,x)=\frac{1}{2}C_0\sum_{n=-\infty}^{\infty}(erf\frac{h+2nl-x}{2\sqrt{Dt}}+erf\frac{h-2nl+x}{2\sqrt{Dt}}) \tag{5.1}$$

where $C(t,x)$ is the concentration at time t and at point x, D is the diffusion coefficient in cm^2/s, t is the time in seconds, l is the width of the channel, h is the fluid width of the initial distribution and C_0 is the initial concentration of fluid in the channel.

Laminar flow has many applications in micro-optofluidics. T-shaped opto-microfluidic devices are widely applied in measuring the diffusion coefficient of an analyte [233, 234], analyte concentration [235], and reaction kinetics [236-238] by detecting the laminar diffusion in the microchannel. Particle filter through laminar flow was reported. Particles have different diffusion coefficients depending on their sizes. When a sample is infused into a H-shaped mirochannnel, small particles diffuse longer distances than large particles do over the same duration through laminar flow and large particles are filtered without membranes [239, 240]. Cho *et al.* proposed a new technique to separate motile sperm by laminar flow. When the sperm sample and media are injected

into an H-shaped microchannel, the non-motile sperm flows along one channel through laminar flow, but the motile sperm disperses and swims to the other channel with a faster velocity [241].

In this section, in order to understand the flow mechanisms in microchannels for further opto-microfluidic experiments, fluorescein isothiocynate isomer I (FITC, Sigma-aldrich®, λ_{ex} 492 nm; λ_{em} 518 nm) in an aqueous solution ($D = 5\times10^{-6}$ cm^2/s) and distilled water are used to study the laminar flow. In addition, simulations of laminar flow are carried out with MATLAB software to compare with the experimental results. In the simulation, we first calculate the flow time (diffusion time) t from the fluid convergent location to various points in the microchannel, and then the fluid concentrations at various points are obtained by designating corresponding x and t values into Equation 5.1. A numerical evaluation uses the first 21 terms in the sum (n = -10 to +10) [242].

5.2 Assembly of the opto-microfluidic device and system

In order to have a functional opto-microfluidic system for the fluidic diagnostic, assembly of opto-microfluidic components is a necessary step. In our study, a microchannelled chip is first cleaned in an ultrasonic bath for 15 minutes, then dried and attached to a microscope slide. A capillary tube of 15 cm in length is tightly inserted into an intake hole, and sealed with superglue. The other side of the tube for liquid input is inserted and glued in a syringe needle (Gauge 22). A syringe (BD®) of 1 mL in volume is then connected to a syringe pump (Chemyx®, Fusion 400) to form an opto-microfluidic system. Figure 5-1 shows the procedures to assemble an opto-microfluidic system. In this

process, tube sleeves (the green ones in Fig. 5-1 (b)) are used to improve the durability by increasing the glue area.

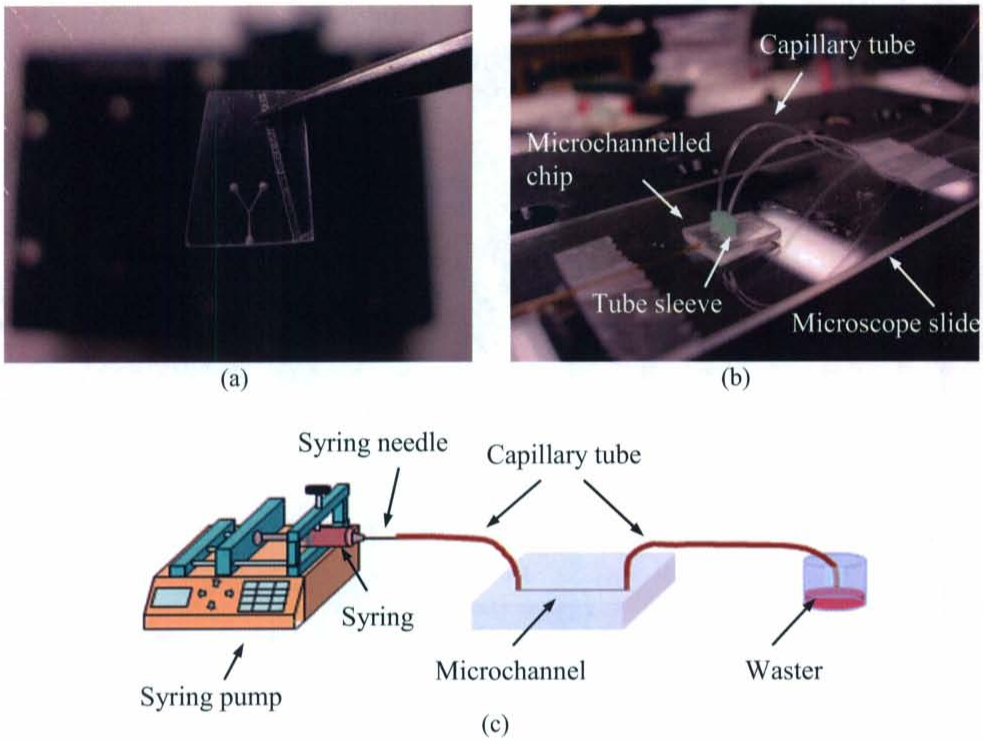

Figure 5-1 Procedures for the assembly of an opto-microfluidic device and system: (a) cleaning of a microchannelled chip; (b) attachment of capillary tubes onto the chip; (c) schematic illustration of connection with a syringe pump.

5.3 Laminar flow in a Y-shaped microfluidic device

In the Y-shaped opto-microfluidic system, FITC and distilled water are infused into the intake holes by the syringe pump with the same pump speed (Fig. 5-1). An Epifluorescence microscope (Eclipse E600) is used to observe the flow of FITC in the microchannel (Fig. 5-2). Laminar flow and diffusion are investigated in the cone-shaped microchannel with an objective lens of magnified 10×. Figures 5-3~5-6 show the laminar

flow with decreasing flow rates (10.0, 1.0, 0.1, and 0.01 μL/min, respectively). In the higher flow rate case, the diffusion is weak, which can only be observed from the middle layer of the fluids. The diffusion is significant in the low flow rate due to the fact that a long flow time (diffusion time) t spent in the microchannel. The simulation results of laminar flow in this cone-shaped microchannel are shown below the fluorescence images. In the simulation, the diameters of the cone-shaped microchannel are 64 μm and 124 μm, and the length of the microchannel is 1232 μm. All data match the sizes of the real microchannel. The yellow colour shows the FITC fluid, while the black colour represents the distilled water, and the colours between black and yellow shown in the colour bar show the different concentrations of fluid. The experimental and simulation data perfectly match in high flow rates, but a slight discrepancy is exhibited in the initial flow at low flow rates. The main reason is that we consider the structure of the microchannel at the fluid convergent location as a cone in the simulation model, which is different from the real structure. In addition, the temperature and the roughness of a microchannel also have an impact on the fluid diffusion.

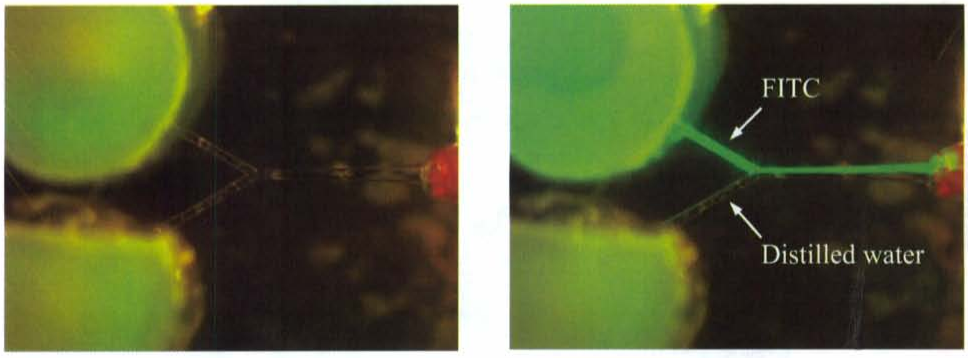

(a) (b)

Figure 5-2 A Y-shaped opto-microfluidic device: (a) channel filled with distilled water; (b) channel filled with distilled water and fluorescein isothiocyanate isomer I (FITC).

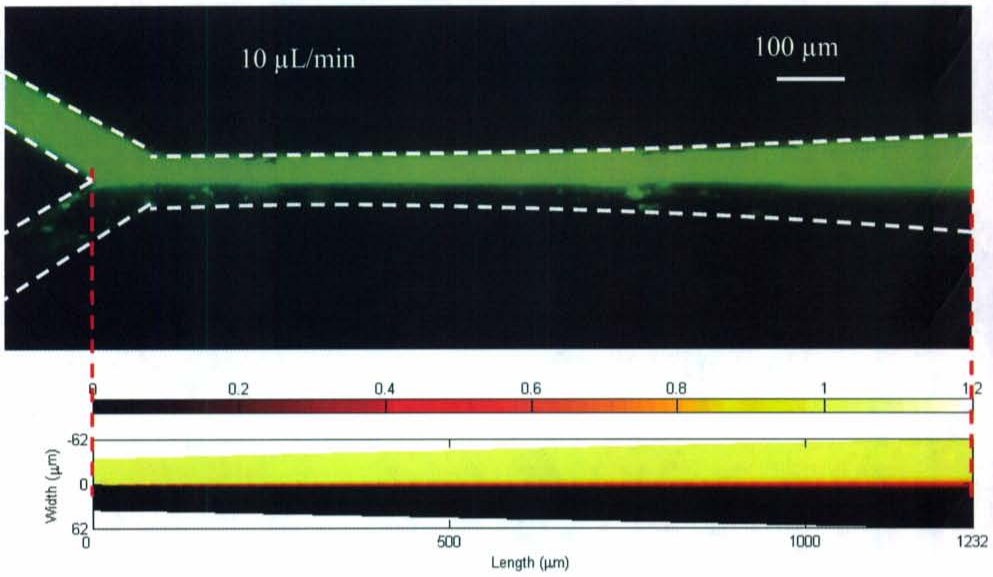

Figure 5-3 Flow of fluids in a Y-shaped microchannel with 10 µL/min flow rates. The colour images are the simulations of the laminar flow and diffusion. The white dashed lines show the edges of the microchannel.

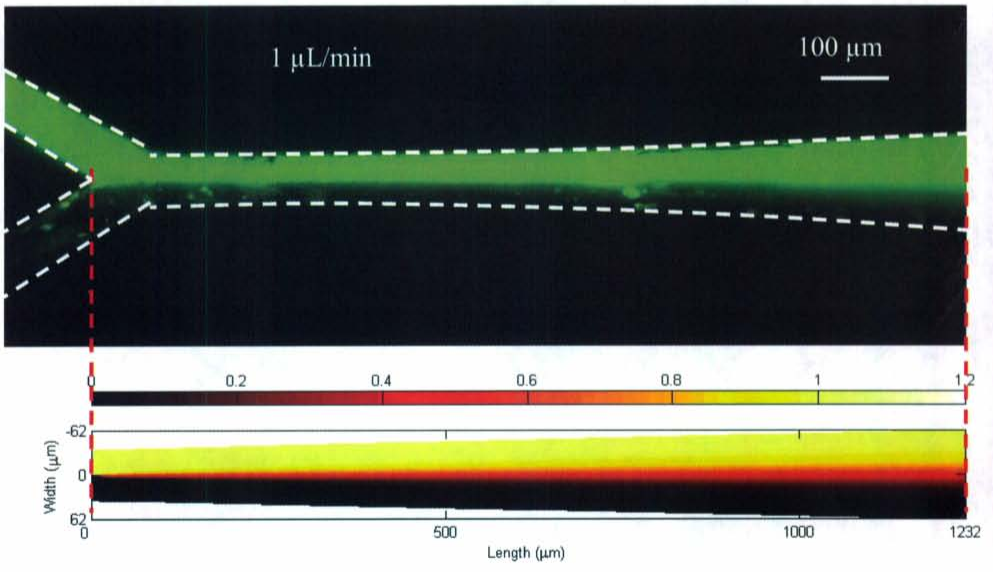

Figure 5-4 Flow of fluids in a Y-shaped microchannel with 1µL/min flow rates. The colour images are the simulations of the laminar flow and diffusion. The white dashed lines show the edges of the microchannel.

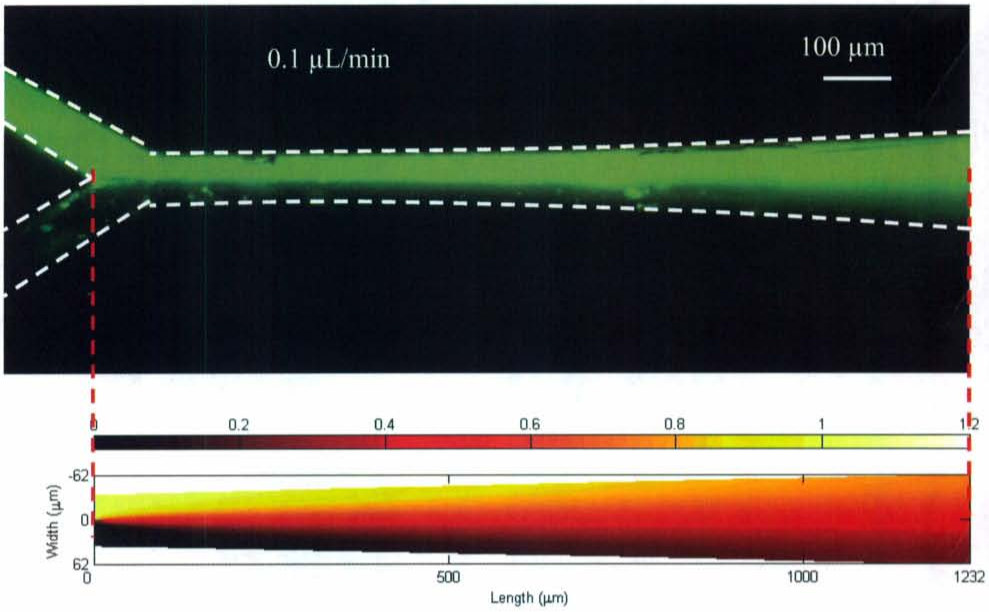

Figure 5-5 Flow of fluids in a Y-shaped microchannel with 0.1μL/min flow rates. The colour images are the simulations of the laminar flow and diffusion. The white dashed lines show the edges of the microchannel.

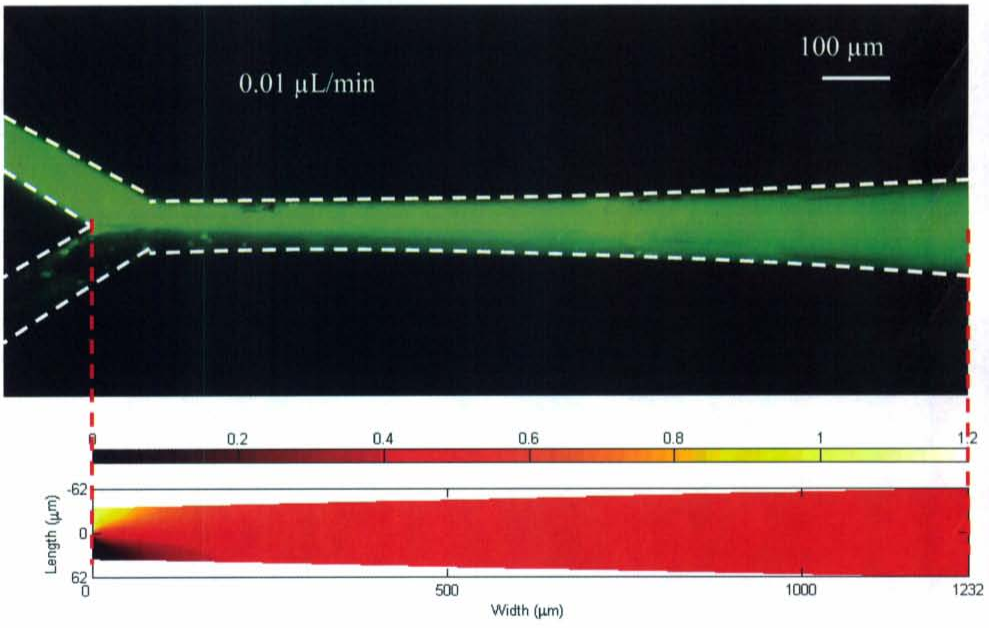

Figure 5-6 Flow of fluids in a Y-shaped microchannel with 0.01μL/min flow rates. The colour images are the simulations of the laminar flow and diffusion. The white dashed lines show the edges of the microchannel.

5.4 Laminar flow in an opto-microfluidic device with three intakes

In order to study laminar flow and diffusion of two or three fluids within one channel, opto-microfluidic devices consisting of a microchannel with three intakes is assembled, as shown in Fig. 5-7. The shape of the microchannel in the fabricated device is a cylinder with a diameter of 114 μm and a length of 670 μm. Laminar flow and diffusion with different flow rates are investigated and simulated for different configurations. In the followed simulated images, the red colour simulates the FITC fluid, the blue colour simulates the distilled water, and the colours between blue and red shown in the colour bar represent the different concentrations of fluid. For a better comparison between the experimental and simulation results, the fluorescent image is converted into pseudocolour image using MATLAB.

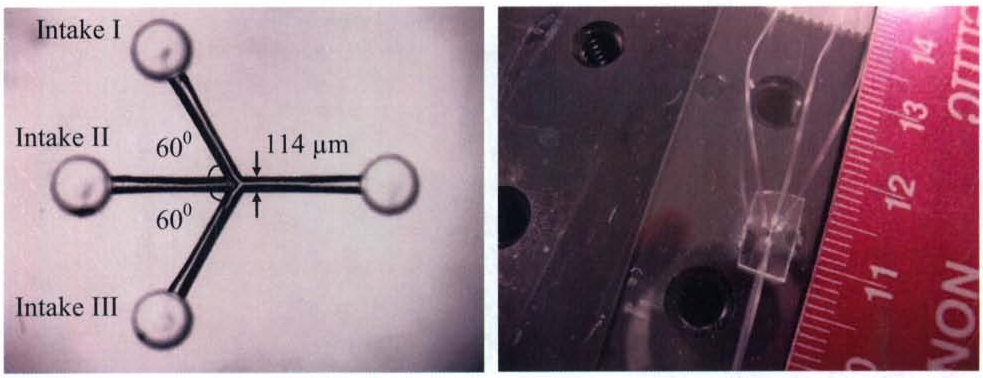

(a) (b)

Figure 5-7 Opto-microfluidic device with four-intakes: (a) opto-microfluidic channel with three-intakes; (b) opto-microfluidic devices with four-intakes assembled with capillary tubes.

Table 5-1 lists three groups of laminar flow and diffusion experiments in different configurations. Figures 5-8~5-19 show that laminar flow takes place in the microchannel

no matter how many different kinds of fluid and what flow rates of the fluids are pumped into the microchannel. No eddies and swirls are observed from the fluorescence microscope images and the diffusion is more significant at the point with the longer diffusion time, such as the end of the microchannel in the high flow rate and the whole microchannel in the low flow rate. Fluid with uniform concentration appears at the position of about 200 μm from the fluid convergent point due to the perfect diffusion at the flow rate of 0.01 μm/min. These experimental results are in good agreement with the laminar flow and diffusion simulation results. In addition, when three kinds of fluid are injected into the microchannel with the same pump rate, the fluid widths of the initial distribution are 42, 30, and 42 μm by simulation with Mathematics software, assuming the cross section of the microchannel to be either a circle or an ellipse (Fig. 5-20). The experimental results show the three fluid widths of the initial distribution are 43, 28, and 43 μm, which also coincide with the simulation result.

Table 5-1 List of laminar flow experiments in an opto-microfluidic device with three intakes.

Configuration label	Description	Flow rate (μL/min)	Figure
A	Intakes I and III filled with distilled water, intake II filled with FITC	10	Fig. 5-5
		1	Fig. 5-6
		0.1	Fig. 5-7
		0.01	Fig. 5-8
B	Intakes II and III filled with distilled water, intake I filled with FITC	10	Fig. 5-9
		1	Fig. 5-10
		0.1	Fig. 5-11
		0.01	Fig. 5-12
C	Intakes I and III filled with FITC, intake II filled with distilled water	10	Fig. 5-13
		1	Fig. 5-14
		0.1	Fig. 5-15
		0.01	Fig. 5-16

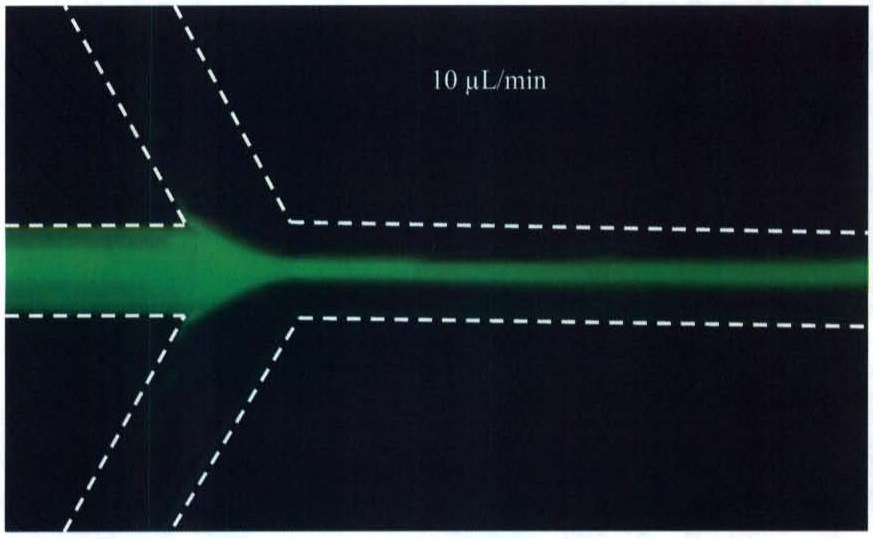

(a)

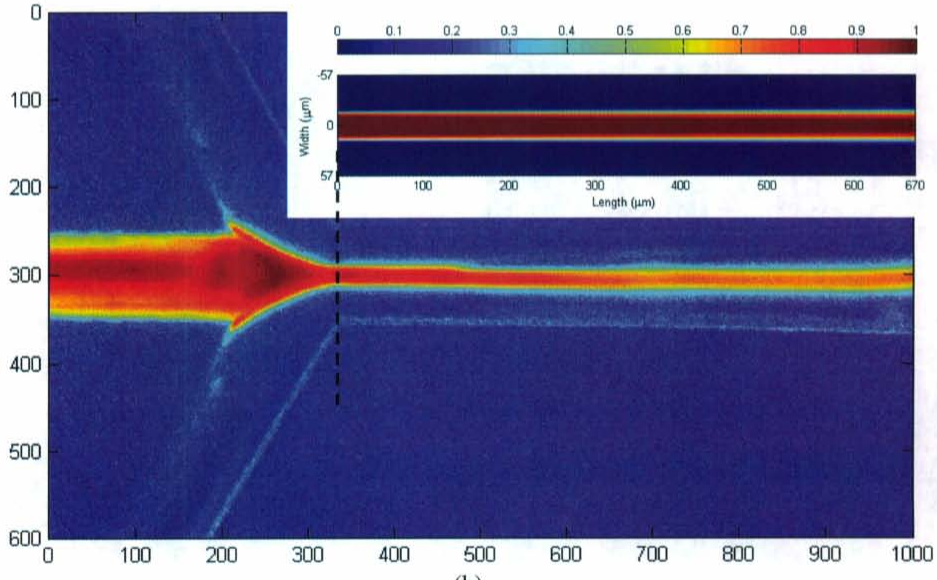

(b)

Figure 5-8 Flow of fluids in the microchannel of configuration A with a flow rate of 10 μL/min: (a) the fluorescence image of the microchannel observed by fluorescence microscopy; (b) pseudocolour image of (a). The inset is the simulation results. The white dashed lines show the edges of the microchannel.

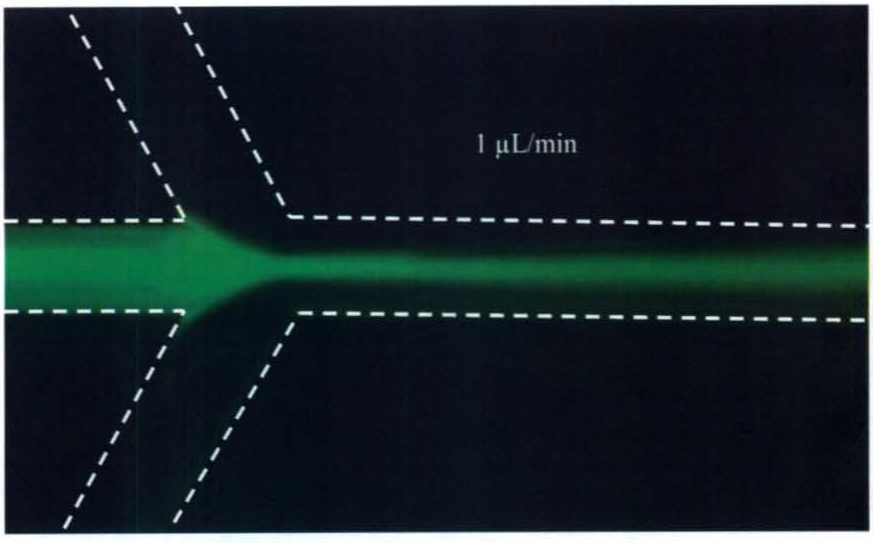

(a)

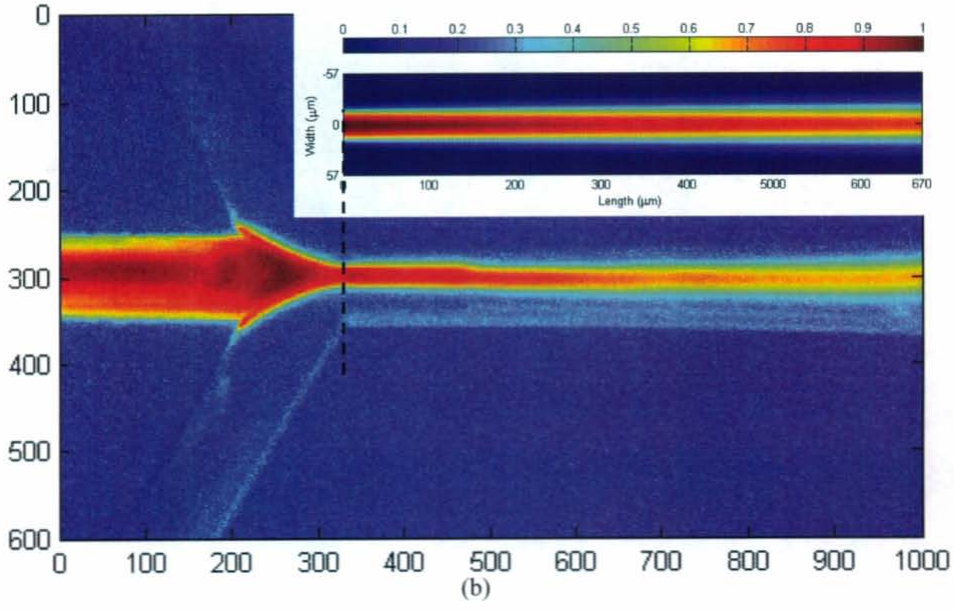

(b)

Figure 5-9 Flow of fluids in the microchannel of configuration A with a flow rate of 1 μL/min: (a) the fluorescence image of the microchannel observed by fluorescence microscopy; (b) pseudocolour image of (a). The inset is the simulation results. The white dashed lines show the edges of the microchannel.

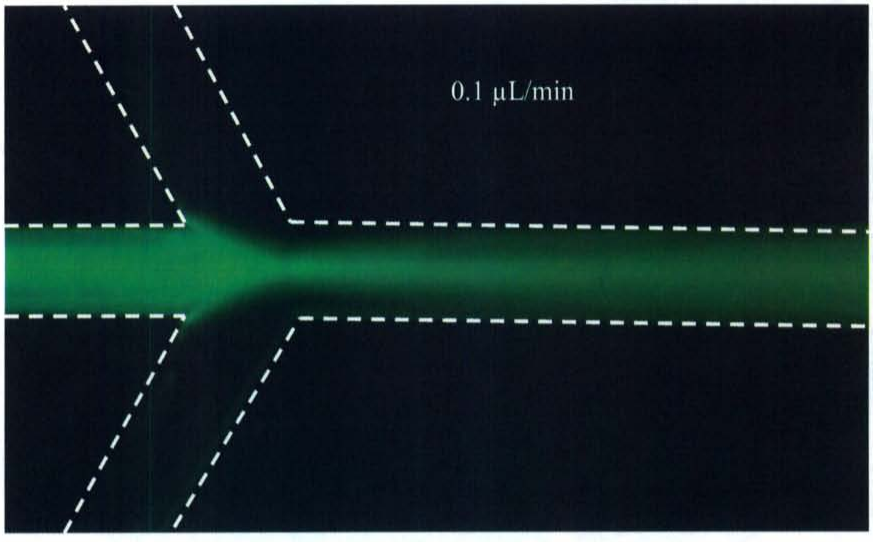

(a)

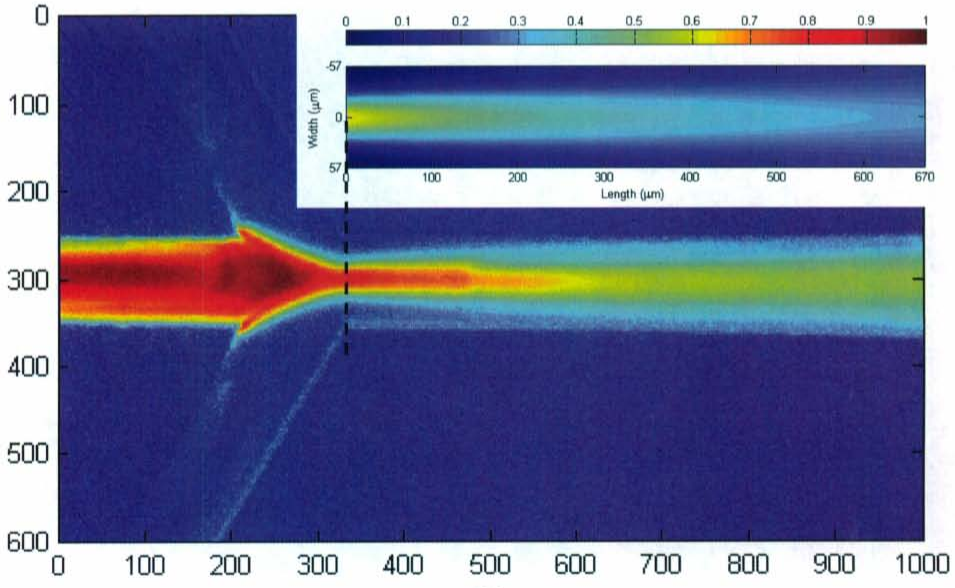

(b)

Figure 5-10 Flow of fluids in the microchannel of configuration A with a flow rate of 0.1 μL/min: (a) the fluorescence image of the microchannel observed by fluorescence microscopy; (b) pseudocolour image of (a). The inset is the simulation results. The white dashed lines show the edges of the microchannel.

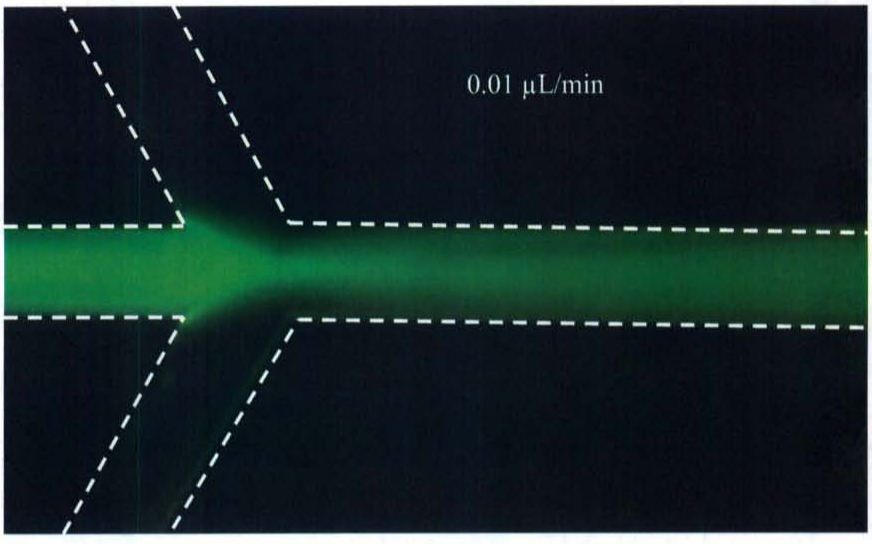

(a)

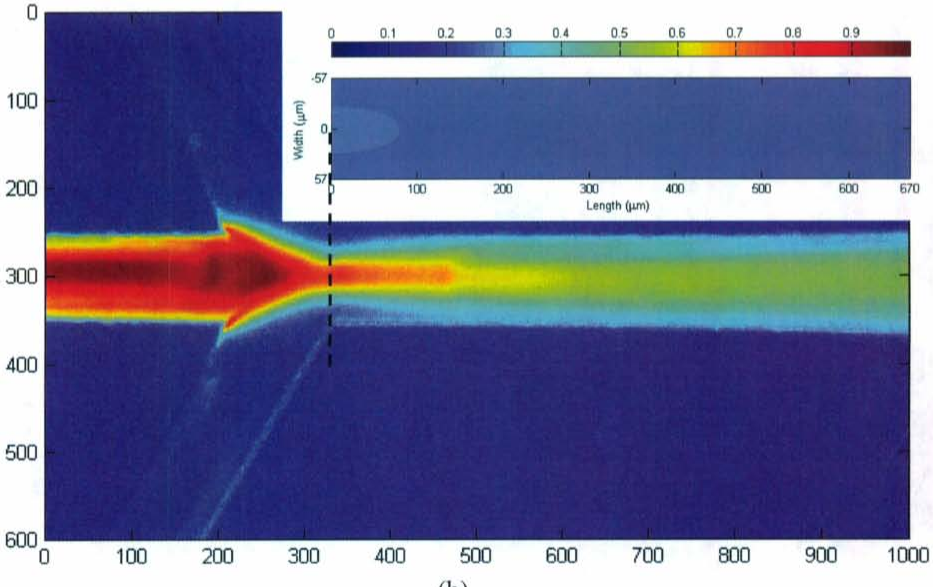

(b)

Figure 5-11 Flow of fluids in the microchannel of configuration A with a flow rate of 0.01 μL/min: (a) the fluorescence image of the microchannel observed by fluorescence microscopy; (b) pseudocolour image of (a). The inset is the simulation results. The white dashed lines show the edges of the microchannel.

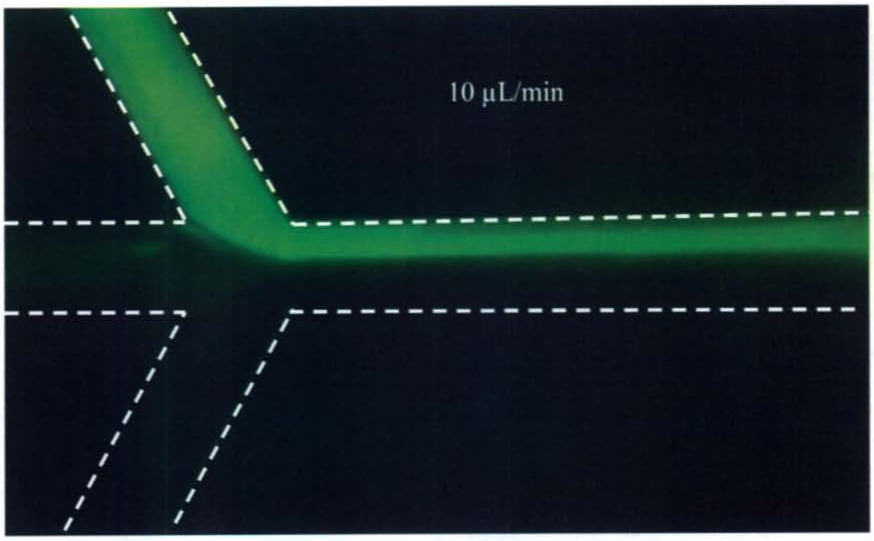

(a)

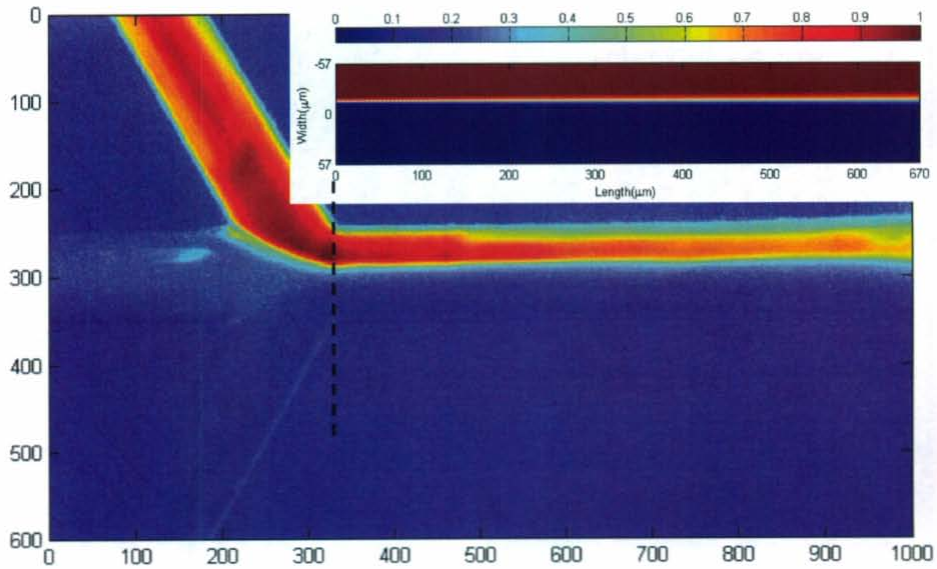

(b)

Figure 5-12 Flow of fluids in the microchannel of configuration B with a flow rate of 10 μL/min: (a) the fluorescence image of the microchannel observed by fluorescence microscopy; (b) pseudocolour image of (a). The inset is the simulation results. The white dashed lines show the edges of the microchannel.

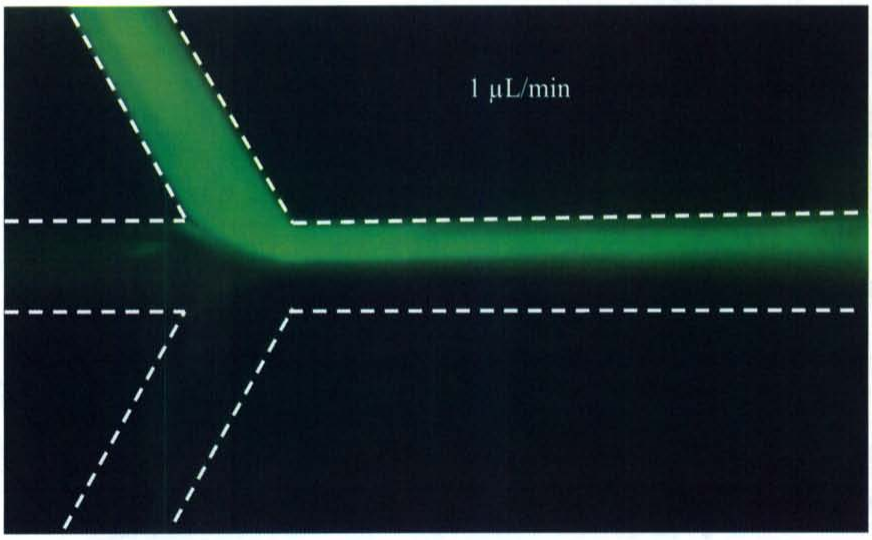

(a)

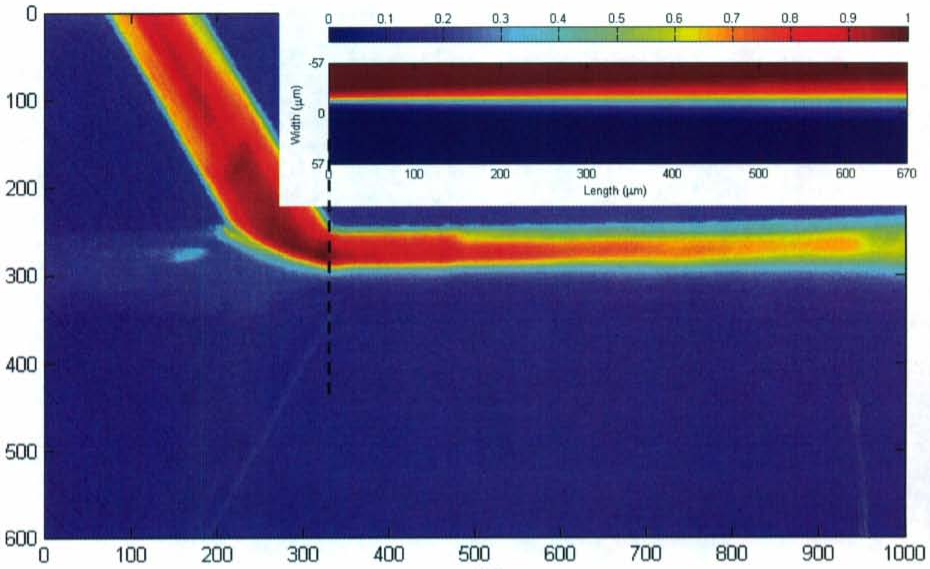

(b)

Figure 5-13 Flow of fluids in the microchannel of configuration B with a flow rate of 1 μL/min: (a) the fluorescence image of the microchannel observed by fluorescence microscopy; (b) pseudocolour image of (a). The inset is the simulation results. The white dashed lines show the edges of the microchannel.

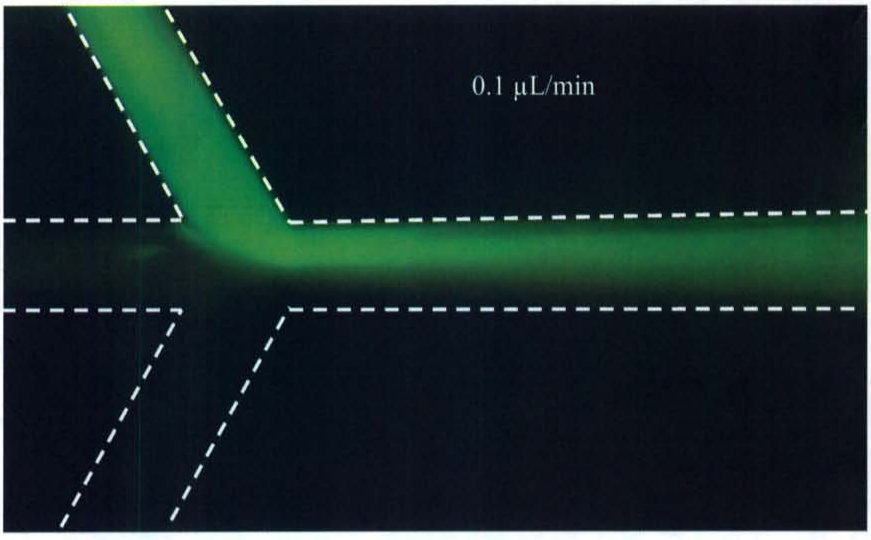

(a)

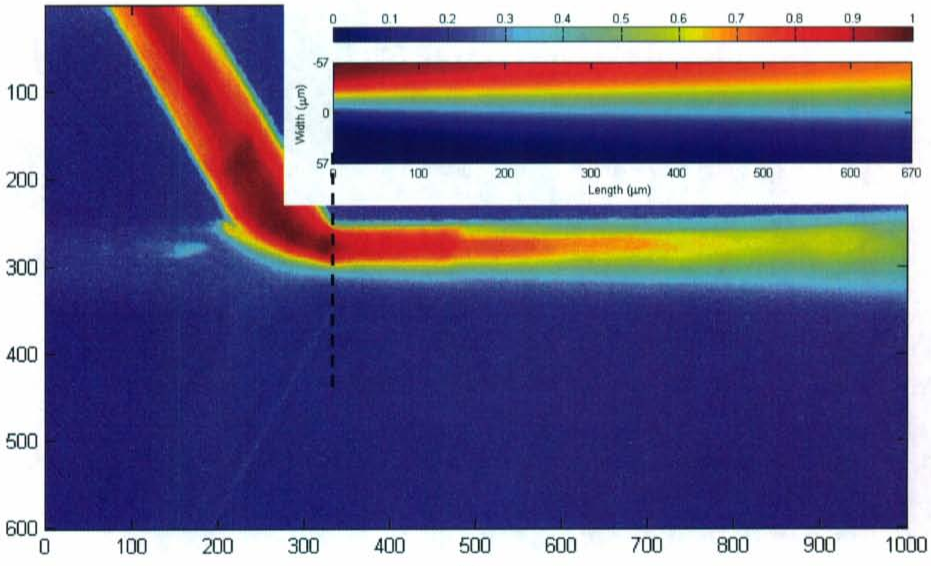

(b)

Figure 5-14 Flow of fluids in the microchannel of configuration B with a flow rate of 0.1 μL/min: (a) the fluorescence image of the microchannel observed by fluorescence microscopy; (b) pseudocolour image of (a). The inset is the simulation results. The white dashed lines show the edges of the microchannel.

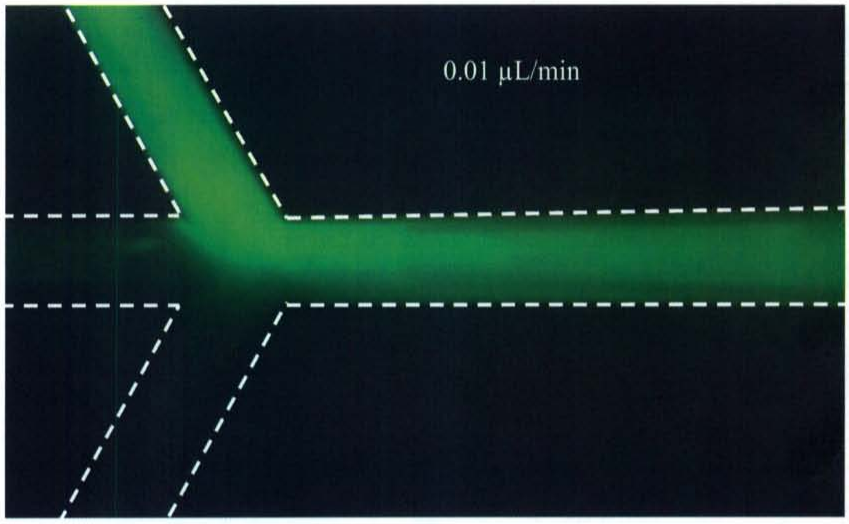

(a)

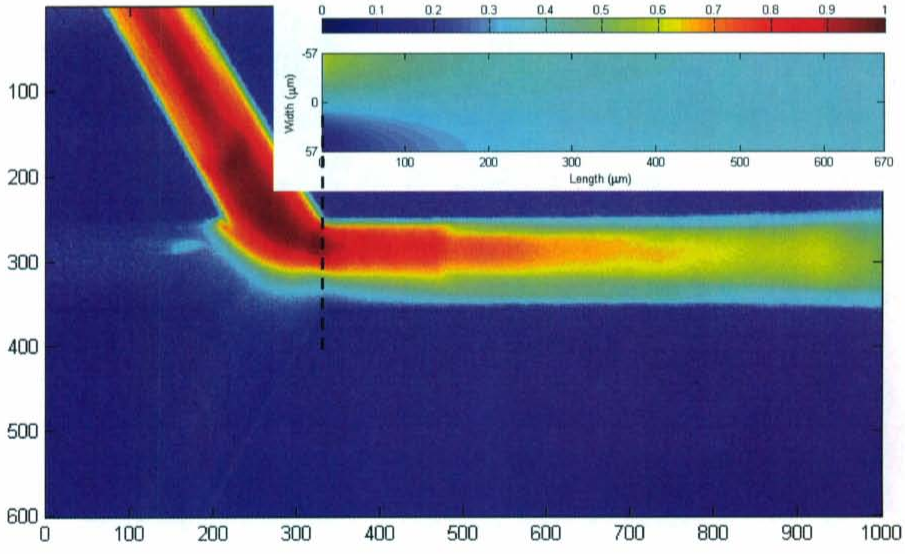

(b)

Figure 5-15 Flow of fluids in the microchannel of configuration B with a flow rate of 0.01 μL/min: (a) the fluorescence image of the microchannel observed by fluorescence microscopy; (b) pseudocolour image of (a). The inset is the simulation results. The white dashed lines show the edges of the microchannel.

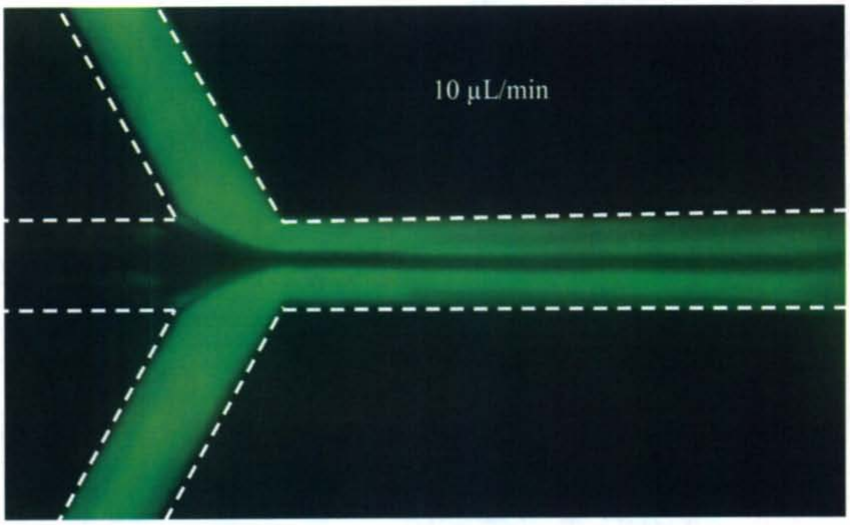

(a)

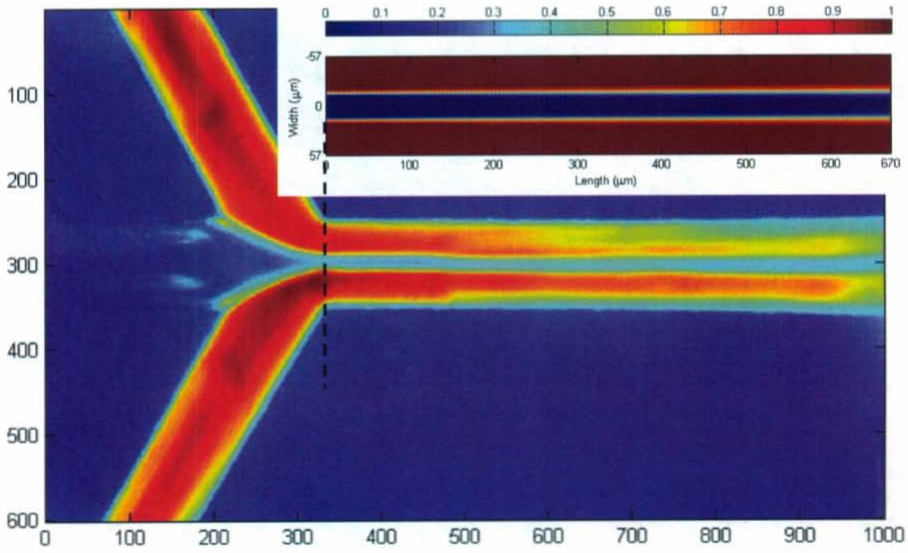

(b)

Figure 5-16 Flow of fluids in the microchannel of configuration C with a flow rate of 10 μL/min: (a) the fluorescence image of the microchannel observed by fluorescence microscopy; (b) pseudocolour image of (a). The inset is the simulation results. The white dashed lines show the edges of the microchannel.

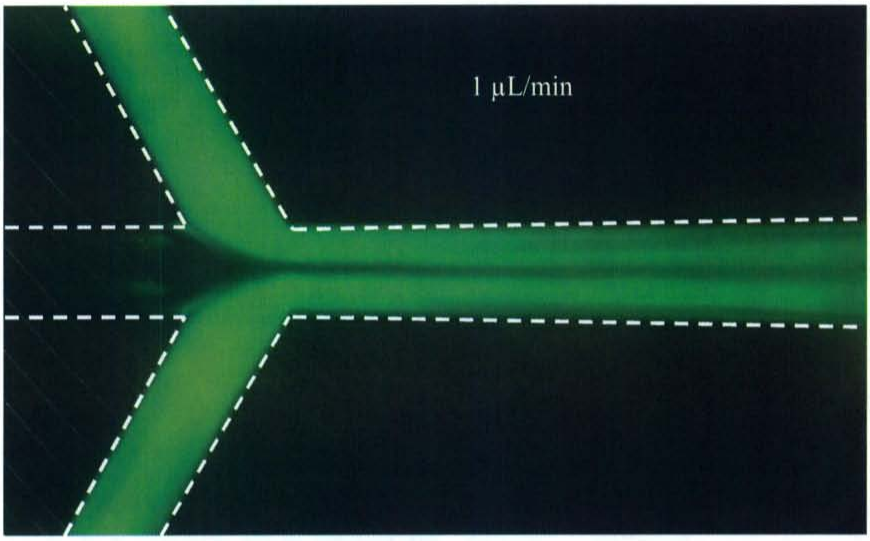

(a)

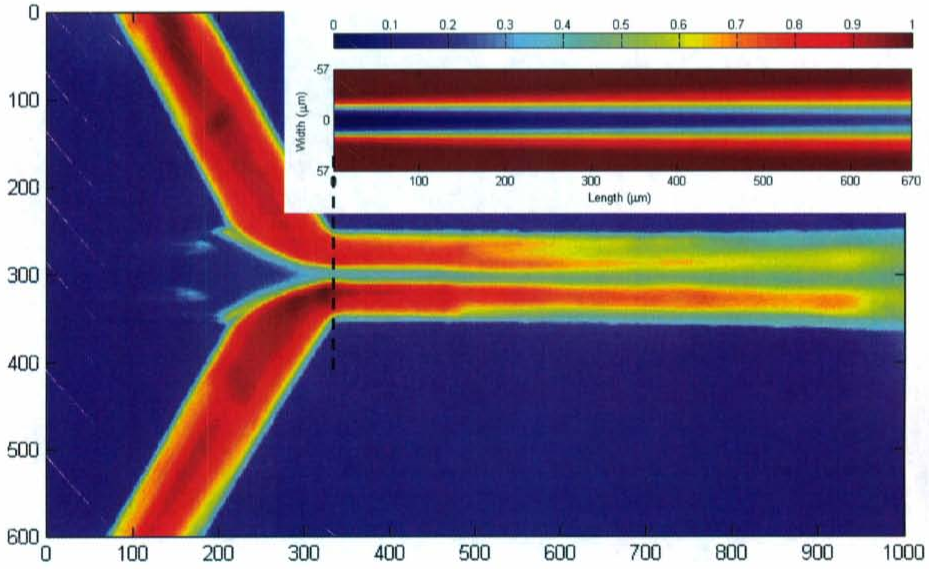

(b)

Figure 5-17 Flow of fluids in the microchannel of configuration C with a flow rate of 1 μL/min: (a) the fluorescence image of the microchannel observed by fluorescence microscopy; (b) pseudocolour image of (a). The inset is the simulation results. The white dashed lines show the edges of the microchannel.

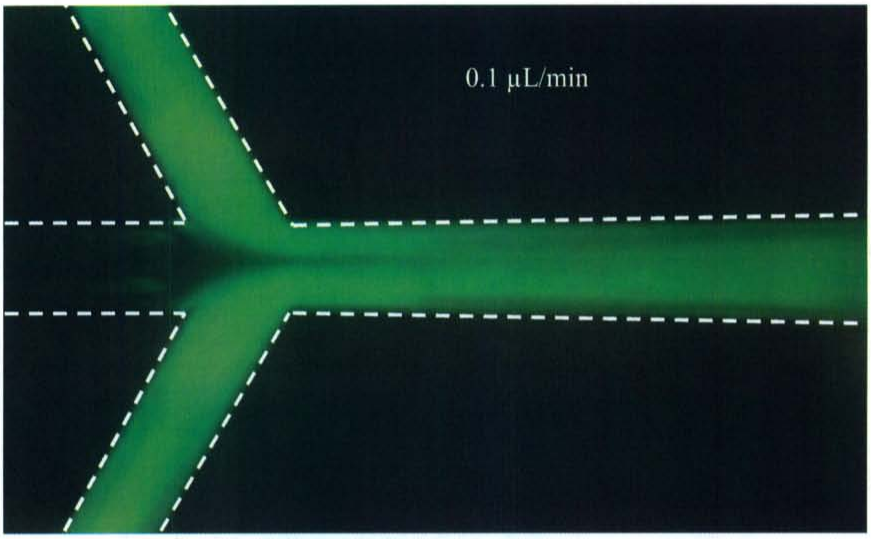

(a)

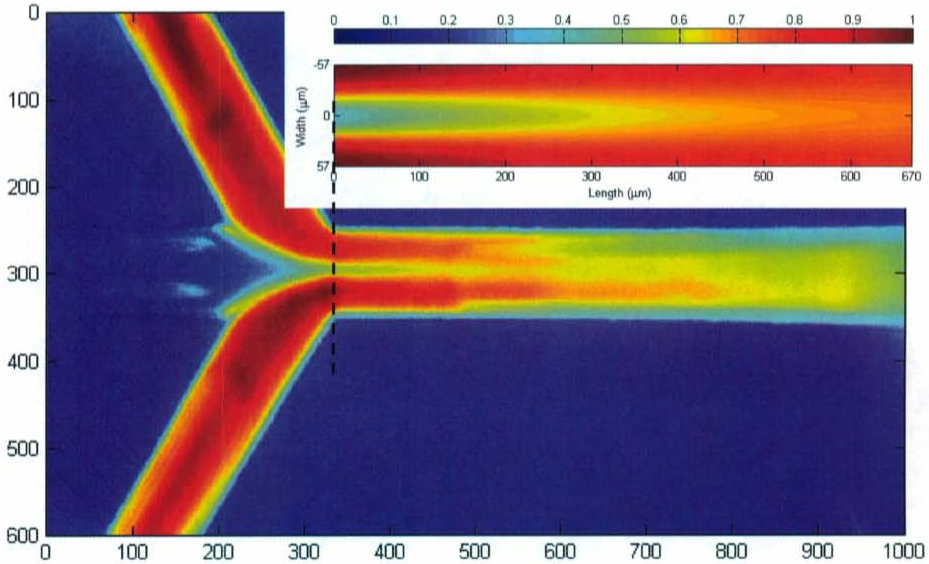

(b)

Figure 5-18 Flow of fluids in the microchannel of configuration C with a flow rate of 0.1 μL/min: (a) the fluorescence image of the microchannel observed by fluorescence microscopy; (b) pseudocolour image of (a). The inset is the simulation results. The white dashed lines show the edges of the microchannel.

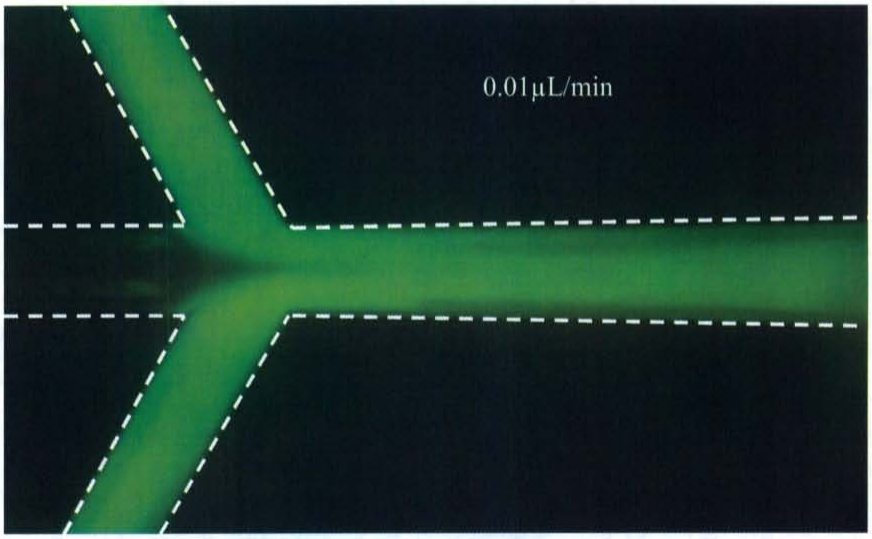

(a)

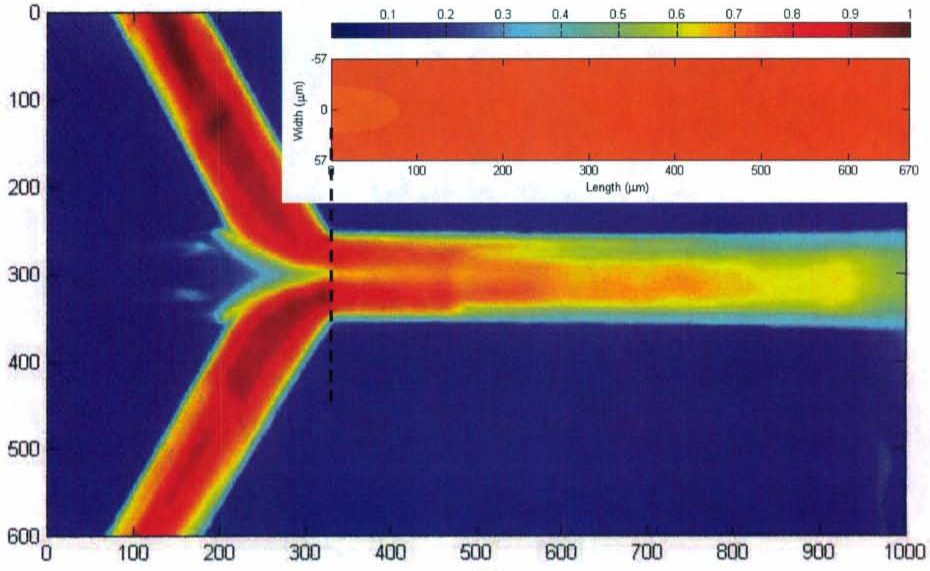

(b)

Figure 5-19 Flow of fluids in the microchannel of configuration C with a flow rate of 0.01 μL/min: (a) the fluorescence image of the microchannel observed by fluorescence microscopy; (b) pseudocolor image of (a). The inset is the simulation results. The white dashed lines show the edges of the microchannel.

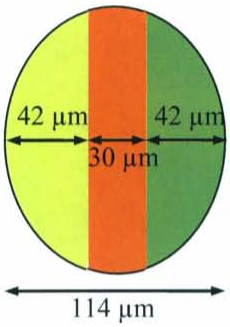

Figure 5-20 Schematic illustration of fluid distributions at the elliptical entrance of the microchannel with different colours representing different fluids.

These laminar flow experiments with opto-microfluidic devices and systems demonstrate a technique to measure diffusion coefficients of fluids as well as providing information on syringe pump speed, solution and microchannel length. Together with other optical monitoring techniques, the prototype opto-microfluidic devices and systems developed here provide possibilities to achieve real-time diagnostics of different properties, which may find applications in biological and chemical experiments. One example of particle counting will be investigated in the following chapter. In addition, high-quality microscopic images also demonstrate that femtosecond laser fabrication assisted by HF etching is an effective technique to fabricate practical opto-microfluidic devices.

Chapter 6 Opto-microfluidic particle counting

6.1 Introduction

A cell counter or hemocytometer is a device designed for counting mammalian cells, yeast and microscopic particles. It is widely used in biomedical applications for medical analysis and molecular synthesis. Conventional cell counters consist of a thick glass microscope slide with a rectangular indentation that creates a chamber. The chamber is marked with grids. The number of cells or particles is manually counted from grids with a microscope (Fig. 6-1), and thereby the concentration of cells in the fluid is calculated. Recently, image analysis software has been applied to the cell counter to produce automated counting, recording and reporting. Another automated device for cell counting is flow cytometry, in which excited fluorescence is detected and collected by multiple sensors when the suspended labeled cells flow through the instrument. Figure 6-2 shows the schematic illustration of a flow cytometry. The sample is injected into the center of a sheath flow, and the combined flow forces the cells to pass through the detection region one by one.

Flourishing cell-based life science is the essential motivation for opto-microfluidic research. Cell manipulating, counting and sorting are the main challenges to various opto-microfluidic devices. In Chapter 1, we have introduced some optofluidic flow cytometers fabricated in polymer materials. In addition, Schafer *et al.* reported a glass-based opto-microfluidic flow cytometer, in which fiber grooves and microfluidic channels are ablated on the surface of glass by femtosecond lasers and sealed to silicon by anodic bonding after the fibers are embedded in the fiber grooves [243]. Another glass-based optofluidic

flow cytometer was proposed by Kim *et al.* First, microchannels were fabricated by femtosecond laser irradiation assisted by HF etching in the bulk of fused silica, and then waveguides were directly written on the sample by femtosecond laser. Finally, a PDMS cover was bonded to the glass by a corona bonding process as a medium to connect the microchannel and capillary tube [244].

In this section, we present an opto-microfluidic particle counter fabricated in fused silica. Compared with the flow cytometry reported, the advantage of the particle counter we discuss here is that no bonding steps are needed. The real 3-dimensional microchannel with intake apertures is fabricated in the sample without an extra bonding process. In addition, no extra liquid is needed to control the cell flow (see Fig. 6-2). With our image counting program, the particle number is counted automatically at different flow rates. The precision will also be discussed.

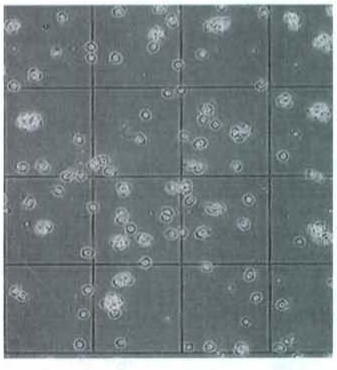

Figure 6-1 Cell counter under microscopy.

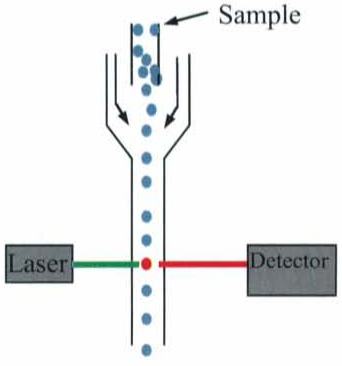

Figure 6-2 Schematic illustration of a flow cytometry.

6.2 Experimental setup

The microchannel with a diameter of 10-15 μm perfectly leads the cells to flow through the microchannel one by one. However, this requires an accurate control of the HF concentration and etching time. Figure 6-3 shows the microchannel used to assemble a flow cytometer, in which a 3-mm-long cone-shaped microchannel with a neck diameter of 16 μm is adopted. In this study, we use fluorescent particles (Thermo scientific G1000, 10 μm, 468/508 nm) which have a diameter close to blood cells (~6-8 μm). The experimental setup is shown in Fig. 6-4. White light emitted from a mercury lamp is filtered by an excitation filter. The light with a special wavelength to excite fluorescence is transmitted through the filter, whilst all remaining irradiation is suppressed. The excitation light reflects from the beam splitting mirror and shines on the microchannel using the objective lens. When fluorescent particles flow through the microchannel, the excited fluorescence passes through the beam splitting mirror which is highly transparent at the fluorescence wavelength. The fluorescence after the filter is recorded by a power meter or CCD camera and counted automatically by a computer program. A CCD camera (SONY, Power HAD, 33 FPS) is used in our experiments. A detection window is set on the video images to detect the variation of the fluorescence intensity in the microchannel. Because of the weak intensity of the fluorescence at the neck due to fast flow speed, we choose a detection window with an area of 30×25 μm^2 near the neck of the microchannel (Fig. 6-5), where most of the particles flow one by one. The dashed lines in the Fig. 6-5 show the edges of the microchannel.

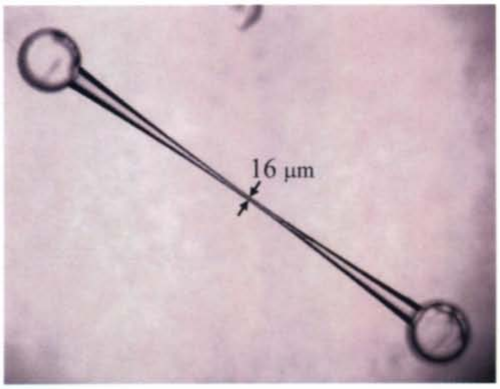

Figure 6-3 Cone-shaped microchannel for particle counting.

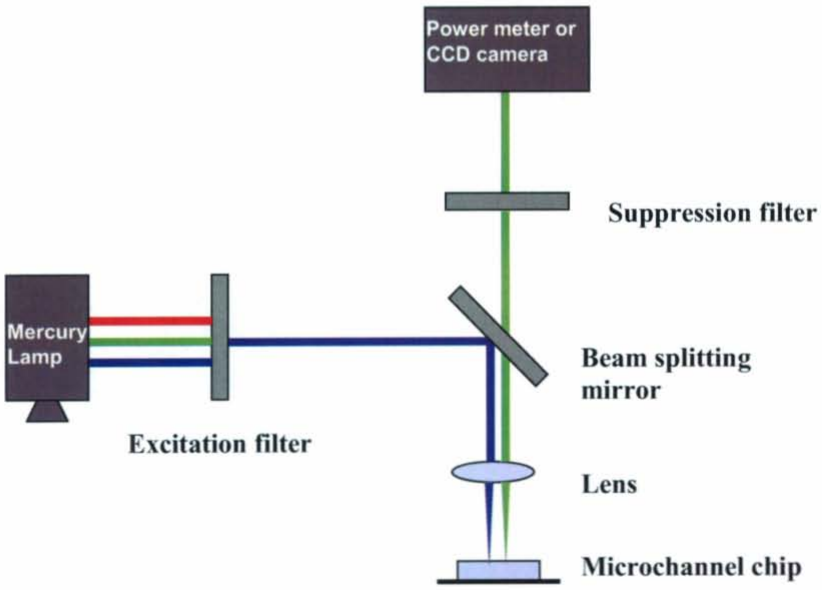

Figure 6-4 Schematic illustration of a particle counter setup used in this study.

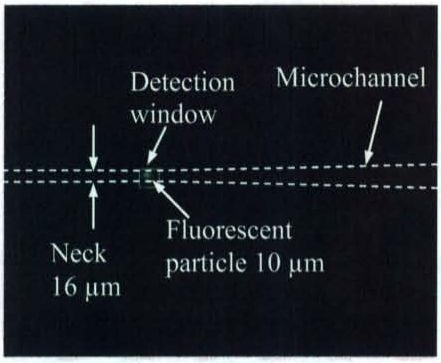

Figure 6-5 Single fluorescent particle flows through the microchannel. The dashed lines show the edges of the microchannel.

6.3 Opto-microfluidic particle counting

First, distilled water is pumped into the microchannel. A 10-second-video is recorded by the CCD camera, and then all frames are extracted from the video. The intensity of green light in the detection window is calculated frame by frame. The average intensity of green light is the background intensity. Considering the fluctuation of background intensity, an extra 5% is added to the average background intensity as the threshold. Second, the fluorescent suspensions in distilled water with concentrations of ~ 1×10^7 and 2×10^5 particles/mL are infused into the microchannel with different flow rates. The intensity of green light in the detection window of each frame is integrated in the same way as the first step. From Fig. 6-5, we know that the intensity of green light significantly increases when green fluorescent particles flow through the detection window. Finally, the number of frames with the detection window's intensity greater than the threshold is counted. From frames extraction to particles counting, all these steps can be automatically performed using a MATLAB program. The counting can be completed within 10 seconds

for a 10-second-video (327 frames with 480×640 pixels array per frame). In order to evaluate the precision of this technique, the video is played in slow motion and the particles are counted manually. Ten sets of data on the variation of fluorescent light intensity at the detection window (the result of the second step) are shown in Fig. 6-6 ~ 6-15. Each dot represents the green light intensity of the detection window in each frame, so 327 dots exist in each graph. The dashed line shows the threshold. If the intensity of a dot exceeds the threshold, it means that one particle is flowing through the detection window. Some dots show extremely high intensity in some graphs, such as Fig. 6-8, 6-9 and 6-14. The reason is that the diameter of the detection window is 25 μm; however, the diameter of a fluorescent particle is 10 μm. Occasionally, two particles flow through the detection window simultaneously which might result in a counting discrepancy. In addition, the counting discrepancy is significant at the flow rate of 0.005 μL/min. This is due to the fact that the fluorescent particle does not flow through the detective window (30 μm) in one frame time (0.033 s) at the lower flow speed. Hence, the counter indicates two or more particles flowing through instead of one (Fig. 6-10). Table 6-1 compares the counted number obtained from the MATLAB program and that from slow motion counting. Higher precision is obtained at flow rates of 0.01, 0.05 and 0.1 μL/min. From Table 6-1, the average particle intensity decreases with the increase of the flow rate. This is because that higher flow rate causes less exposure time and then weaker intensity of green light in the detection window. As the result, the intensity of green light is too weak to be separated from the background at the flow rate of 0.5 μL/min (Fig. 6-15).

It is evident that the proposed method succeeds in counting particle numbers, especially for the cases with a flow rate in the range of 0.01 ~ 0.1 μL/min. Particle

counting with higher precision could be achieved if detection devices of higher resolution are adopted.

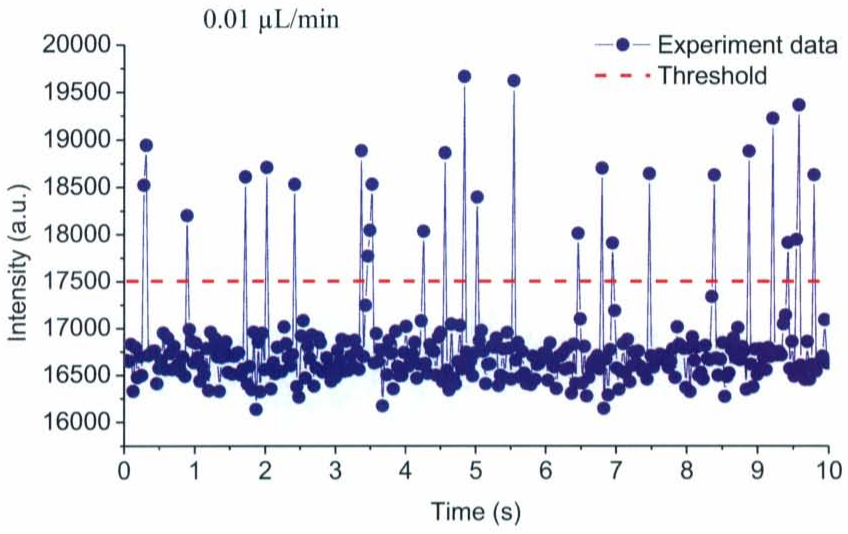

Figure 6-6 Fluorescent light intensity collected at the detection window in the flow rate of 0.01 μL/min

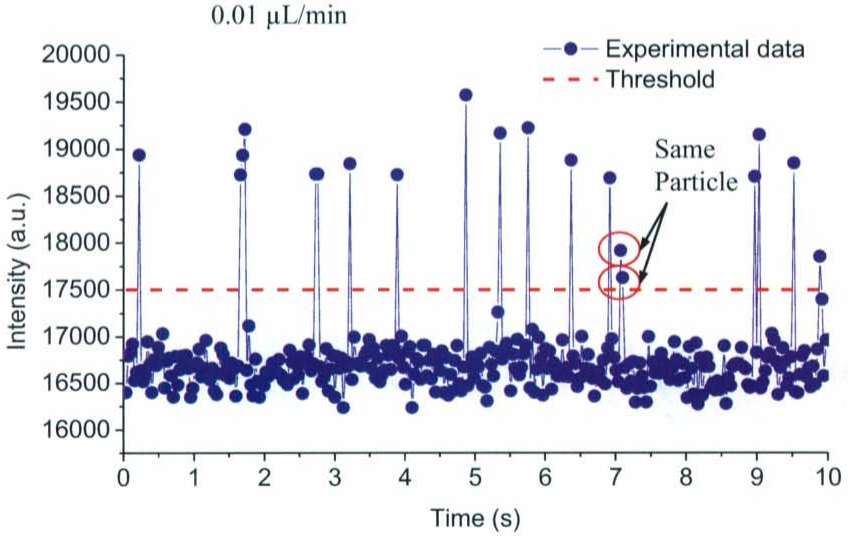

Figure 6-7 Fluorescent light intensity collected at the detection window in the flow rate of 0.01 μL/min.

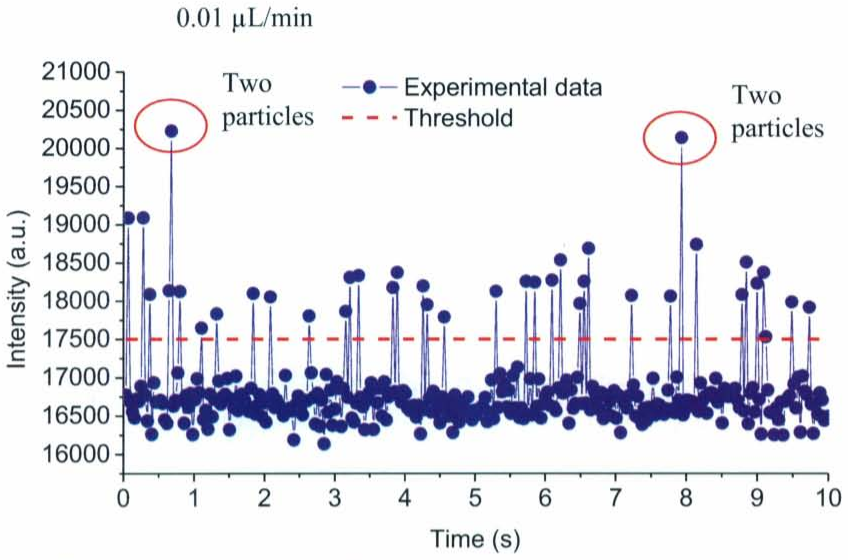

Figure 6-8 Fluorescent light intensity collected at the detection window in the flow rate of 0.01 μL/min.

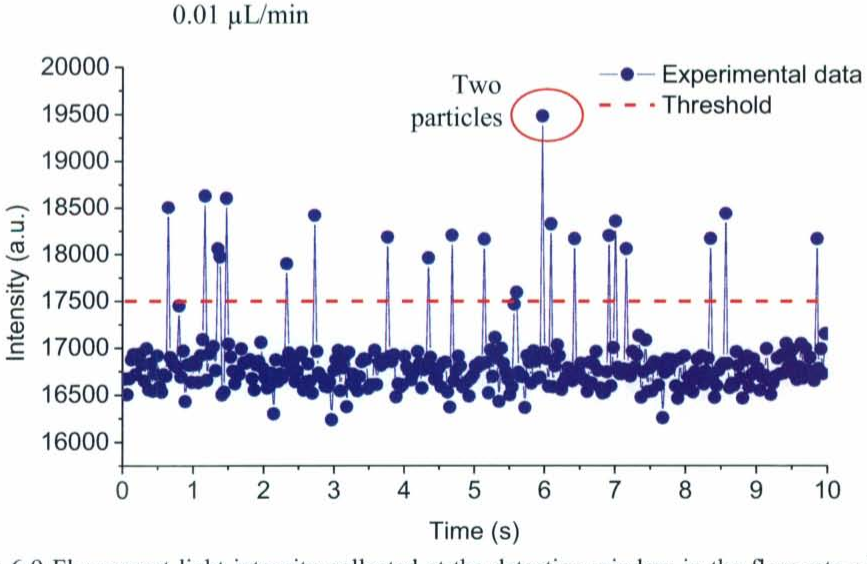

Figure 6-9 Fluorescent light intensity collected at the detection window in the flow rate of 0.01 μL/min.

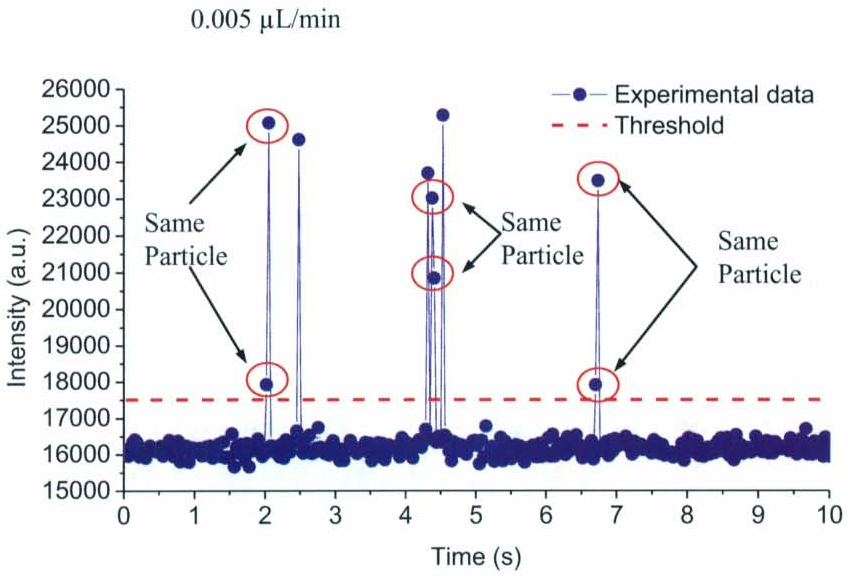

Figure 6-10 Fluorescent light intensity collected at the detection window in the flow rate of 0.005 μL/min.

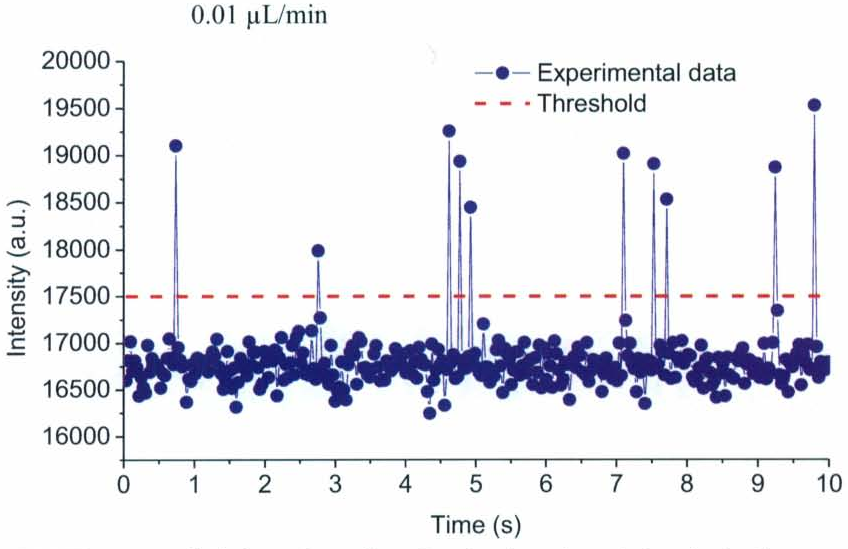

Figure 6-11 Fluorescent light intensity collected at the detection window in the flow rate of 0.01 μL/min.

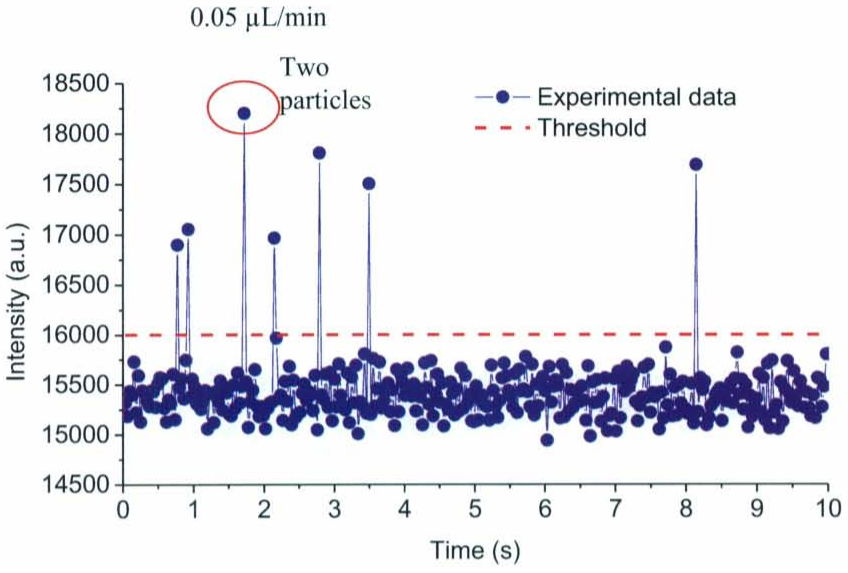

Figure 6-12 Fluorescent light intensity collected at the detection window in the flow rate of 0.05 μL/min.

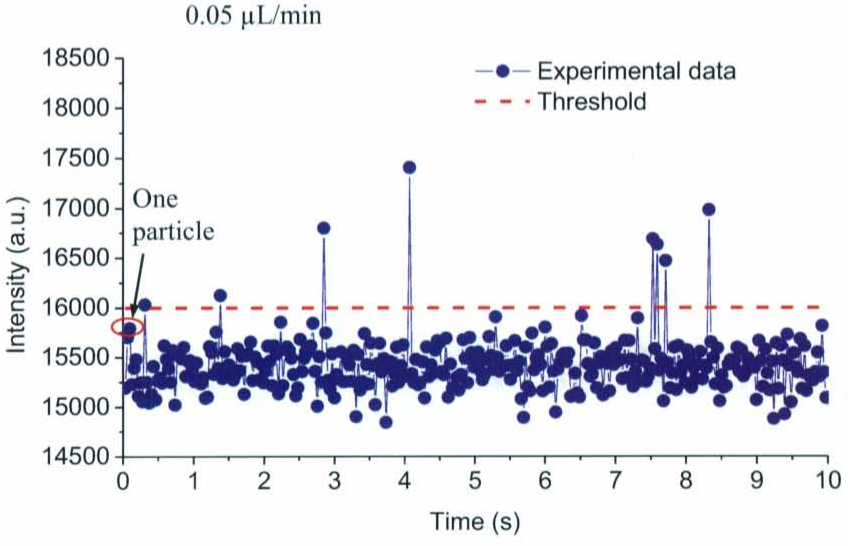

Figure 6-13 Fluorescent light intensity collected at the detection window in the flow rate of 0.05 μL/min.

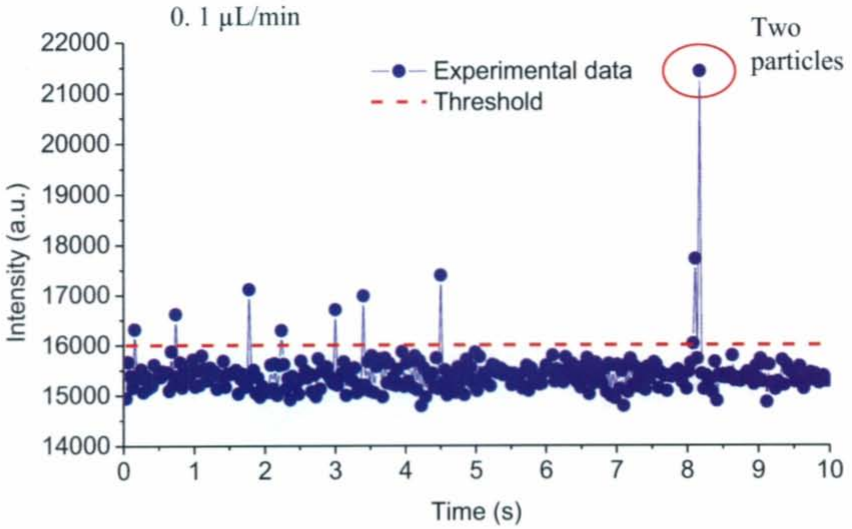

Figure 6-14 Fluorescent light intensity collected at the detection window in the flow rate of 0.1 μL/min.

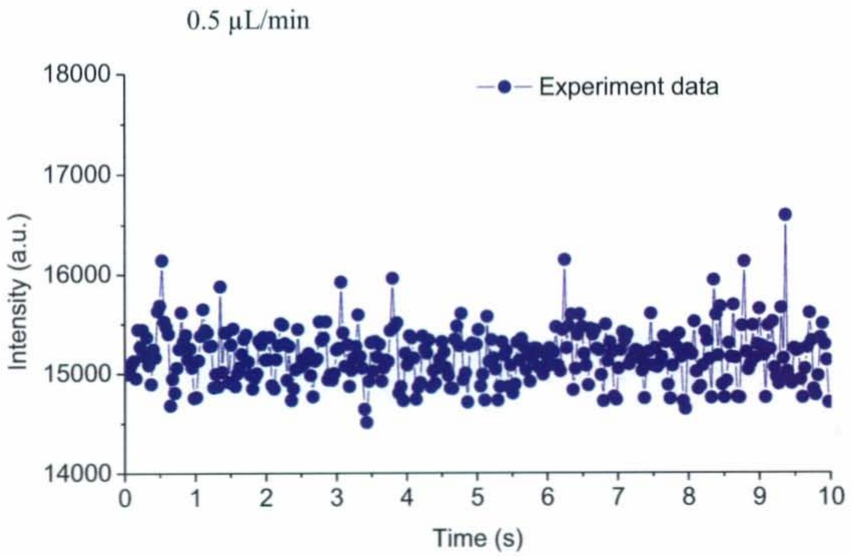

Figure 6-15 Fluorescent light intensity collected at the detection window in the flow rate of 0.5 μL/min.

Table 6-1 Comparison between the counting number from the MATLAB program and the accurate number read from slow motion counting.

Figure	**Concentration (particles/mL)**	**Flow rate (μL/min)**	**Counting number**	**Real number**	**Average particle intensity (a.u.)**	**Average background Intensity (a.u.)**	**Threshold (a.u.)**
6-6	10^7	0.01	26	26	18500	16700	17500
6-7	10^7	0.01	19	18	18500	16700	17500
6-8	10^7	0.01	38	40	18500	16700	17500
6-9	10^7	0.01	21	22	18500	16700	17500
6-10	10^7	0.005	9	6	23500	16200	17500
6-11	10^7	0.01	10	10	18500	16700	17500
6-12	2×10^5	0.05	7	8	17000	15300	16000
6-13	2×10^5	0.05	8	9	17000	15300	16000
6-14	2×10^5	0.1	9	10	16750	15300	16000
6-15	2×10^5	0.5	-	-	15750	15300	-

Chapter 7 Conclusions

The femtosecond laser is a powerful tool for three-dimensional micromachining and microfabrication. Various features in fused silica fabricated by the femtosecond laser at different fabrication parameters have been achieved and analyzed, indicating that a femtosecond laser is effective to fabricate microstructures with minimized heat-affected zones. In addition to type II waveguides fabrication in the fused silica, we explored the origins of type II waveguides by analyzing the Raman spectra near the irradiation region. Near-field images also demonstrated the success of type II waveguide fabrication. The propagation loss has been found to be ~4 dB/cm after coupling with a laser at 1550 nm.

Microchannels in fused silica have been successfully fabricated by the femtosecond laser microfabrication assisted by HF acid etching. The shapes, variable channel widths and attachment of intake apertures of the opto-microfluidic devices fabricated by the femtosecond laser of different laser energy, polarization, writing speed, and etching time have been investigated. Microchannels of complex configurations, such as T-shaped, Y-shaped, three-intake and conical microchannels, have been fabricated by using optimized parameters. Integrated with capillary tubes, syringe needles, syringes, and syringe pumps, the prototypes of opto-microfluidic devices and systems have been assembled and used in preliminary experiments.

Laminar flow experiments with opto-microfluidic devices and systems fabricated in this study have revealed flow mechanisms at the microscale, indicating that neither eddies nor swirls exist in the microchannel. Diffusion is the major impetus for particle transportation along the perpendicular direction of microchannels. Simulations performed

with the MATLAB program have also verified the experimental results. These results not only provide us with a technique to measure diffusion coefficient, but also give us the possibility of identifying the buffer solutions or diluents used in biological or chemical opto-microfluidic experiments. For important biomedical applications of opto-microfluidic devices, the validity of the particle counter has been experimentally demonstrated, in which the number of fluorescent particles has been automatically counted with a CCD camera through a MATLAB program when the particles flow through the microchannel. Optimal results have been obtained with the particle concentration of 10^7 particles/mL at a flow rate of 0.01 μL/min. The technique possesses the possibility for further improvement in the performance of particle counting if detection devices of high resolution are adopted.

More complex opto-microfluidic devices will be designed and fabricated in fused silica by the femtosecond laser fabrication in the future work, such as integration of microchannels and waveguides, microlens and gratings. Therefore, multiple functions (such as measurement of refractive index and temperature) could be achieved in these devices. In addition, other materials, such as PDMS and SU-8, may be applied in the fabrication of opto-microfluidic devices. Some opto-microfluidic sensors (MZI and SPR) for optical and biological measurements are interesting topics for future exploration.

Publication List

Parts of this thesis work have been published in a refereed journal paper and presented in three conferences. Several manuscripts for journal submissions are currently under preparation.

1. (Invited) D. Zhang, L. Men, and Q. Chen, "Microfabrication and applications of opto-microfluidic sensors," *Sensors* **11,** 5360 (2011).
2. D. Zhang and Q. Chen, "Femtosecond laser microfabrication of versatile microchannels in fused silica," Photonics North 2011, Ottawa, Canada (May 2011).
3. D. Zhang and Q. Chen, "Three-dimensional opto-microfluidic channels fabricated by femtosecond laser," Canadian Association of Physicsts (CAP) Congress 2011, St. John's, Canada (June 2011).
4. D. Zhang and Q. Chen, "High precision ultrafast laser microfabrication," IEEE Newfoundland Electrical and Computer Engineering Conference (NECEC) 2010, St. John's, Canada (November, 2010).

Bibliography

1. W. M. Steen and J. Mazumder, "*Laser material processing*," 3rd ed., London: Springer, 2003.
2. O. Svelto, "*Principles of lasers*," 5th ed., New York: Springer, 2009.
3. D. Basting and G. Marowsky, "*Excimer laser technology*," Berlin: Springer, 2005.
4. K. Miura, J. Qui, H. Inouye, T. Mitsuyu, and K. Hirao, "Photowritten optical waveguides in various glasses with ultrashort pulse laser," *Appl. Phys. Lett.* **71**, 3329 (1997).
5. S. L. Chin, "*Femtosecond laser filamentation*," New York: Springer, 2009.
6. L. V. Keldysh, "Ionization in the field of a strong electromagnetic wave," *Sov. Phys. JETP.* **28**, 1307 (1965).
7. K. Miura, J. R. Qiu, H. Inouye, T. Mitsuyu, and K. Hirao, "Photowritten optical waveguides in various glasses with ultrashort pulse laser," *Appl. Phys. Lett.* **71**, 3329 (1997).
8. J. Liu, Z. Zhang, C. Flueraru, X. Liu, S. Chang, and C. P. Grover, "Waveguide shaping and writing in fused silica using a femtosecond laser," *IEEE J. Sel. Top. Quan. Elec.* **10**, 169 (2004).
9. C. W. Ponader, J. F. Schroeder, and A. M. Streltsov, "Origin of the refractive-index increase in laser-written waveguides in glasses," *J. Appl. Phys.* **103**, 063516 (2008).
10. E. Bricchi, J. D. Mills, P. G. Kazansky, B. G. Klappauf and J. J. Baumberg, "Birefringent Fresnel zone plates in silica fabricated by femtosecond laser machining," *Opt. Lett.* **27**, 2200 (2002).
11. E. Bricchi, B. G. Klappauf and P. G. Kazansky, "Form birefringence and negative index change created by femtosecond direct writing in transparent materials," *Opt. Lett.* **29**, 119 (2004).
12. C. Marceau, Y. Chen, F. Théberge, M. Châteauneuf, J. Dubois and S. L. Chin, "Ultrafast birefringence induced by a femtosecond laser filament in gases," *Opt. Lett.* **34**, 1417 (2009).
13. S. Juodkazis, H. Misawa, T. Hashimoto, E. G. Gamaly and B. L. Davies, "Laser-induced microexplosion confined in a bulk of silica: formation of nanovoids," *Appl. Phys. Lett.* **88**, 201909 (2006).
14. E. Toratani, M. Kamata and M. Obara, "Self-fabrication of void array in fused silica by femtosecond laser processing," *Appl. Phys. Lett.* **87**, 171103 (2005).
15. C. B. Schaffer, A. O. Jamison, and E. Mazur, "Morphology of femtosecond laser-induced structural changes in bulk transparent materials," *Appl. Phys. Lett.* **84**, 1441 (2004).
16. K. M. Davis, K. Miura, N. Sugimoto, K. Hirao, "Writing waveguides in glass with a femtosecond laser," *Opt. Lett.* **21**, 1729 (1996).
17. B. McMillen, K. P. Chen, and D. Jaque, "Microstructural imaging of high repetition rate ultrafast laser written $LiTaO_3$ waveguides," *Appl. Phys. Lett.* **94**, 081106 (2009).

18. R. An, Y. Li, D. Liu, Y. Dou, F. Qi, H. Yang and Q. Gong, "Optical waveguide writing inside Foturan glass with femtosecond laser pulses," *Appl. Phys. A* **86**, 343 (2007).
19. R. R. Thomson, S. Campbell, I. J. Blewett, A. K. Kar and D. T. Reid, "Active waveguide fabrication in erbium-doped oxyfluoride silicate glass using femtosecond pulses," *Appl. Phys. Lett.* **87**, 121102 (2005).
20. N. D. Psaila, R. R. Thomson, H. T. Bookey, A. K. Kar, N. Chiodo, R. Osellame, G. Cerullo, A. Jha and S. Shen, "Er: Yb-doped oxyfluoride silicate glass waveguide amplifier fabricated using femtosecond laser inscription," *Appl. Phys. Lett.* **90**, 131102 (2007).
21. D. K. Y. Low, H. Xie, Z. Xiong and G. C. Lim "Femtosecond laser direct writing of embedded optical waveguides in aluminosilicate glass," *Appl. Phys. A* **81**, 1633 (2005).
22. J. W. Chan, T. R. Huser, S. H. Risbud, J. S. Hayden and D. M. Krol, "Waveguide fabrication in phosphate glasses using femtosecond laser pulses," *Appl. Phys. Lett.* **82**, 2371 (2003).
23. D. Blömer, A. Szameit, F. Dreisow, T. Schreiber, S. Nolte and A. Tünnermann, "Nonlinear refractive index of fs-laser-written waveguides in fused silica," *Opt. Express* **14**, 2151 (2006).
24. A. Zoubir, M. Richardson, L. Canioni, A. Brocas, and L. Sarger, "Optical properties of infrared femtosecond laser-modified fused silica and application to waveguide fabrication," *J. Opt. Soc. Am. B* **22**, 2138 (2005).
25. M. Will, S. Nolte, B. N. Chichkov and A. Tunnermann, "Optical properties of waveguides fabricated in fused silica by femtosecond laser pulses," *Appl. Opt.* **41**, 4360 (2002).
26. T. Allsop, M. Dubov, V. Mezentsev and I. Bennion, "Inscription and characterization of waveguides written into borosilicate glass by a high-repetition-rate femtosecond laser at 800nm," *Appl. Opt.* **49**, 1938 (2010).
27. A. Saliminia, N. T. Nguyen, M. C. Nadeau, S. Petit, S. L. Chin and R. Vallee, "Writing optical waveguides in fused silica using 1 kHz femtosecond infrared pulses," *J. Appl. Phys.* **93**, 3724 (2003).
28. N. D. Psaila, R. R. Thomson, H. T. Bookey, A. K. Kar, N. Chiodo, R. Osellame, G. Cerullo, G. Brown, A. Jha and S. Shen, "Femtosecond laser inscription of optical waveguides in Bismuth ion doped glass," *Opt. Express* **14**, 10452 (2006).
29. G. Cerullo, R. Osellame, S. Taccheo and M. Marangoni, "Femtosecond micromachining of symmetric waveguides at 1.5 μm by astigmatic beam focusing," *Opt. Lett.* **27**, 1938 (2002).
30. R. Osellame, S. Taccheo and M. Marangoni, "Femtosecond writting of active optical waveguides with astigmatically shaped beams," *J. Opt. Soc. Am. B* **20**, 1559 (2003).
31. Y. Cheng, K. Sugioka, and K. Midorikawa, "Control of the cross-sectional shape of a hollow microchannel embedded in photostructurable glass by use of a femtosecond laser," *Opt. Lett.* **28**, 55 (2003).

32. F. He, H. Xu, Y Cheng, J. Ni, H. Xiong, Z. Xu, K. Sugioka and K. Midorikawa, "Fabrication of microfluidic channels with a circular cross section using spatiotemporally focused femtosecond laser pulses," *Opt. Lett.* **35**, 1106 (2010).
33. D. Homoelle, S. Wielandy, A. L. Gaeta, N. F. Borrelli, and C. Smith, "Infrared photosensitivity in silica glasses exposed to femtosecond laser pulses," *Opt. Lett.* **24**, 1311 (1999).
34. S. Nolte, M. Will, J. Burghoff, and A. Tuennermann, "Femtosecond waveguide writing: a new avenue to three-dimensional integrated Optics," *Appl. Phys. A* **77**, 109 (2003).
35. J. Liu, Z. Zhang, S. Chang, C. Flueraru, and C. P. Grover, "Directly writing of 1-to-N optical waveguide power splitters in fused silica glass using a femtosecond laser," *Opt. Comm.* **253** , 315 (2005).
36. W. Watanabe, T. Asano, K. Yamada, K. Itoh, and J. Nishii, "Wavelength division with three-dimensional couplers fabricated by filamentation of femtosecond laser pulse," *Opt. Lett.* **28**, 2491 (2003).
37. K. Minoshima, A. Kowalevicz, E. Ippen, and J. Fujimoto, "Fabrication of coupled mode photonic devices in glass by nonlinear femtosecond laser materials processing," *Opt. Express* **10**, 645 (2002).
38. T. Pertsch, U. Peschel, F. Lederer, J. Burghoff, M. Will, S. Nolte, and A. Tünnermann, "Discrete diffraction in two-dimensional arrays of coupled waveguides in silica," *Opt. Lett.* **29**, 468 (2004).
39. H. Chen, X. Chen, Y. Xia, D. Liu, Y. Li, and Q. Gong, "Beam coupling in 2×2 waveguide arrays in fused silica fabricated by femtosecond laser pulses," *Opt. Express* **15**, 5445 (2007).
40. A. Szameit1, F. Dreisow, T. Pertsch, S. Nolte and A. Tunnermann, "Control of directional evanescent coupling in fs laser written waveguides," *Opt. Express* **15**, 1579 (2007).
41. W. Watanabe, Y. Note, and K. Itoh, "Fabrication of multimode interference waveguides in glass by use of a femtosecond laser," *Opt. Lett.* **30**, 2888 (2005).
42. A. S. Vengurlekar, "Polarization dependence of optical properties of metallodielectric gratings with subwavelength grooves in classical and conical mounts," *J. Appl. Phys.* **104**, 023109 (2008).
43. K. C. Vishnubhatla, S. V. Rao, R. S. S. Kumar, M. Ferrari, and D. N. Rao, "Optical studies of two dimensional gratings in fused silica, GE 124, and Foturan glasses fabricated using femtosecond laser pulses," *Opt. Comm.* **282**, 4537 (2009).
44. K. C. Vishnubhatla, S. V. Rao, R. S. S. Kumar, R. Osellame, S. N. B. Bhaktha, S. Turrell, A. Chiappini, A. Chiasera, M. Ferrari, M. Mattarelli, M. Montagna, R. Ramponi, G. C. Righini, and D. N. Rao, "Femtosecond laser direct writing of gratings and waveguides in high quantum efficiency erbium-doped Baccarat glass," *J. Phys. D: Appl. Phys.* **42**, 205106 (2009).
45. F. He, H. Sun, M. Huang, J. Xu, Y. Liao, Z. Zhou, Y. Cheng, Z. Xu, K. Sugioka, and K. Midorikawa, "Rapid fabrication of optical volume gratings in Foturan glass by femtosecond laser micromachining," *Appl. Phys. A* **97**, 853 (2009).
46. D. L. N. Kallepalli, N. R. Desai, and V. R. Soma, "Fabrication and optical characterization of microstructures in poly (methylmethacrylate) and poly

(dimethylsiloxane) using femtosecond pulses for photonic and microfluidic applications," *Appl. Opt.* **49**, 2475 (2010).
47. S. Taccheo, G. Della Valle, R. Osellame, G. Cerullo, N. Chiodo, P. Laporta, O. Svelto, A. Killi, U. Morgner, M. Lederer, and D. Kopf, "Er: Yb-doped waveguide laser fabricated by femtosecond laser pulses," *Opt. Lett.* **29**, 2626 (2004).
48. A. Marcinkevicius, S. Juodkazis, M. Watanabe, M. Miwa, S. Matsuo, H. Misawa, and J. Nishii, "Femtosecond laser-assisted three-dimensional microfabrication in silica," *Opt. Lett.* **26**, 277 (2001).
49. S. Matsuo, H. Sumi, S. Kiyama, T. Tomita, and S. Hashimoto, "Femtosecond laser-assisted etching of Pyrex glass with aqueous solution of KOH," *Appl. Surf. Sci.* **255**, 9758 (2009).
50. K. C. Vishnubhatla, N. Bellini, R. Ramponi, G. Cerullo, and R. Osellame, "Shape control of microchannels fabricated in fused silica by femtosecond laser irradiation and chemical etching," *Opt. Express* **17**, 8685 (2009).
51. F. He, Y. Cheng, Z. Xu, Y. Liao, J. Xu, H. Sun, C. Wang, Z. Zhou, K. Sugioka, K. Midorikawa, Y. Xu, and X. Chen, "Direct fabrication of homogeneous microfluidic channels embedded in fused silica using a femtosecond laser," *Opt. Lett.* **35**, 282 (2010).
52. Y. Li, K. Itoh, W. Watanabe, K. Yamada, D. Kuroda, J. Nishii, and Y. Jiang, "Three-dimensional hole drilling of silica glass from the rear surface with femtosecond laser pulses," *Opt. Lett.* **26**, 1912 (2001).
53. D. J. Hwang, T. Y. Choi, C. P. Grigoropoulos, "Liquid-assisted femtosecond laser drilling of straight and three-dimensional microchannels in glass," *Appl. Phys. A* **79**, 605 (2004).
54. C. Li, X. Shi, J. Si, T. Chen, F. Chen, A. Li, and X. Hou, "Fabrication of three-dimensional microfluidic channels in glass by femtosecond pulses," *Opt. Comm.* **282**, 657 (2009).
55. D. J. Hwang, K. Hiromatsu, H. Hidai, and C. P. Grigoropoulos, "Self-guided glass drilling by femtosecond laser pulses," *Appl. Phys. A* **94**, 555 (2009).
56. R. An, Y. Li, Y. Dou, H. Yang, and Q. Gong, "Simultaneous multi-microhole drilling of sodalime glass by water-assisted ablation with femtosecond laser pulses," *Opt. Express* **13**, 1855 (2005).
57. R. An, Y. Li, Y. Dou, D. Liu, H. Yang, and Q. Gong, "Water-assisted drilling of microfluidic chambers inside silica glass with femtosecond laser pulses," *Appl. Phys. A* **83**, 27 (2006).
58. G. M. Whitesides, "The origins and the future of micofluidics," *Nature* **442**, 368 (2006).
59. J. C. Mcdonald, D. C. Duffy, J. R. Anderson, D. T. Chiu, H. Wu, O. J. A. Schueller, and G. M. Whitesides, "Fabrication of microfluidic systems in poly(dimethylsiloxane)," *Electrophoresis* **21**, 27 (2000).
60. C. Monat, P. Domachuk, and B. J. Eggleton, "Integrated optofluidics: a new river of light," *Nat. Photonics* **1**, 106 (2007).
61. D. Psaltis, S. R. Quake, and C. Yang, "Developing optofluidic technology through the fusion of microfluidics and optics," *Nature* **442**, 381 (2006).

62. Y. Fainman, L. P. Lee, D. Psaltis, and C. Yang, "*Optofluidics: fundamentals, devices, and applications*" The McGraw-Hill Companies, 2010.
63. D. Zhang, L. Men, and Q. Chen, "Microfabrication and applications of opto-microfluidic sensors," *Sensors* **11**, 5360 (2011).
64. S. C. Terry, J. H. Jerman, and J. B. Angell, "A gas chromatographic air analyzer fabricated on a silicon wafer," *IEEE Trans. Elect. Dev.* **26,** 1880 (1979).
65. K. Seiler, D. J. Harrison, and A. Manz, "Planar glass chip for capillary electrophoresis: repetitive sample injection, quantitation, and separation efficiency," *Anal. Chem.* **65**, 1481 (1993).
66. K. Fluri, G. Fitzpatrick, N. Chiem, and D. J. Harrison, "Integrated capillary electrophpresis devices with an efficient postcolumn reactor in planar quartz and glass chips," *Anal. Chem.* **68**, 4285 (1996).
67. J. Khandurina, S. C. Jacobson, L. C. Waters, R. S. Foote, and J. M. Ramsey, "Microfabricated porous membrane structure for sample concentration and electrophoretic analysis," *Anal. Chem.* **71**, 1815 (1999).
68. T. Koerner, L. Brown, R. Xie, and R. D. Oleschuk, "Epoxy resins as stamps for hot embossing of microstructures and microfluidic channels," *Sens. Actuat. B* **107**, 632 (2005).
69. S. Ssenyange, J. Taylor, D. J. Harrison, and M. T. McDermott, "A glassy carbon microfluidic device for electrospray mass spectrometry," *Anal. Chem.* **76**, 2393 (2004).
70. P. P. Shiu, G. K. Knopf, M. Ostojic, and S. Nikumb, "Rapid fabrication of tooling for microfluidic devices via laser micromachining and hot embossing," *J. Micromech. Microeng.* **18**, 025012 (2008).
71. P. P. Shiu, G. K. Knopf, M. Ostojic, and S. Nikumb, "Rapid fabrication of micromolds for polymeric microfluidic devices," 21st Canadian Conference on Electrical and Computer Engineering (CCECE), Vancouver, BC, Canada, 22–26 April 2007; pp. 8-11.
72. P. P. Shiu, G. K. Knopf, M. Ostojic, and S. Nikumb, "Fabrication of polymer microfluidic devices with 3D microfeatures that have near optical surface quality," Microsystems and Nanoelectronics Research Conference (MNRC), Ottawa, Ont., Canada, 15 October 2008; pp. 53-56.
73. N. S. Cameron, H. Roberge, T. Veres, S. C. Jakeway, and H. J. Crabtree, "High fidelity, high yield production of microfluidic devices by hot embossing lithography: Rheology and stiction," *Lab Chip* **6**, 936 (2006).
74. S. M. Azmayesh-Fard, E. Flaim, and J. N. McMullin, "PDMS biochips with integrated waveguides," *J. Micromech. Microeng.* **20**, 087002 (2010).
75. B. Wang, Z. Abdulali-Kanji, E. Dodwell, J. H. Horton, and R. D. Oleschuk, "Surface characterization using chemical force microscopy and the flow performance of modified polydimethylsiloxane for microfluidic device applications," *Electrophoresis* **24**, 1442 (2003).
76. B. G. Subramani and P. R. Selvaganapathy, "Surface micromachined PDMS microfluidic devices fabricated using a sacrificial photoresist," *J. Micromech. Microeng.* **19**, 015013 (2009).

77. Y. Xi, D. A. Duford, and E. D. Salin, "Automated liquid-solid extraction of pyrene from soil on centrifugal microfluidic devices," *Talanta* **82**, 1072 (2010).
78. P. J. Bock, P. Cheben, J. H. Schmid, J. Lapointe, A. Delâge, S. Janz, G. C. Aers, D. Xu, A. Densmore, and T. J. Hall, "Subwavelength grating periodic structures in silicon-on-insulator: a new type of microphotonic waveguide," *Opt. Express* **18**, 20251 (2010).
79. P. Dumais, C. L. Callender, J. P. Noad, and C. J. Ledderhof, "Integrated optical sensor using a liquid-core waveguide in a Mach-Zehnder interferometer," *Opt. Express* **16**, 18164 (2008).
80. C. L. Bliss, J. N. McMullin, and C. J. Backhouse, "Integrated wavelength-selective optical waveguides for microfluidic-based laser-induced fluorescence detection," *Lab Chip* **8**, 143 (2008).
81. A. D. Densmore, X. Xu, S. Janz, P. Waldron, J. Lapointe, T. Mischki, G. Lopinski, A. Delage, J. H. Schmid, and P. Cheben, "Sensitive label-free biomolecular detection using thin silicon waveguides," *Adv. Opt.* Technol., Article ID 725967 (2008).
82. T. Kowpak, B. R. Watts, Z. Zhang, S. Zhu, and C. Xu, "Fabrication of photonic/microfluidic integrated devices using an epoxy photoresist," *Macromol. Mater. Eng.* **295**, 559 (2010).
83. H. Y. Zheng, H. Liu, S. Wan, G. C. Lim, S. Nikumb, and Q. Chen, "Ultrashort pulse laser micromachined microchannels and their application in an optical switch," *Int. J. Adv. Manuf. Technol.* **27**, 925 (2006).
84. H. Zhang, S. Ho, S. M. Eaton, J. Li, and P. R. Herman, "Three-dimensional optical sensing network written in fused silica glass with femtosecond laser," *Opt. Express* **16**, 14015 (2008).
85. L. Shah, A. Y. Arai, S. M. Eaton, and P. R. Herman, "Waveguide writing in fused silica with a femtosecond fiber laser at 522 nm and 1 MHz repetition rate," *Opt. Express* **13**, 1999 (2005).
86. C. Blake and B. J. Gould, "Use of enzymes in immunoassay techniques. A review," *Analyst* **109**, 533 (1984).
87. D. Wild, "The Immunoassay Handbook," 3rd ed., Oxford: Elsevier, 2008.
88. S. R. Mikkelsen and E. Corton, "*Bioanalytical Chemistry*," Hoboken: Wiley, 2004.
89. F. Y. H. Lin, M. Sabri, D. Erickson, J. Alirezaie, D. Li, and P. M. Sherman, "Development of a novel microfluidic immunoassay for the detection of Helicobacter pylori infection," *Analyst* **129**, 823 (2004).
90. Y. Gao, F. Y. H. Lin, G. Hu, P. M. Sherman, and D. Li, "Development of a novel electrokinetically driven microfluidic immunoassay for the detection of Helicobacter pylori," *Anal. Chim. Acta* **543**, 109 (2005).
91. Q. Xiang, G. Hu, Y. Gao, and D. Li, "Miniaturized immunoassay microfluidic system with electrokinetic control," *Biosens. Bioelectron.* **21**, 2006 (2006).
92. R. Peytavi, F. R. Raymond, D. Gagné, J. Picard, G. Jia, J. Zoval, M. Madou, K. Boissinot, M. Boissinot, L. Bissonnette, M. Ouellette, and M. G. Bergeron, "Microfluidic device for rapid (<15 min) automated microarray hybridization," *Clin. Chem.* **51**, 1836 (2005).

93. P. Roos and C. D. Skinner, "A two bead immunoassay in a micro fluidic device using a flat laser intensity profile for illumination," *Analyst* **128**, 527 (2003).
94. M. Herrmann, T. Veresb, and M. Tabrizian, "Enzymatically-generated fluorescent detection in micro-channels with internal magnetic mixing for the development of parallel microfluidic ELISA," *Lab Chip* **6**, 555 (2006).
95. F. Y. H. Lin, M. Sabri, J. Alirezaie, D. Li, and P. M. Sherman, "Development of a nanoparticle-labeled microfluidic immunoassay for detection of pathogenic microorganisms," *Clin. Diagn. Lab Immunol.* **12**, 418 (2005).
96. P. Schmitt-Kopplin and H.Munchen, "*Capillary Electrophoresis: methods and protocols*," Totowa: Humana Press, 2008.
97. D. A Skoog, F. J. Holler, and S. R. Crouch, "*Principles of Instrumental Analysis*," 6th ed., Belmont: Thomson Brooks/Cole, 2007.
98. P. Taylor, D. P. Managea, K. E. Helmle, Y. Zheng, D. M. Glerum, and C. J. Backhouse, "Analysis of mitochondrial DNA in microfluidic systems," *J. Chromatogr. B* **822**, 78 (2005).
99. J. M. Klostranec, Q. Xiang, G. A. Farcas, J. A. Lee, A. Rhee, E. I. Lafferty, S. D. Perrault, K. C. Kain, and W. C. W Chan, "Convergence of quantum dot barcodes with microfluidics and signal processing for multiplexed high-throughput infectious disease diagnostics," *Nano Lett.* **7**, 2812 (2007).
100. T. Footz, S. Wunsam, S. Kulak, H. J. Crabtree, D. M. Glerum, and C. J. Backhouse, "Sample purification on a microfluidic device," *Electrophoresis* **22**, 3868 (2001).
101. L. M. Pilarski, J. Lauzon, E. Strachan, S. Adamia, A. Atrazhev, A. R. Belch, and C. J. Backhouse, "Sensitive detection using microfluidics technology of single cell PCR products from high and low abundance IgH VDJ templates in multiple myeloma," *J. Immunol. Method.* **305**, 94 (2005).
102. J. Chowdhury, G. V. Kagiala, S. Pushpakom, J. Lauzon, A.Makin, A. Atrazhev, A. Stickel, W. G. Newman, C. J. Backhouse, and L. M. Pilarski, "Microfluidic platform for single nucleotide polymorphism genotyping of the thiopurine s-methyltransferase gene to evaluate risk for adverse drug events," *J. Mol. Diagn.* **9**, 521 (2007).
103. J. van Dijken, G. V. Kaigala, J. Lauzon, A. Atrazhev, S. Adamia, B. J. Taylor, T. Reiman, A. R. Belch, C. J. Backhouse, and L. M. Pilarski, "Microfluidic chips for detecting the t(4;14) translocation and monitoring disease during treatment using reverse transcriptase-polymerase chain reaction analysis of IgH-MMSET hybrid transcripts," *J. Mol. Diagn.* **9**, 358 (2007).
104. A. R. Prakash, C. D. L. Rosa, J. D. Fox, and K. V. I. S. Kaler, "Identification of respiratory pathogen Bordetella Pertussis using integrated microfluidic chip technology," *Microfluid. Nanofluid.* **4**, 451 (2008).
105. G. V. Kaigala, R. J. Huskins, J. Preiksaitis, X. Pang, L. M. Pilarski, and C. J. Backhouse, "Automated screening using microfluidic chip-based PCR and product detection to assess risk of BK virus-associated nephropathy in renal transplant recipients," *Electrophoresis* **27**, 3753 (2006).
106. C. Wang, R. Oleschuk, F. Ouchen, J. Li, P. Thibault, and D. J. Harrison, "Integration of immobilized trypsin bead beds for protein digestion within a

microfluidic chip incorporating capillary electrophoresis separations and an electrospray mass spectrometry interface," *Rapid Commun. Mass Spectrom.* **14**, 1377 (2000).

107. R. Prakash and K. V. I. S. Kaler, "An integrated genetic analysis microfluidic platform with valves and a PCR chip reusability method to avoid contamination," *Microfluid. Nanofluid.* **3**, 177 (2007).
108. N. Chiem, C. Colyer, and D. J. Harrison, "Microfluidic systems for clinical diagnostics," In Proceedings of International Conference on Solid-State Sensors and Actuators, Chicago, IL, USA, 16–19 June 1997; Volume 1, pp. 183-186.
109. C. X. Qiu and D. J. Harrison, "Integrated self-calibration via electrokinetic solvent proportioning for microfluidic immunoassays," *Electrophoresis* **22**, 3949 (2001).
110. T. Tang, M. Y. Badal, G. Ocvirk, W. E. Lee, D. E. Bader, F. Bekkaoui, and D. J. Harrison, "Integrated microfluidic electrophoresis system for analysis of genetic materials using signal amplification methods," *Anal. Chem.* **74**, 725 (2002).
111. S. B. Cheng, C. D. Skinner, J. Taylor, S. Attiya, W. E. Lee, G. Picelli, and D. J. Harrison, "Development of a multichannel microfluidic analysis system employing affinity capillary electrophoresis for immunoassay," *Anal. Chem.* **73**, 1472 (2001).
112. N. R. Munce, J. Z. Li, P. R. Herman, and L. Lilge, "Microfabricated system for parallel single-cell capillary electrophoresis," *Anal. Chem.* **76**, 4983 (2004).
113. P. C. H. Li, W. Wang, and M. Parameswaran, "An acoustic wave sensor incorporated with a microfluidic chip for analyzing muscle cell contraction," *Analyst* 128, 225 (2003).
114. C. L. Bliss, J. N. McMullin, and C. J. Backhouse, "Rapid fabrication of a microfluidic device with integrated optical waveguides for DNA fragment analysis," *Lab Chip* **7**, 1280 (2007).
115. Z. Nie, S. Xu, M. Seo, P. C. Lewis, and E. Kumacheva, "Polymer particles with various shapes and morphologies produced in continuous microfluidic reactors," *J. Am. Chem. Soc.* **127**, 8058 (2005).
116. H. Zhang, E. Tumarkin, R. Peerani, Z. Nie, R. M. A. Sullan, G. C. Walker, and E. Kumacheva, "Microfluidic production of biopolymer microcapsules with controlled morphology," *J. Am. Chem. Soc.* **128**, 12205 (2006).
117. Z. Nie, W. Li, M. Seo, S. Xu, and E. Kumacheva, "Janus and ternary particles generated by microfluidic synthesis: design, synthesis, and self-assembly," *J. Am. Chem. Soc.* **128**, 9408 (2006).
118. H. Zhang, E. Tumarkin, R. M. A. Sullan, G. C. Walker, and E. Kumacheva, "Exploring microfluidic routes to microgels of biological polymers," *Macromol. Rapid Commun.* **28**, 527 (2007).
119. S. Xu, Z. Nie, M. Seo, P. Lewis, E. Kumacheva, H. A. Stone, P. Garstecki, D. B. Weibel, I. Gitlin, and G. M. Whitesides, "Generation of monodisperse particles by using microfluidics: control over size, shape, and composition," *Angew. Chem.* **117**, 734 (2005).
120. M. Seo, Z. Nie, S. Xu, P. C. Lewis, and E. Kumacheva, "Microfluidics: from dynamic lattices to periodic arrays of polymer disks," *Langmuir* **21**, 4773 (2005).

121. M. Seo, C. Paquet, Z. Nie, S. Xua, and E. Kumacheva, "Microfluidic consecutive flow-focusing droplet generators," *Soft Matter* **3**, 986 (2007).
122. J. I. Park, Z. Nie, A. Kumacheva, A. I. Abdelrahman, B. P. Binks, H. A. Stone, and E. Kumacheva, "A microfluidic approach to chemically driven assembly of colloidal particles at gas-liquid interfaces," *Angew. Chem.* **121**, 5404 (2009).
123. D. A. Duford, D. D. Peng, and E. D. Salin, "Magnetically driven solid sample preparation for centrifugal microfluidic devices," *Anal. Chem.* **81**, 4581 (2009).
124. Y. Xi, E. J. Templeton, and E. D. Salin, "Rapid simultaneous determination of nitrate and nitrite on a centrifugal microfluidic device," *Talanta* **82**, 1612 (2010).
125. J. P. Lafleur, A. A. Rackov, S. McAuley, and E. D. Salin, "Miniaturised centrifugal solid phase extraction platforms for in-field sampling, pre-concentration and spectrometric detection of organic pollutants in aqueous samples," *Talanta* **81**, 722 (2010).
126. Y. Godwal, G. Kaigala, V. Hoang, S. L. Lui, C. Backhouse, Y. Y. Tsui, and R. Fedosejevs, "Elemental analysis using micro laser-induced breakdown spectroscopy in a microfluidic platform," *Opt. Express* **16**, 12435 (2008).
127. Y. Godwal, M. T. Taschuk, S. L. Lui, Y. Y. Tsui, and R. Fedosejevs, "Development of laser-induced breakdown spectroscopy for microanalysis applications," *Laser Part. Beams* **26**, 95 (2008).
128. S. A. Maier, "*Plasmonics: foundamentals and applications*," New York: Springer, 2007.
129. K. Welford, "Surface plasmon-polaritons and their uses," *Opt. Quant. Electron.* **23**, 1 (1991).
130. E. K. Akowuah, T. Gorman, and S. Haxha, "Design and optimization of novel surface plasmon resonance biosensor based on Otto configuration," *Opt. Express* **17**, 23511 (2009).
131. H. S. Leong, J. Guo, R. G. Lindquist, and Q. H. Liu, "Surface plasmon resonance in nanostructured metal films under the Kretschmann configuration," *J. Appl. Phys.* **106**, 124314 (2009).
132. W. H. Yeh, J. Kleingartner, and A. C. Hillier, "Wavelength tunable surface plasmon resonance-enhanced optical transmission through a chirped diffraction grating," *Analyt. Chem.* **82**, 4988 (2010).
133. W. Chien, M. Z. Khalid, X. D. Hoa, and A. G. Kirk, "Monolithically integrated surface plasmon resonance sensor based on focusing diffractive optic element for optofluidic platforms," *Sens. Actuat. B* **138**, 441 (2009).
134. A. A. Kolomenskii, P. D. Gershon, and H. A. Schuessler, "Sensitivity and detection limit of concentration and adsorption measurements by laser-induced surface-plasmon resonance," *Appl.Opt.* **36**, 6539 (1997).
135. J. H. Grassi and R. M. Georgiadis, "Temperature-dependent refractive index determination from critical angle measurements: implications for quantitative SPR sensing," *Anal. Chem.* **71**, 4392 (1999).
136. D. Sinton, R. Gordon, and A. G. Brolo, "Nanohole arrays in metal films as optofluidic elements: progress and potential," *Microfluid. Nanofluid.* **4**, 107 (2008).

137. C. Escobedo, A. G. Brolo, R. Gordon, and D. Sinton, "Optofluidic sieving with flow-through plasmonic nanohole arrays," In Proceedings of Conference of Lasers and Electro-Optics (CLEO) and Quantum Electronics and Laser Science Conference (QELS), San Jose, CA, USA, 16–21 May 2010; pp. 1-2.
138. A. D. Leebeeck, L. K. S. Kumar, V. Lange, D. Sinton, R. Gordon, and A. G. Brolo, "On-chip surface-based detection with nanohole arrays," *Anal. Chem.* **79**, 4094 (2007).
139. F. Eftekhari, R. Gordon, J. Ferreira, A. G. Brolo, and D. Sinton, "Polarization-dependent sensing of a self-assembled monolayer using biaxial nanohole arrays," *Appl. Phys. Lett.* **92**, 253103 (2008).
140. J. Ferreira, M. J. L. Santos, M. M. Rahman, A. G. Brolo, R. Gordon, D. Sinton, and E. M. Girotto, "Attomolar protein detection using in-hole surface plasmon resonance," *J. Am. Chem. Soc.* **131**, 436 (2009).
141. F. Eftekhari, C. Escobedo, J. Ferreira, X. Duan, E. M. Girotto, A. G. Brolo, R. Gordon, and D. Sinton, "Nanoholes as nanochannels: flow-through plasmonic sensing," *Anal. Chem.* **81**, 4308 (2009).
142. E. Ouellet, C. Lausted, T. Lin, C. W. T. Yang, L. Hood, and E. T. Lagally, "Parallel microfluidic surface plasmon resonance imaging arrays," *Lab Chip* **10**, 581 (2010).
143. V. Kanda, J. K. Kariuki, D. J. Harrison, and M. T. McDermott, "Label-free reading of microarray-based immunoassays with surface plasmon resonance imaging," *Anal. Chem.* **76**, 7257 (2004).
144. L. Malic, B. Cui, T. Veres, and M. Tabrizian, "Enhanced surface plasmon resonance imaging detection of DNA hybridization on periodic gold nanoposts," *Opt. Lett.* **32**, 3092 (2007).
145. L. Malic, T. Veres, and M. Tabrizian, "Two-dimensional droplet-based surface plasmon resonance imaging using electrowetting-on-dielectric microfluidics," *Lab Chip* **9**, 473 (2009).
146. L. Malic, T. Veres, and M. Tabrizian, "Biochip functionalization using electrowetting-on-dielectric digital microfluidics for surface plasmon resonance imaging detection of DNA hybridization," *Biosens. Bioelectron.* **24**, 2218 (2009).
147. M. W. L. Watson, M. Abdelgawad, G. Ye, N. Yonson, J. Trottier, and A. R. Wheeler, "Microcontact printing-based fabrication of digital microfluidic devices," *Anal. Chem.* **78**, 7877 (2006).
148. M. Abdelgawad and A. R. Wheeler, "Rapid prototyping in copper substrates for digital microfluidics," *Adv. Mater.* **19**, 133 (2007).
149. M. Abdelgawad and A. R. Wheeler, "Low-cost, rapid-prototyping of digital microfluidics devices," *Microfluid. Nanofluid.* **4**, 349 (2008).
150. D. Brassard, L. Malic, F. Normandin, M. Tabrizian, and T. Veres, "Improving the operation of electrowetting-based digital micro-fluidic systems by using water-oil core-shell droplets," In Proceedings of the Twelfth International Conference on Miniaturized Systems for Chemistry and Life Sciences, San Diego, CA, USA, 12-16 October 2008; pp. 772-774.
151. V. N. Luk, G. C. Mo, and A. R. Wheeler, "Pluronic additives: a solution to sticky problems in digital microfluidics," *Langmuir* **24**, 6382 (2008).

152. H. Guo, P. Zhao, G. Xiao, Z. Zhang, and J. Yao, "Optical manipulation of microparticles in an SU-8/PDMS hybrid microfluidic chip incorporating a monolithically integrated on-chip lens set," *Quant. Electron.* **16**, 919 (2010).
153. B. R. Watts, T. Kowpak, Z. Zhang, C. Xu, and S. Zhu, "Formation and characterization of an ideal excitation beam geometry in an optofluidic device," *Bio. Opt. Express* **1**, 848 (2010).
154. Y. Cheng, H. L. Tsai, K. Sugioka, and K. Midorikawa, "Fabrication of 3D microoptical lenses in photosensitive glass using femtosecond laser micromachining," *Appl. Phys. A* **85**, 11 (2006).
155. Z. Wang, K. Sugioka, and K. Midorikawa, "Three-dimensional integration of microoptical components buried inside photosensitive glass by femtosecond laser direct writing," *Appl. Phys. A* **89**, 951 (2007).
156. Z. Wang, K. Sugioka, and K. Midorikawa, "Fabrication of integrated microchip for optical sensing by femtosecond laser direct writing of Foturan glass," *Appl Phys A* **93**, 225 (2008).
157. F. He, Y. Cheng, L. Qiao, C. Wang, Z. Xu, K. Sugioka, K. Midorikawa, and J. Wu, "Two-photon fluorescence excitation with a microlens fabricated on the fused silica chip by femtosecond laser micromachining," *Appl. Phys. Lett.* **96**, 041108 (2010).
158. V. Maselli, J. R. Grenier, S. Ho, and P. R. Herman, "Femtosecond laser written optofluidic sensor: Bragg grating waveguide evanescent probing of microfluidic channel," *Opt. Express* **17**, 11719 (2009).
159. R. St-Gelais, J. Masson, and Y. A. Peter, "High resolution microfluidic refractometer for biomedical applications," In Proceedings of 2009 International Conference on Microtechnologies in Medicine and Biology, Québec City, PQ, Canada, 1–3 April 2009; pp. 96-97.
160. Y. Cheng, K. Sugioka, K. Midorikawa, M. Masuda, K. Toyoda, Masako Kawachi, and K. Shihoyama, "Three-dimensional micro-optical components embedded in photosensitive glass by a femtosecond laser," *Opt. Lett.* **28**, 1144 (2003).
161. S. Balslev, A. M. Jorgensen, B. Bilenberg, K. B. Mogensen, D. Snalenborg, O. Geschke, J. P. Kutter, and A. Krostensen, "Lab-on-a-chip with integrated optical transducers," *Lab chip* **6**, 213 (2006).
162. K. C. Vishnubhatla, J. Clark, G. Lanzani, R. Ramponi, R. Osellame, and T. Virgili, "Femtosecond laser fabrication of microfluidic channels for organic photonic devices," *Appl. Opt.* **48**, G114 (2009).
163. Y. Cheng, K. Sugioka, and K. Midorikawa, "Microfluidic laser embedded in glass by three-dimensional femtosecond laser microprocessing," *Opt. Lett.* **29**, 2007 (2004).
164. R. Gordon, J. T. Blakely, and D. Sinton, "Particle-optical self-trapping," *Phys. Rev. A* **75**, 055801 (2007).
165. J. T. Blakely, D. Sinton, and R. Gordon, "Flow dependent optofluidic particle trapping," In Proceedings of Conference of Lasers and Electro-Optics, 2008 and 2008 Conference on Quantum Electronics and Laser Science, San Jose, CA, USA, 4–9 May 2008; pp. 1-2.

166. R. Gordon, M. Kawano, J. T. Blakely, and D. Sinton, "Optohydrodynamic theory of particles in a dual-beam optical trap," *Phys. Rev. B* **77**, 245125 (2008).
167. M. Kawano, J. T. Blakely, R. Gordon, and D. Sinton, "Theory of dielectric microsphere dynamics in a dual-beam optical trap," *Opt. Express* **16**, 9306 (2008).
168. B. R. Watts, T. M. Kowpak, C. Xu, and S. Zhu, "Optical simulation, design, and optimization of a microchip-based flow cytometer," In Proceedings of Conference of Photonics North 2008, Montreal, QC, Canada, 02 June 2008.
169. X. T. Su, W. Rozmus, and Y. Y. Tsui, "Wide angle light scattering differentiation of organelle-size particle distributions in whole cells," *Cytometry A* **77**, 580 (2010).
170. X. Su, S. E. Kirkwood, H. Gul, K. Singh, M. Z. Islama, A. Janowska-Wieczorek, W. Rozmus, and Y. Y. Tsui, "Light scattering characterization of single biological cells in a microfluidic cytometer," Proc. SPIE 2009 **7386**, 738602-1-8.
171. M. Z. Islam, X. Su, S. E. Kirkwood, K. Singh, J. N. McMullin, W. Rozmus, A. Janowska-Wieczorek, and Y. Y. Tsui, "Development of an opto-microfluidic flow cytometer for the sorting of stem cells from blood samples," Proc. SPIE 2009, **7386**, 73860C-1-8.
172. P. Dumais, C. L. Callender, J. P. Noad, and C. J. Ledderhof, "Microchannel-based refractive index sensors monolithically integrated with silica waveguides: structures and sensitivities," *IEEE Sens. J.* **8**, 457 (2008).
173. P. Dumais, C. L. Callender, C. J. Ledderhof, and J. P. Noad, "Temperature sensors and refractometers using liquid-core waveguide structures monolithically integrated in silica-on-silicon," Proc. SPIE 2008, **7099**, 70991Y.
174. A. S. Jugessur, J. J. Dou, S. Aitchison,; R. M. De La Rue, and M. Gnan, "A photonic nano-Bragg grating device integrated with microfluidic channels for biosensing applications," *Microelectron. Eng.* **86**, 1488 (2009).
175. P. P. Pronko, S. K. Dutta, J. Squier, J. V. Rudd, D. Du, and G. Mourou, "Machining of sub-micron holes using a femtosecond laser at 800 nm," *Opt. Commun.* **114**, 106 (1995).
176. B. N. Chichkov, C. Momma, S. Nolte, F. von Alvensleben, and A. Tunnermann, "Femtosecond, picosecond and nanosecond laser ablation of solids," *Appl. Phys. A-Mat. Sci. Process.* **63**, 109 (1996).
177. S. Nolte, C. Momma, H. Jacobs, and A. Tunnermann, "Ablation of metals by untrashort laser pulses," *J. Opt. Soc. Am. B* **14**, 2716 (1997).
178. J. P. McDonald, S. Ma, T. M. Pollock, S. M. Yalisove, and J. A. Nees, "Femtosecond pulsed laser ablation dynamics and ablation morphology of nickel based superalloy CMSX-4," *J. Appl. Phys.* **103**, 093111 (2008).
179. S. Ameer-Beg, W. Perrie, S. Rathbone, J. Wright, W. Weaver, and H. Champoux, "Femtosecond laser microstructuring of materials," *Appl. Surf. Sci.* **127-129**, 875 (1998).
180. A. Ben-Yakar, R. L. Byer, A. Harkin, J. Ashmore, H. A. Stone, M. shen, and E. Mazur, "Morphology of femtosecond-laser-ablated borosilicate glass surfaces," *Appl. Phys. Lett.* **83**, 3030 (2003).

181. E. Vanagas, I. Kudryashov, D. Tuzhilin, S. Juodkazis, S. Matsuo, and H. Misawa, "Surface nanostructuring of borosilicate glass by femtosecond nJ energy pulses," *Appl. Phys. Lett.* **82**, 2901 (2003).
182. Y. Izawa, S. Tokita, M. Fujita, M. Nakai, T. Norimatsu, and Y. Izawa, "Ultrathin amorphization of single-crystal silicon by ultraviolet femtosecond laser pulse irradiation," *J. Appl. Phys.* **105**, 064909 (2009).
183. S. Panchatsharam, B. Tan, and K. Venkatakrishnan, "Femtosecond laser-induced shockwave formation on ablated silicon surface," *J. Appl. Phys.* **105**, 093103 (2009).
184. J. P. McDonald, J. L. Hendricks, V. R. Mistry, D. C. Martin, and S. M. Yalisove, "Femtosecond pulsed laser patterning of poly (3, 4-ethylene dioxythiophene)-poly (styrenesulfonate) thin films on gold/palladium substrates," *J. Appl. Phys.* **102**, 013107 (2007).
185. M. Lenzner, J. Krüger, S. Sartania, Z. Cheng, C. Spielmann, G. Mourou, W. Kautek, and F. Krausz, "Femtosecond optical breakdown in dielectrics," *Phys. Rev. Lett.* **80**, 4076 (1998).
186. D. Giguère, G. Olivié, F. Vidal, S. Toetsch, G. Girard, T. Ozaki, and J. Kieffer, "Laser ablation threshold dependence on pulse duration for fused silica and corneal tissues: experiments and modeling," *J. Opt. Soc. Am. A* **24,** 1562 (2007).
187. B. C. Stuart, M. D. Feit, S. Herman, A. M. Rubenchik, B. W. Shore, and M. D. Perry, "Nanosecond-to-femtosecond laser-induced breakdown in dielectrics," *Phys. Rev. B* **53**, 1749 (1996).
188. D. Ashkenasi, M. Lorenz, R. Stoian, and A. Rosenfeld, "Surface damage threshold and structuring of dielectrics using femtosecond laser pulses: the role of incubation," *Appl. Surf. Sci.* **150**, 101 (1999).
189. D. Ashkenasi, A. Rosenfeld, H. Varel, M. Wa¨hmer, and E. E. B. Campbell, "Laser processing of sapphire with picosecond and sub-picosecond pulses," *Appl. Surf. Sci.* **120,** 65 (1997).
190. Z. Wu, H. Jiang, Z. Zhang, Q. Sun, H. Yang, and Q. Gong, "Morphological investigation at the front and rear surfaces of fused silica processed with femtosecond laser pulses in air," *Opt. Express* **10**, 1244 (2002).
191. M. R. Kasaai, S. Lagace, D. Boudreau, E. Forster, B. Muller, and S. L. Chin, "Creation of micro-holes on glass surface by femtosecond laser through the ejection of molten material," *J. Non-Cryst. Solilds* **292**, 202 (2001).
192. H. Y. Zheng, W. Zhou, H. X. Qian, T. T. Tan, and G. C. Lim, "Polarisation-independence of femtosecond laser machining of fused silica," *Appl. Surf. Sci.* **236**, 114 (2004).
193. C. B. Schaffer, A. Brodeur, and E. Mazur, "Laser-induced breakdown and damage in bulk transparent materials induced by tightly focused femtosecond laser pulses," *Meas. Sci. Technol.* **12**, 1784 (2001).
194. T. Q. Jia, H. X. Chen, M. Huang, F. L. Zhao, X. X. Li, S. Z. Xu, H. Y. Sun, D. H. Feng, C. B. Li, X. F. Wang, R. X. Li, Z. Z. Xu, X. K. He, and H. Kuroda, "Ultraviolet-infrared femtosecond laser-induced damage in fused silica and CaF_2 crystals," *Phy. Rev. B* **73**, 054105 (2006).
195. A. Ghatak, "*Optics*," 4th ed., Tata McGraw-Hill, 2009.

196. E. N. Glezer and E. Mazur, "Ultrafast- laser driven micro-explosions in transparent materials," *Appl. Phys. Lett.* **71**, 882 (1997).
197. C. B. Schaffer, J. F. Garcia, and E. Mazur, "Bulk heating of transparent materials using a high repetition rate femtosecond laser," *Appl. Phys. A* **76**, 351 (2003).
198. J. Jasns and K. Brenner, "*Microoptics: from technology to applications*," New York: Springer, 2004.
199. S. M. Eaton, H. Zhang, P. R. Herman, F. Yoshino, L. Shah, J. Bovatsek, and A. Y. Arai, "Heat accumulation effects in femtosecond laser-written waveguides with variable repetition rate," *Opt. Express* **13**, 4708 (2005).
200. A. Zoubir, M. Richardson, L. Canioni, A. Brocas, and L. Sarger, "Optical properties of infrared femtosecond laser-modified fused silica and application to waveguide fabrication," *J. Opt. Soc. Am. B* **22**, 2138 (2005).
201. G. D. Valle, R. Osellame, and P. Laporta, "Micromachining of photonic devices by femtosecond laser pulses," *J. Opt. A: Pure Appl. Opt* **11**, 013001 (2009).
202. K. Hirao and K. Miura, "Writing waveguides and gratings in silica and related materials by a femtosecond laser," *J. Non-Cryst. Solids* **239**, 91 (1998).
203. C. B. Schaffer, A. Brodeur, J. F. García, and E. Mazur, "Micromachining bulk glass by use of femtosecond laser pulses with nanojoule energy," *Opt. Lett.* **26**, 93 (2001).
204. A. H. Nejadmalayeri and P. R. Herman, "Rapid thermal annealing in high repetition rate ultrafast laser waveguide writing in lithium niobate," *Opt. Express* **15**, 10842 (2007).
205. J. W. Chan, T. Huser, S. Risbud, and D. M. Krol, "Structural changes in fused silica after exposure to focused femtosecond laser pulses," *Opt. Lett.* **26**, 1726 (2001).
206. A. M. Streltsov and N. F. Borrelli, "Study of femtosecond-laser-written waveguides in glasses," *J. Opt. Soc. Am. B* **19**, 2496 (2002).
207. F. Vega, J. Armengol, V. Diez-Blanco, J. Siegel, J. Solis, B. Barcones, A. Perez-Rondriguez, and P. Loza-Alvarez, "Mechanisms of refractive index modification during femtosecond laser writing of waveguides in alkaline lead-oxide silicate glass," *Appl. Phys. Lett.* **87**, 021109 (2005).
208. Y. Li, Z. He, H. Tang, L. Liu, L. Xu, and W. Wang, "The structural and refractive index changes in the waveguides written by femtosecond laser in Er-doped silicate glasses," *J. Non-Cryst. Solids* **354**, 1216 (2008).
209. L. B. Fletcher, J. J. Witcher, W. B. Reichman, A. Arai, J. Bovatsek, and D. M. Krol1, "Changes to the network structure of Er–Yb doped phosphate glass induced by femtosecond laser pulses," *J. Appl. Phys.* **106**, 083107 (2009).
210. W. F. Silva, C. Jacinto, A. Benayas, J. R. Vazquez de Aldana, G. A. Torchia, F. Chen, Y. Tan, and D. Jaque, "Femtosecond-laser-written, stress-induced Nd: YVO_4 waveguides preserving fluorescence and Raman gain," *Opt. Lett.* 35, 916 (2010).
211. A. Ródenas, A. H. Nejadmalayeri, D. Jaque, and P. Herman, "Confocal Raman imaging of optical waveguides in $LiNbO_3$ fabricated by ultrafast high-repetition rate laser-writing," *Opt. Express* **16**, 1379 (2008).

212. S. M. Eaton, C. A. Merchant, R. Iyer, A. J. Zilkie, A. S. Helmy, J. S. Aitchison, P. R. Herman, D. Kraemer, R. J. D. Miller, C. Hnatovsky, and R. S. Taylor, "Raman gain from waveguides inscribed in $KGd(WO_4)_2$ by high repetition rate femtosecond laser," *Appl. Phys. Lett.* **92**, 081105 (2008).
213. B. McMillen, K. P. Chen, and D. Jaque, "Microstructural imaging of high repetition rate ultrafast laser written $LiTaO_3$ waveguides," *Appl. Phys. Lett.* **94**, 081106 (2009).
214. C. M. Endez, J. R. Vazquez de Aldana, G. A. Torchia, and L. Roso, "Optical waveguide arrays induced in fused silica by void-like defects using femtosecond laser pulses," *Appl. Phys. B* **86**, 343 (2007).
215. C. N. Borca, V. Apostolopoulos, F. Gardillou, H. G. Limberger, M. Pollnau, and R. P. Salathe, "Buried channel waveguides in Yb-doped $KY(WO_4)_2$ crystals fabricated by femtosecond laser irradiation," *Appl. Surf. Sci.* **253,** 8300 (2007).
216. J. Burghoff, C. Grebing, S. Nolte, and A. Tünnermannb, "Efficient frequency doubling in femtosecond laser-written waveguides in lithium niobate," *Appl. Phys. Lett.* **89**, 081108 (2006).
217. J. Thomas, M. Heinrich, J. Burghoff, S. Nolte, A. Ancona and A. Tünnermann, "Femtosecond laser-written quasi-phase-matched waveguides in lithium niobate," *Appl. Phys. Lett.* **91**, 151108 (2007).
218. J. Burghoffl, S. Nolte, and A. Tünnermann, "Origins of waveguiding in femtosecond laser-structured $LiNbO_3$," *Appl. Phys. A* **89**, 127 (2007).
219. W. Reichman, J. W. Chan, and D. M. Krol, "Confocal fluorescence and Raman microscopy of femtosecond laser-modified fused silica," *J. Phys.: Condens. Matter* **15**, S2447 (2003).
220. C. W. Ponader, J. F. Schroeder, and A. M. Streltsov, "Origin of the refractive-index increase in laser-written waveguides in glasses," *J. Appl. Phys.* **103**, 063516 (2008).
221. Y. Bellouard, E. Barthel, A. A. Said, M. Dugan, and P. Bado, "Scanning thermal microscopy and Raman analysis of bulk fused silica exposed to low energy femtosecond laser pulses," *Opt. Express* **16**, 19520 (2008).
222. C. Hnatovsky, R. S. Taylor, E. Simova, V. R. Bhardwaj, D. M. Rayner, and P. B. Corkum, "Polarization-selective etching in femtosecond laser-assisted microfluidic channel fabrication in fused silica," *Opt. Lett.* **30**, 1867 (2005).
223. V. Maselli, R. Osellame, G. Cerullo, R. Ramponi, P. Laporta, L. Magagnin, and P. L. Cavallotti, "Fabrication of long microchannels with circular cross section using astigmatically shaped femtosecond laser pulses and chemical etching," *Appl. Phys. Lett.* **88**, 191107 (2006).
224. Z. Wang and H. Y. Zheng, "Femtosecond laser direct writing microfluidic channels inside photosensitive glass," photonics Global @ Singapore, 2008. IPGC 2008. IEEE.
225. R. Osellame, V. Maselli, R. M. Vazquez, R. Ramponi, and G. Cerullo, "Integration of optical waveguides and microfluidic channels both fabricated by femtosecond laser irradiation," *Appl. Phys. Lett.* **90**, 231118 (2007).

226. D. Wortmann, J. Gottmann, N. Brandt, and H. H. Solle, "Micro- and nanostructures inside sapphire by fs-laser irradiation and selective etching," *Opt. Express* **16**, 1517 (2008).
227. C. Hnatovsky, R. S. Taylor, E. Simova, P. P. Rajeev, D. M. Rayner, V. R. Bhardwaj and P.B. Corkum, "Fabrication of microchannels in glass using focused femtosecond laser radiation and selective chemical etching," *Appl. Phys. A* **84**, 47 (2006).
228. Q. Sun, A. Saliminia, F. Theberge, R. Vallee and S. L. Chin, "Microchannel fabrication in silica glass by femtosecond laser pulses with different central wavelengths," *J. Micromech. Microeng.* **18**, 035039 (2008).
229. Y. Shimotsuma, P. G. Kazansky, J. Qiu, and K. Hirao, "Self-organized nanogratings in glass irradiated by ultrashort light pulses," *Phys. Rev. Lett.* **91**, 247405 (2003).
230. T. M. Squires and S. R. Quake, "Microfluidic: fluid physics at the nanoliter scale," *Rev. Mod. Phys.* **77**, 977 (2005).
231. S. Kakac, B. Kosoy, D. Li, and A. Pramuanjaroenkij, "*Microfluidics based microsystems: fundamentals and applications*," 1st ed., Turkey: Springer, 2009.
232. J. Crank. "*The Mathematics of Diffusion*," 2nd ed. Oxford: Oxford University Press, 1975.
233. B. H. Weigl and P. Yager, "Microfluidic diffusion-based separation and detection," *Science* **283**, 346 (1999).
234. A. E. Kamholz, and P. Yager, "Theoretical analysis of molecular diffusion in pressure-driven laminar flow in microfluidic channels," *Biophys. J.* **80**, 155 (2001).
235. A. E. Kamholz, E. A. Schilling, and P. Yager, "Optical measurement of transverse molecular diffusion in a microchannel," *Biophys. J.* **80**, 1967 (2001).
236. A. E. Kamholz, B. H. Weigl, B. A. Finlayson, and P. Yager, "Quantitative analysis of molecular interaction in a microfluidic channel: the T-sensor," *Anal. Chem.* **71**, 5340 (1999).
237. A. E. Kamholz, and P. Yager, "Molecular diffusive scaling laws in pressure-driven microfluidic channels: deviation from one-dimensional Einstein approximation," Sens. *Actuators B* **82**, 117 (2002).
238. C. N. Baroud, F. Okkels, L. Menetrier, and P. Tabeling, "Reaction-diffusion dynamics: confrontation between theory and experiment in a microfluidic reactor," *Phys. Rev. E* **67**, 060104 (2003).
239. J. P. Brody, P. Yager, R. E. Goldstein, and R. H. Austin, "Biotechnology at low Reynolds number," *Biophys. J.* **71**, 3430 (1996).
240. J. P. Brody and P. Yager, "Diffusion-based extraction in a microfabricated device," *Sens. Actuators A* **58**, 13 (1997).
241. B. S. Cho, T. G. Schuster, X. Zhu, D. Chang, G. D. Smith, and S. Takayama, "Passively driven integrated microfluidic system for separation of motile sperm," *Anal. Chem.* **75**, 1671 (2003).
242. N. L. Jeon, S. K. W. Dertinger, D. T. Chiu, I. S. Choi, A. D. Stroock, and G. M. Whitesides, "Generation of solution and surface gradients using microfluidic systems," *Langmuir* **16**, 8311 (2000).

243. D. Schafer, E. A. Gibson, E. A. Salim, A. E. Palmer, R. Jimenez, and J. Squier, "Microfluidic cell counter with embedded optical fibers fabricated by femtosecond laser ablation and anodic bonding," *Opt. Express.* **17**, 6068 (2009).
244. M. Kim, D. J. Hwang, H. Jeon, K. Hiromatsu and C. P. Grigoropoulos, "Single cell detection using a glass-based optofluidic device fabricated by femtosecond laser pulses," *Lab chip* **9**, 311 (2009).